

# New Optimal Periodic Control Policy for the Optimal Periodic Performance of a Chemostat Using a Fourier-Gegenbauer-Based Predictor-Corrector Method

Kareem T. Elgindy<sup>\*,a</sup>

<sup>a</sup>*Mathematics & Statistics Department, The College of Sciences, King Fahd University of Petroleum & Minerals  
Dhahran 31261, Kingdom of Saudi Arabia*

---

## Abstract

In its simplest form, the chemostat consists of microorganisms or cells which grow continually in a specific phase of growth while competing for a single limiting nutrient. Under certain conditions on the cells' growth rate, substrate concentration, and dilution rate, the theory predicts and numerical experiments confirm that a periodically operated chemostat exhibits an "over-yielding" state in which the performance becomes higher than that at the steady-state operation. In this paper we show that an optimal control policy for maximizing the chemostat performance can be accurately and efficiently derived numerically using a novel class of integral-pseudospectral methods and adaptive  $h$ -integral-pseudospectral methods composed through a predictor-corrector algorithm. Some new formulas for the construction of Fourier pseudospectral integration matrices and barycentric shifted Gegenbauer quadratures are derived. A rigorous study of the errors and convergence rates of shifted Gegenbauer quadratures as well as the truncated Fourier series, interpolation operators, and integration operators for nonsmooth and generally  $T$ -periodic functions is presented. We introduce also a novel adaptive scheme for detecting jump discontinuities and reconstructing a discontinuous function from the pseudospectral data. An extensive set of numerical simulations is presented to support the derived theoretical foundations.

*Key words:* Adaptive method, Chemostat model, Fourier interpolation, Gegenbauer polynomials,  $h$ -integral-pseudospectral, Integration matrix, Optimal control, Predictor-Corrector, Pseudospectral method.

---

## 1. Introduction

A chemostat is a laboratory bioreactor in which a microbial culture in a well-stirred culture medium is continuously supplied with nutrients at a fixed/variable rate, while an equal flow of the culture liquid containing micro-organisms and nutrients is continuously drained out from the culture vessel, so that the vessel retains a constant volume of culture at all times. In this manner, a chemostat enables experimental control of cell growth rates within limits in a well-defined and controlled environment and the microbial cells external environment remains constant. The control of the growth rate in this manner allows to (i) optimize the production of specific microbial products like ethanol and antibiotics, (ii) optimize the production of L-leucine used for blood sugar and energy levels regulations, the growth and repairment of bones and muscles, and healing of wounds, (iii) facilitate the study of nutrient limitation and the micro-organisms growth in natural ecological environments such as rivers and lakes, (iv) analyzing the complex interactions between distinct biological populations, (v) waste-water treatment by decomposing harmful substances in waste-water to improve the water quality, etc. [1–6]. For these reasons, the chemostat is of great theoretical and practical value in applied sciences and the industry.

One of the main challenges in operating the chemostat is the maintenance of required growing conditions of the micro-organisms. There are practically three variables that can be manipulated in a chemostat, namely, the dilution rate (aka the feeding rate) and the input concentrations of the substrate and the biomass. Assuming that the latter two are given, one can control the flow rate and maintain a constant substrate concentration. However, it is well known, since the discovery of Douglas and Rippin [7], that the performance of an unsteady-state (dynamically or periodically) operated biochemical reactor is sometimes superior to that obtained under conventional steady-state<sup>1</sup> operation in the sense that the conversion can be increased by cycling one or more inputs, stirring many research works in that direction for more than half a century; cf. [8–16], and the Refs. therein. An important case of periodic operations is when the steady-state condition is chosen arbitrarily and the time-averaged substrate concentration is

---

<sup>\*</sup>Corresponding author

*Email address:* kareem.elgindy@kfupm.edu.sa (Kareem T. Elgindy)

<sup>1</sup>At steady state, the dilution rate is equal to the specific growth rate of the cells population; thus, the experimenter can force the cells to grow at a desired rate.

equal to the substrate concentration value at the steady-state operation; cf. [17, 18]. Another perhaps more interesting class of periodic operations is when the time-averaged substrate concentration is less than that at the steady-state operation; such systems were termed “*over-yielding*” systems; cf. [19].

The success of optimizing the performance of a chemostat depends upon the availability of a representative mathematical model of the process and the choice of an appropriate numerical and optimization routine. For periodically operated chemostat systems, one can describe the process using a finite-horizon optimal control problem and the chemostat performance can be maximized by determining the optimal periodic control under certain conditions; cf. [15, 20]. When the dilution rate is used as the control variable, Bayen et al. [15] showed through Pontryagin Maximum Principle that the best periodic control for a chemostat exhibiting an over-yielding state is “*bang-bang with even switching times.*” However, the derived mathematical model was only solved numerically using BOCOP<sup>2</sup>. This motivates us to explore new optimal periodic control policies to improve the chemostat performance in light of a more accurate, robust, and efficient numerical method. In our work we shall consider the chemostat of a single reaction model where the growth rate of the micro-organisms is given by a Contois expression, which was introduced by Contois [21] to model the growth of *Aerobacter aerogenes*, and was often used later to model the growth of biomass in waste-waters containing biodegradable organic materials [16, 22]. A clear exposition of a broad class of growth rate functions exhibiting a wide range of outlooks on the subject can be found in the book of Moser [23].

Our main goal in this paper is to numerically determine the optimal periodic dilution rate associated with a periodically varying substrate concentration that can optimize the performance of an over-yielding chemostat in terms of the time-averaged substrate concentration over a given finite-horizon. To this end, we shall explore the possibility of applying two attractive classes of methods in a unified composite approach. The first class is the class of Fourier integral-pseudospectral (FIPS) methods<sup>3</sup> where the periodic solutions are represented in terms of grid point values by way of interpolants. Integral-pseudospectral (IPS) methods are robust variants of the popular pseudospectral (PS) methods in which an initial step of reformulating the dynamical system equations in their integral form is required first before the collocation phase starts. The integral reformulation can be performed by either a direct integration of the dynamical system equations if they have constant coefficients, or by approximating the solution’s highest-order derivative involved in the problem by a nodal finite series in terms of its grid point values, and then solve for those grid point values before successively integrating back in a stable manner to obtain the sought solution grid point values [24]. Some of the advantages of FIPS methods inherited from FPS methods include (i) their ability to furnish exponential convergence rates when the problem exhibits sufficiently smooth solutions, (ii) the nodal representation of the solution is extremely useful, since its values are immediately available at the collocation points once the full discretization is implemented, whereas Fourier series integration (FSI) methods<sup>4</sup> require a further step of computing the modal approximation after calculating Fourier coefficients, and (iii) although FPSI methods often introduce an aliasing error that does not exist in FSI methods, we prefer the former methods because of the Discrete Fourier Transform (DFT) pair, which allows us to rapidly transform from the set of function values at an equally-spaced points to the set of its interpolation coefficients using Fast Fourier Transform (FFT), and vice-versa, instead of computing  $N$  integrals to determine the Fourier series coefficients. A bonus advantage of FIPS methods over the usual FPS methods manifests in the integral reformulation strategy imposed by the former which avoids the degradation of precision often caused by numerical differentiation processes [25, 26].

For problems with nonsmooth solutions, the IPS methods lose their exponential convergence virtue, and the class of  $h$ -IPS methods comes into play as a better choice due to its ability to recover the discontinuous/nonsmooth solutions within high accuracies via the decomposition of the solution interval into smaller mesh intervals or elements ( $h$ -refinement), and approximating the restricted solution on each element with a finite, nodal expansion series in terms of the solution grid point values by means of interpolation [27]. For discontinuous solutions with unknown discontinuities, adaptive strategies are desirable to determine which elements need to be refined in advance before the collocation process takes place. This prevents excessive and blind divisions of the solution domain using composite-grid discretizations that is computationally expensive, time consuming, and often produce poor levels of accuracy compared to the former adaptive strategy [25]. Since the controller of the problem under study is discontinuous with unknown jump discontinuities as proven in [15], a FIPS approximation of the controller would suffer from Gibbs phenomenon, which appears in the form of over- and undershoots around the jump discontinuities. While Gibbs phenomenon is generally considered a demon that needs to be cast out, we shall demonstrate later that it is rather “*a blessing,*” in view of the current work, that can be constructively used to set up a robust adaptive algorithm. In particular, the over- and undershoots developed near a discontinuity in the event of a Gibbs phenomenon provides an excellent means of detecting one. This adaptive scheme together with an  $h$ -IPS method can be combined with a FIPS method to solve the optimal control problem accurately and efficiently.

In light of the above arguments, we propose a novel, composite class of IPS methods and adaptive  $h$ -IPS methods composed through a predictor-corrector algorithm. In the prediction step, the composite method applies a direct IPS method in which the optimal control problem in integral form is initially collocated in the Fourier physical space. In the correction step, the composite method carries out an adaptive  $h$ -IPS method in which the integrated dynamical system equation is collocated in the shifted Gegenbauer (SG) physical space after splitting the time domain

---

<sup>2</sup>BOCOP is an open source toolbox for optimal control; see <https://www.bocop.org/>.

<sup>3</sup>FIPS methods are aka “*Fourier pseudospectral (FPS) integration methods*” and can also be termed “*nodal Fourier integration methods.*”

<sup>4</sup>FSI methods can also be termed “*modal Fourier integration methods.*”

into smaller elements while allowing the SG interpolant degree to increase on each element as desired. For these reasons we coin the proposed method with the name “*Fourier-Gegenbauer-based predictor-corrector composite IPS and adaptive h-IPS method*,” which we prefer to abbreviate simply by the “*Fourier-Gegenbauer-based predictor-corrector (FG-PC) method*.” To the best of our knowledge, a unified procedure of this type has not been used so far for the derivation of optimal control policies of periodically operated biochemical reactors or for solving general finite-horizon optimal control problems with state- and control-variables inequality constraints.

The rest of the paper is organized as follows. In the next section we give some preliminary notations to be used in the paper. In Section 3 we present the mathematical model under study. In Section 4 we derive some new formulas for the construction of FPS integration (FPSI) matrices that are superior to the formulas obtained earlier by Elgindy [28] in terms of accuracy, speed, and computational complexity. The computational complexity and speed of constructing FPSI matrices are investigated in Section 4.1. In Section 4.2 we study the errors and convergence rates of truncated Fourier series, interpolation operators, and integration operators for nonsmooth and generally  $T$ -periodic functions. In Section 5 we study the behavior of Fourier interpolants at jump discontinuities. A discussion on detecting jump discontinuities and reconstructing a discontinuous function from the FPS data is presented in Section 6. In Section 6.1 we give a practical prescription on how to implement the edge detection strategy. A discussion on how to accurately evaluate definite integrals of reconstructed discontinuous functions from the FPS data is presented in Section 7. In Section 7.1 we derive some new formulas for constructing barycentric SG quadratures. Section 7.1.1 is devoted for studying their errors and convergence. Efficient and stable computation of SG matrices necessary for constructing the SG quadratures is discussed in Section 7.1.2. The proposed FG-PC method is presented in Section 8. Simulation results are shown in Section 9 followed by some conclusions and remarks in Section 10. A possible future work is presented in Section 11. Two computational algorithms for the fast, accurate, and economic construction of FPSI matrices and reconstructing an approximate discontinuous function from the FPS data are prescribed in Appendix A.

## 2. Preliminary Notations

**Logical Symbols.**  $\forall$ ,  $\forall_a$ ,  $\forall_e$ , and  $\forall_s$  stand for the phrases “for all”, “for any”, “for each”, and “for some”, respectively. The notations  $f \in \text{Def}(\Omega)$  and  $f \in C^k(\Omega)$  mean  $f$  is defined on the set  $\Omega$  and  $f$  has  $k$  continuous derivatives on the set  $\Omega$ .  $\forall_a$  function  $f$ , in respective order.

**Set and List Notations.**  $\text{int}(\Omega)$  stands for the interior of a set  $\Omega$ . The symbols  $\mathbb{C}$ ,  $\mathfrak{F}$ ,  $\mathbb{Z}_\emptyset$ ,  $\mathbb{Z}^+$ ,  $\mathbb{Z}_0^+$ ,  $\mathbb{Z}_e^+$ ,  $\mathbb{Z}_{0,e}^+$ ,  $\mathbb{Z}_o^+$ ,  $\mathbb{R}_\emptyset$ , and  $\mathbb{R}_0^+$  denote the sets of all complex-valued functions, all real-valued functions, non-zero integers, positive integers, non-negative integers, positive even integers, non-negative even integers, positive odd integers, non-zero real numbers, and non-negative real numbers, respectively. The notations  $i : j : k$  or  $i(j)k$  indicate a list of numbers from  $i$  to  $k$  with increment  $j$  between numbers, unless the increment equals one where we use the simplified notation  $i : k$ . For example,  $0 : 0.5 : 2$  simply means the list of numbers 0, 0.5, 1, 1.5, and 2, while  $0 : 2$  means 0, 1, and 2. The set of any numbers  $y_1, y_2, \dots, y_n$  is represented by  $\{y_{1:n}\}$ . The list of any sets  $\Omega_1, \Omega_2, \dots, \Omega_n$  is represented by  $\Omega_{1:n} \forall_a n \in \mathbb{Z}^+$ . We define  $\mathbb{J}_n = \{0 : n - 1\}$  and  $\mathbb{J}_n^+ = \mathbb{J}_n \cup \{n\} \forall_a n \in \mathbb{Z}^+$ ; moreover,  $\mathbb{K}_N = \{-N/2 : N/2\}$ ,  $\mathbb{K}'_N = \mathbb{K} \setminus \{N/2\}$ , and  $\mathbb{K}''_N = \mathbb{K} \setminus \{\pm N/2\} \forall_a N \in \mathbb{Z}_e^+$ .  $\mathbb{T}_T$  is the space of  $T$ -periodic, univariate functions  $\forall_a T \in \mathbb{R}^+$ . Also,  $\mathbb{S}_n = \{x_{n,0:n-1}\}$  and  $\mathbb{S}_n^+ = \mathbb{S}_n \cup \{x_{n,n}\}$  are the sets of  $n$ - and  $(n + 1)$ - equally-spaced points such that  $x_{n,j} = Tj/n \forall j \in \mathbb{J}_n$  and  $j \in \mathbb{J}_n^+$ , respectively.

**Function Notations.** For convenience, we shall denote  $g(x_{N,n})$  by  $g_n \forall_a g \in \mathbb{C}$ , unless stated otherwise. Moreover, if a set  $\Omega$  is partitioned into a number of subsets  $\Gamma_{1:n} \forall_s n \in \mathbb{Z}^+$ , the notation  ${}_k g$  indicates the restriction of  $g$  to  $\Gamma_k$ .

**Vector Notations.** We shall use the shorthand notation  $[z]_n$  to denote a row vector containing  $n$  copies of  $z \forall_a z \in \mathbb{C}$ ,  $n \in \mathbb{Z}^+$ . Moreover,  $c^{0:N-1}$ ,  $\mathbf{x}_N$  (or  $x_{N,0:N-1}^t$ ),  $\mathbf{x}_N^+$  (or  $x_{N,0:N}^t$ ) stand for the  $N$ th-dimensional row vector  $[c^0, c^1, \dots, c^{N-1}] \forall_a c \in \mathbb{R}_\emptyset$  and the column vectors  $[x_{N,0}, x_{N,1}, \dots, x_{N,N-1}]^t$  and  $[x_{N,0}, x_{N,1}, \dots, x_{N,N}]^t$ , respectively.  $g_{0:N-1}$ ,  $g_{0:N-1}^t$ ,  $g^{(0:n)}$ , and  $f(g_{0:N-1})$  denote the column vector  $[g_0, g_1, \dots, g_{N-1}]^t$ , the transpose vector  $[g_0, g_1, \dots, g_{N-1}]$ , the column vector of derivatives  $[g, g', \dots, g^{(n)}] \forall n \in \mathbb{Z}_0^+$ , and the column vector of composite function values  $[f(g_0), f(g_1), \dots, f(g_{N-1})] \forall_a f \in \mathbb{C}$  in respective order. Moreover,  $\text{ind } g_{0:N-1}$ ,  $\text{indmax } g_{0:N-1}$ , and  $\text{indmin } g_{0:N-1}$  denote the indices vector of nonzero values and maximum- and minimum-values of  $g_{0:N-1}$ , respectively.

**Interval Notations.** The shorthand notation  $[c, y_i]_{i=0:n-1}$  stands for the collection of intervals  $[c, y_0], \dots, [c, y_{n-1}] \forall_a c, y_0, \dots, y_{n-1} \in \mathbb{R} : y_j > c \forall j \in \mathbb{J}_n$ . The specific interval  $[0, c]$  is denoted by  $\Omega_c \forall c > 0$ . For example,  $[0, x_{N,n}]$  is denoted by  $\Omega_{x_{N,n}}$ ; moreover,  $\Omega_{x_{N,0:N-1}}$  stands for the list of intervals  $\Omega_{x_{N,0}}, \Omega_{x_{N,1}}, \dots, \Omega_{x_{N,N-1}}$ .  $|\Omega|$  gives the length of an interval  $\Omega$ .

**Integral Notations.** By closely following the convention for writing definite integrals introduced in [28], we denote  $\int_0^{x_{N,j}} h(x) dx$  by  $\mathcal{I}_{x_{N,j}}^{(x)} h \forall_a$  integrable  $h \in \mathbb{T}_T$ ; moreover, by  $\mathcal{I}_{a,b}^{(x)} f$  we mean  $\int_a^b f(x) dx \forall_a a, b \in \mathbb{R}$  and an integrable function  $f$ . If the integrand functions  $h$  and  $f$  are to be evaluated at any other expression of  $x$ , say  $u(x)$ , we express  $\int_0^{x_{N,j}} h(u(x)) dx$  and  $\int_a^b f(u(x)) dx$  with a stroke through the square brackets as  $\mathcal{I}_{x_{N,j}}^{(x)} h \{u(x)\}$  and  $\mathcal{I}_{a,b}^{(x)} f \{u(x)\}$ , respectively. We adopt the notation  $\mathcal{I}_{x_N}^{(x)} h$  to denote the  $N$ th-dimensional column vector  $[\mathcal{I}_{x_{N,0}}^{(x)} h, \mathcal{I}_{x_{N,1}}^{(x)} h, \dots, \mathcal{I}_{x_{N,N-1}}^{(x)} h]^t$ . The

notation  $\mathcal{I}_{\Omega}^{(x)} h$  simply means the definite integral  $\int_{a,b}^{(x)} h \forall_a \Omega = [a, b]$ . Moreover,  $\mathcal{I}_{\Omega_{1:n}}^{(x)} h$  stands for  $[\mathcal{I}_{\Omega_1}^{(x)} h, \dots, \mathcal{I}_{\Omega_n}^{(x)} h]^t \forall_a$  collection of intervals  $\Omega_{1:n}$ .

**Matrix Notations.**  $\mathbf{O}_n$ ,  $\mathbf{1}_n$ , and  $\mathbf{I}_n$  stand for the zero, all ones, and the identity matrices of size  $n$ . By  $[\mathbf{A}; \mathbf{B}]$  we mean the usual vertical matrix concatenation of  $\mathbf{A}$  and  $\mathbf{B} \forall_a$  two matrices  $\mathbf{A}$  and  $\mathbf{B}$  having the same number of columns. For a two-dimensional matrix  $\mathbf{C}$ , the notation  $\mathbf{C}_{\bullet}$  stands for the matrix obtained by deleting the zeroth-row of  $\mathbf{C}$ . Moreover,  $\mathbf{C}_n$  denotes a row vector whose elements are the  $n$ th-row elements of  $\mathbf{C}$ , except when  $\mathbf{C}_n = \mathbf{O}_n$ ,  $\mathbf{1}_n$ , or  $\mathbf{I}_n$ , where it denotes the size of the matrix.  $\mathbf{C}_{n,m}$  indicates that  $\mathbf{C}$  is a rectangular matrix of size  $n \times m$ . For convenience, a vector is represented in print by a bold italicized symbol while a two-dimensional matrix is represented by a bold symbol, except for a row vector whose elements form a certain row of a matrix where we represent it in bold symbol as stated earlier. For example,  $\mathbf{I}_n$  and  $\mathbf{0}_n$  denote the  $n$ -dimensional all ones- and zeros- column vectors, while  $\mathbf{1}_n$  and  $\mathbf{O}_n$  denote the all ones- and zeros- matrices of size  $n$ , respectively.

**Algorithmic Notations.** For algorithmic purpose, we adopt the notation “==” such that  $\mathbf{A} == \mathbf{B}$  gives a logical array with elements set to logical 1 where arrays  $\mathbf{A}$  and  $\mathbf{B}$  are equal; otherwise, the element is logical 0  $\forall_a$  arrays  $\mathbf{A}$  and  $\mathbf{B}$  of the same size.

### 3. Problem Statement

Consider the classical biochemical reaction kinetics model

$$\dot{s} = -\mu x + (s_{\text{in}} - s)u, \quad (3.1a)$$

$$\dot{x} = (\mu - u)x, \quad (3.1b)$$

governed by the Contois growth model

$$\mu = \frac{\mu_{\text{max}} s}{k_s x + s}, \quad (3.1c)$$

where  $s(t)$ ,  $x(t)$ , and  $u(t)$  are the substrate concentration, the micro-organism concentration, and the dilution rate (aka the feeding rate) at any time  $t \in \Omega_T \forall_s T > 0$ , respectively,  $\mu(s, x)$  is the specific growth rate of the micro-organisms,  $\mu_{\text{max}}$  is the maximum specific growth rate, and  $k_s$  is the Contois saturation constant. Assume that (i)  $s_{\text{in}} > 0$  is the input substrate concentration, (ii)  $x(0) > 0$ , (iii)  $k_s > 1$ , (iv)  $u \in [u_{\text{min}}, u_{\text{max}}] : u_{\text{min}}, u_{\text{max}} \geq 0$ , where  $u_{\text{min}}$  and  $u_{\text{max}}$  are the minimum and maximum dilution rates allowed, respectively, and (v) the substrate quantity  $\bar{s} \in [0, s_{\text{in}}]$  brought by a  $T$ -periodic dilution rate is equal to the quantity brought by some constant dilution rate  $\bar{u} \in [u_{\text{min}}, u_{\text{max}}] : \bar{u} < \mu_{\text{max}}$ . Under these assumptions, the goal is to find the optimal  $T$ -periodic waveforms,  $x^*$ ,  $s^*$ , and  $u^*$ , which satisfy the dynamical system equations (3.1a) and (3.1b) of the chemostat model governed by the Contois growth model (3.1c) and minimize the time-averaged substrate concentration. Such a problem can be described by the following finite-horizon optimal control problem: For a given time period  $T > 0$ , find the control variable  $u$  on the time interval  $[0, T]$  that minimizes the performance index

$$J(u) = \frac{1}{T} \mathcal{I}_T^{(t)} s \quad (3.2a)$$

subject to Eqs. (3.1a)-(3.1c),

$$0 \leq s \leq s_{\text{in}}, \quad u \in \mathcal{U}, \quad \frac{1}{T} \mathcal{I}_T^{(t)} u = \bar{u}, \quad (3.2b)$$

$$s(0) = s(T) = \bar{s}, \quad \text{and} \quad (3.2c)$$

$$x(0) = x(T),$$

and under Assumptions (i)-(v), where  $s$  and  $x$  are the state variables, and

$$\mathcal{U} = \{u : \mathbb{R}_0^+ \rightarrow [u_{\text{min}}, u_{\text{max}}] \text{ s.t. } u \text{ is measurable and } T\text{-periodic}\}.$$

To reduce the dimensionality of the optimal control problem, Bayen et al. [15] argued that all trajectories of Eqs. (3.1a) and (3.1b) converge asymptotically to the invariant set  $s + x = s_{\text{in}}$ , so we can reduce the coupled system of dynamic equations (3.1a) and (3.1b) into the single differential equation

$$\dot{s} = \psi, \quad (3.3)$$

where  $\psi = (u - v)(s_{\text{in}} - s)$  is the state derivative variable and  $v = \frac{\mu_{\text{max}} s}{k_s (s_{\text{in}} - s) + s}$ . Moreover, the non-trivial equilibrium solution  $\bar{s}$  of the differential equation  $\dot{s}|_{u=\bar{u}} = 0$  exists and is given by

$$\bar{s} = \frac{\bar{u} k_s s_{\text{in}}}{\bar{u}(k_s - 1) + \mu_{\text{max}}}. \quad (3.4)$$

The system in this case exhibits an over-yielding state in the sense that there exists  $u : J(u) < J(\bar{u}) = \bar{s}$ . The goal now is to find the optimal  $T$ -periodic waveforms,  $s^*$  and  $u^*$ , which minimize the averaged substrate concentration (3.2a) and satisfy the differential Eq. (3.3) together with Conditions (3.2b) and (3.2c). We refer to this problem by Problem  $\mathcal{P}$ . If we integrate both sides of Eq. (3.3) over the time interval  $\Omega_t \forall_s t \in \Omega_T \setminus \{0\}$ , we transform the optimal control problem into its integral form where the same performance index  $J$  is minimized subject to the integral equation

$$s(t) = \bar{s} + \mathcal{I}_t^{(x)} \psi, \quad (3.5)$$

and Conditions (3.2b) and (3.2c). We refer to this integral form of Problem  $\mathcal{P}$  by Problem  $\mathcal{IP}$ . Although Problems  $\mathcal{P}$  and  $\mathcal{IP}$  are mathematically equivalent, they are not necessarily numerically equivalent in floating-point arithmetic. In particular, while the numerical discretization of Problem  $\mathcal{P}$  entails the use of numerical differentiation operators known to be ill-conditioned as they could potentially lead to serious round-off errors, the numerical discretization of Problem  $\mathcal{IP}$  admits the use of numerical integration operators widely popular for being ‘well-conditioned operators,’ and ‘their well-conditioning is essentially unaffected for increasing number of points’; see [29, 30] and the Refs. therein.

#### 4. FPSI Matrices in Reduced Form

In this section we improve the recent formulas obtained by Elgindy [28] for the construction of FPSI matrices. The aim is to gain more accuracy and speed in approximating the integrations of periodic functions while reducing the computational complexity requisite. Using the Fourier quadrature rule

$$\mathcal{Q}_F(f) = \frac{T}{N} \sum_{j=0}^{N-1} f_j, \quad \forall f \in \mathbb{T}_T,$$

we can define the following discrete inner product

$$(u, v)_N = \frac{T}{N} \sum_{j=0}^{N-1} u_j v_j^*,$$

$\forall u, v \in \mathbb{C}$ , where  $v_j^*$  is the complex conjugate of  $v_j$ . Now, let  $I_N f$  be the  $N/2$ -degree,  $T$ -periodic Fourier interpolant that matches  $f$  at the set of nodes  $\mathbb{S}_N$  so that

$$I_N f(x) = \sum_{k=-N/2}^{N/2} \frac{\tilde{f}_k}{c_k} e^{i\omega_k x}, \quad (4.1)$$

where  $\omega_\alpha = \frac{2\pi\alpha}{T} \forall \alpha \in \mathbb{R}$ ,

$$c_k = \begin{cases} 1, & k \in \mathbb{K}_N'', \\ 2, & k = \pm \frac{N}{2}, \end{cases}$$

and  $\tilde{f}_k$  is the discrete Fourier interpolation coefficient given by

$$\tilde{f}_k = \frac{1}{T} (f, e^{i\omega_k x})_N = \frac{1}{N} \sum_{j=0}^{N-1} f_j e^{-i\omega_k x_{N,j}}, \quad \forall k \in \mathbb{K}_N.$$

Since

$$\tilde{f}_{k \pm N} = \frac{1}{N} \sum_{j=0}^{N-1} f_j e^{-i\omega_{k \pm N} x_{N,j}} = \frac{1}{N} \sum_{j=0}^{N-1} f_j e^{-i\omega_k x_{N,j}} e^{\mp i\omega_N x_{N,j}} = \frac{1}{N} \sum_{j=0}^{N-1} f_j e^{-i\omega_k x_{N,j}} e^{\mp 2\pi i j} = \frac{1}{N} \sum_{j=0}^{N-1} f_j e^{-i\omega_k x_{N,j}} = \tilde{f}_k,$$

then  $\tilde{f}_{N/2} = \tilde{f}_{-N/2}$ . Therefore, we can rewrite Eq. (4.1) in the following reduced form

$$I_N f(x) = \sum_{|k| \leq N/2} \tilde{f}_k e^{i\omega_k x}, \quad (4.2)$$



where the primed sigma denotes a summation in which the last term is omitted. We can now define the DFT pair by

$$\begin{cases} \tilde{f}_k = \frac{1}{N} \sum_{j=0}^{N-1} f_j e^{-i\omega_k x_{N,j}} = \frac{1}{N} \sum_{j=0}^{N-1} f_j e^{-i\hat{\omega}_j k}, & k \in \mathbb{K}'_N, \\ f_j = \sum'_{|k| \leq N/2} \tilde{f}_k e^{i\omega_k x_{N,j}} = \sum'_{|k| \leq N/2} \tilde{f}_k e^{i\hat{\omega}_j k}, & \forall j \in \mathbb{J}_N, \end{cases} \quad (4.3a)$$

where  $\hat{\omega}_k = 2\pi k/N \forall k$ . Substituting Eq. (4.3a) into Eq. (4.2), and then swapping the order of the summations, express the interpolant in the equivalent Lagrange form

$$I_N f(x) = \sum_{j=0}^{N-1} f_j \mathcal{F}_j(x), \quad (4.4)$$

where  $\mathcal{F}_j(x)$  is the trigonometric Lagrange interpolating polynomial given by

$$\mathcal{F}_j(x) = \frac{1}{N} \sum'_{|k| \leq N/2} e^{i\omega_k(x-x_{N,j})} = \left[ \frac{1}{N} \sin\left(\frac{\pi N}{T}(x-x_{N,j})\right) \cot\left(\frac{\pi}{T}(x-x_{N,j})\right) \right]_{x \neq x_{N,j}}, \quad j \in \mathbb{J}_N;$$

see [28]. Since  $\mathcal{F}_j(x_{N,l}) = \delta_{j,l} \forall j, l \in \mathbb{J}_N$ , where  $\delta_{j,l}$  is the kronecker delta function of variables  $j$  and  $l$ , one can easily write the vector of interpolant values at the grid points set  $\mathbb{S}_N$  using the writing conventions introduced in Section 2 as  $(I_N f)_{0:N-1} = f_{0:N-1}$ . We can also integrate  $I_N f$  over the interval  $\Omega_{x_{N,l}}$  through the formula

$$\mathcal{I}_{x_{N,l}}^{(x)}(I_N f) = \sum_{j=0}^{N-1} f_j \mathcal{I}_{x_{N,l}}^{(x)} \mathcal{F}_j = \sum_{j=0}^{N-1} \theta_{l,j} f_j, \quad \forall l \in \mathbb{J}_N, \quad (4.5)$$

where

$$\theta_{l,j} = \mathcal{I}_{x_{N,l}}^{(x)} \mathcal{F}_j = \frac{1}{N} \left[ x_{N,l} + \frac{Ti}{2\pi} \sum'_{\substack{|k| \leq N/2 \\ k \neq 0}} \frac{1}{k} e^{-i\omega_k x_{N,j}} (1 - e^{i\omega_k x_{N,l}}) \right], \quad l, j \in \mathbb{J}_N, \quad (4.6)$$

are the entries of the first-order square Fourier integration matrix (FIM),  $\Theta$ , of size  $N$ . Elgindy [28] pointed out further that when the calculation of  $\mathcal{I}_{y_{M,l}}^{(x)}(I_N f)$  is needed,  $\forall_s M$ -random set of points  $\{y_{M,0:M-1}\} \subset (0, T) : y_{M,l} \notin \mathbb{S}_N \forall M \in \mathbb{Z}^+, l \in \mathbb{J}_M$ , one can derive the elements formulas of the associated rectangular FIM,  $\hat{\Theta} = (\hat{\theta}_{l,j}), l \in \mathbb{J}_M, j \in \mathbb{J}_N$ , by performing the replacement  $x_{N,l} \leftarrow y_{M,l}$  in Formulas (4.6):

$$\hat{\theta}_{l,j} = \mathcal{I}_{y_{M,l}}^{(x)} \mathcal{F}_j = \frac{1}{N} \left[ y_{M,l} + \frac{Ti}{2\pi} \sum'_{\substack{|k| \leq N/2 \\ k \neq 0}} \frac{1}{k} e^{-i\omega_k x_{N,j}} (1 - e^{i\omega_k y_{M,l}}) \right], \quad l \in \mathbb{J}_M, j \in \mathbb{J}_N. \quad (4.7)$$

We can rewrite Formulas (4.5) and its variants

$$\mathcal{I}_{y_{M,l}}^{(x)}(I_N f) = \sum_{j=0}^{N-1} f_j \mathcal{I}_{y_{M,l}}^{(x)} \mathcal{F}_j = \sum_{j=0}^{N-1} \hat{\theta}_{l,j} f_j, \quad l \in \mathbb{J}_M,$$

which are consistent with the set  $\{y_{M,0:M-1}\}$  in matrix notation as

$$\begin{aligned} \mathcal{I}_{x_N}^{(x)}(I_N f) &= \Theta f_{0:N-1}, \\ \mathcal{I}_{y_M}^{(x)}(I_N f) &= \hat{\Theta} f_{0:N-1}, \end{aligned} \quad (4.8a)$$

respectively. In the special case when  $y_{M,l} = T$ , Formula (4.7) reduces to  $\hat{\theta}_{l,j} = T/N \forall j \in \mathbb{J}_N$ . For convenience, we denote  $\hat{\theta}_{l,j}$  by  $\theta_{N,j}$  in this particular case and define  $\Theta_N = \frac{T}{N} \mathbf{I}'_N$  so that

$$\mathcal{I}_T^{(x)}(I_N f) = \Theta_N f_{0:N-1} = \frac{T}{N} (\mathbf{I}'_N f_{0:N-1}). \quad (4.9)$$

The zeroth-rows of  $\Theta$  and  $\hat{\Theta}$  are zeros rows, and the matrix  $\Theta_{\bullet}$  is “a row-wise element-twins matrix” in the sense that each element in each row has exactly one twin element in the same row such that

$$\begin{aligned} \theta_{l,j} &= \theta_{l,l-j}, \quad \forall l = 1, \dots, N-1, \quad j = 0, \dots, \left\lfloor \frac{l-1}{2} \right\rfloor, \\ \theta_{l,N-j} &= \theta_{l,l+j}, \quad \forall l = 1, \dots, N-2, \quad j = 1, \dots, \left\lfloor \frac{N-l-1}{2} \right\rfloor; \end{aligned}$$

see [28, pp. 379-380]. This distinguished characteristic of  $\Theta_{\bullet}$  can be exploited to efficiently accelerate the construction of  $\Theta$  through Algorithm A.1 in Appendix A; the operations  $\odot$  and  $\oslash$  in the algorithm refer to the Hadamard product and division, respectively. It is noteworthy to mention that the rectangular matrix  $\Theta_{\bullet}$  has a  $T$ -invariant, 2-norm condition number  $\mathcal{K}_2 = \|\Theta_{\bullet}\| \|\Theta_{\bullet}^{\dagger}\| = O(N^{1.5})$ , for relatively large values of  $N$ , as clearly seen in Figure 1, where  $\Theta_{\bullet}^{\dagger}$  is the Moore-Penrose pseudoinverse of  $\Theta_{\bullet}$ .

#### 4.1. Computational Complexity and Speed

Most parts of Algorithm A.1 are optimized and arranged to work on chunks of vectors and matrices, thus their efficiency increases by allowing for vectorized operations. To analyze the computational cost of the algorithm, notice that the first 3 lines require 8 arithmetic operations. The Kronecker product in Line 4 requires  $N(N-1)$  multiplications, so the line requires  $1+3N(N-1)$  arithmetic operations. Line 6 requires 5 arithmetic operations. Line 8 requires  $3N-4$  operations. Line 10 requires  $1+\lfloor \frac{l+3}{2} \rfloor$  additions and subtractions. Line 13 requires  $3(N-1)$  arithmetic operations. Line 15 requires  $\lfloor \frac{N+3-l}{2} \rfloor - 1$  additions and subtractions, and Line 17 requires  $2N$  additions and multiplications. Therefore, the for loop in Lines 5 – 18 require

$$\begin{aligned} & \sum_{l=2}^{N-1} \left( \sum_{j=2}^{\lfloor \frac{l+3}{2} \rfloor} 3(N-1) + \left\lfloor \frac{1}{2}(-l+N+3) \right\rfloor + (3N-4) \left\lfloor \frac{l+3}{2} \right\rfloor + \left\lfloor \frac{l+3}{2} \right\rfloor + 2N+5 \right) + (3N-4) \left\lfloor \frac{N+3}{2} \right\rfloor \\ & + \left\lfloor \frac{N+3}{2} \right\rfloor + 2N+6 = 3(N-1) \left\lfloor \frac{N+3}{2} \right\rfloor + 2N+6 + \begin{cases} 0, & N=2, \\ \frac{3}{4}(N-2)(N(2N+7)+2), & N \geq 4, \end{cases} \end{aligned}$$

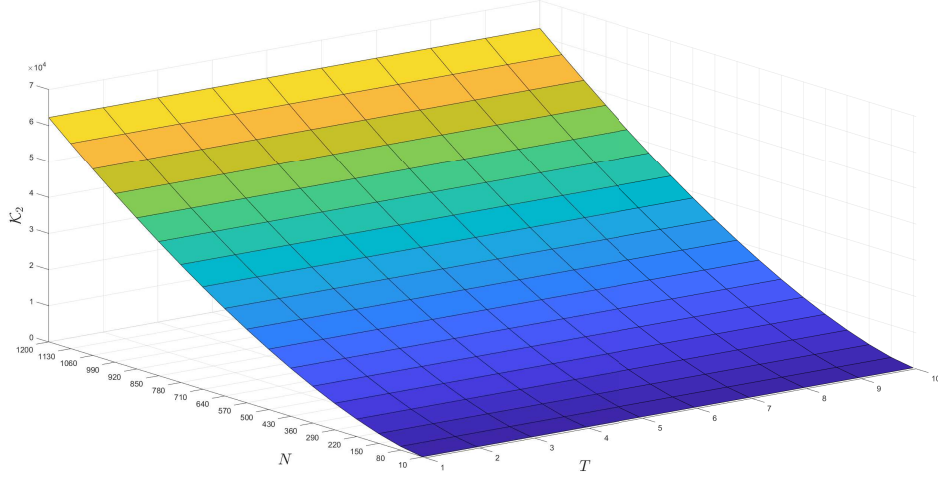
arithmetic operations. Since Line 19 requires  $N^2$  divisions, the exact total cost of the algorithm,  $\text{TC}_{\text{new}}$ , is

$$\text{TC}_{\text{new}} = 3(N-1) \left\lfloor \frac{N+3}{2} \right\rfloor + N(4N-1) + 15 + \begin{cases} 0, & N=2, \\ \frac{3}{4}(N-2)(N(2N+7)+2), & N \geq 4 \end{cases} = O\left(\frac{3}{2}N^3\right), \quad \text{as } N \rightarrow \infty.$$

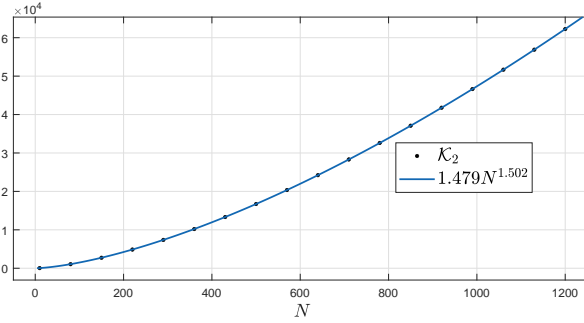
The operational count of [28, Algorithm 3.1] was roughly estimated to be of  $O(\frac{1}{2}N^3)$ , for large values of  $N$ , however, if we attempt to calculate its exact total cost,  $\text{TC}_{\text{old}}$ , we count 6 arithmetic operations in the precomputation of the constants  $\frac{Ti}{2\pi}$  and  $\frac{2\pi i}{T}$ . Line 3 of that algorithm would now require  $(11N+3) \left( \left\lfloor \frac{l-1}{2} \right\rfloor + 2 \right)$  arithmetic operations. Line 4 requires  $\left\lfloor \frac{l-1}{2} \right\rfloor + 1$  subtractions. Line 6 requires  $(11N+4) \left( \left\lfloor \frac{1}{2}(-l+N-1) \right\rfloor + 1 \right)$  arithmetic operations, and Line 7 requires  $2 \left\lfloor \frac{1}{2}(-l+n-1) \right\rfloor$  additions and subtractions. Therefore, a precise estimate of  $\text{TC}_{\text{old}}$  would be

$$\text{TC}_{\text{old}} = (11N+4) \left\lfloor \frac{N}{2} \right\rfloor + 11N+9 + \begin{cases} 0, & N=2, \\ \frac{1}{2}(N-2)((11N+38)N+8), & N \geq 4 \end{cases} = O\left(\frac{11}{2}N^3\right), \quad \text{as } N \rightarrow \infty.$$

Hence,  $\text{TC}_{\text{new}}/\text{TC}_{\text{old}} \sim 3/11 = 0.\overline{27}$ , i.e., the current algorithm requires about one-quarter of the total cost of the earlier algorithm. Indeed, Figure 2 shows a comparison between the elapsed time (ET) to perform [28, Direct Formulas (3.3) and Algorithm 3.1] and the current algorithm. The calculated execution times were measured multiple times and



(a)



(b)

Figure 1: Figure (a) shows a surface plot of  $\mathcal{K}_2$ , formed by joining adjacent point values of  $\mathcal{K}_2$  with straight lines, above a rectangular grid in the  $TN$ -plane generated using  $T = 1 : 10$  and  $N = 10(70)1200$ . Figure (b) shows a plot of  $\mathcal{K}_2$  and its power function least-squares fit of the form  $aN^b$  against  $N = 10(70)1200$ . The fitted coefficients have the 95% confidence bounds  $1.476 \leq a \leq 1.483$  and  $1.501 \leq b \leq 1.502$ .

the shown data are the median of the time measurements in seconds (s). For  $N = 200$ , the ET of [28, Algorithm 3.1],  $\text{ET}_{\text{old}}$ , took about 0.359 s, while the ET recorded for the current algorithm,  $\text{ET}_{\text{new}}$ , was about 0.084 s; thus,  $\text{ET}_{\text{new}}/\text{ET}_{\text{old}} \approx 0.234$ , as nearly expected. The results manifest clearly that the present algorithm is superior to [28, Direct Formulas (3.3) and Algorithm 3.1] in terms of speed and computational cost.

#### 4.2. Errors and Convergence Rates for Nonsmooth and Generally $T$ -Periodic Functions

In this section we study the errors and convergence rates of the truncated Fourier series, interpolation operators, and integration operators for nonsmooth and generally  $T$ -periodic functions. To this end, let  $\beta = [-\beta, \beta] \forall \beta > 0$ ,  $\mathbf{C}_{T,\beta} = \{x + iy : x \in \Omega_T, y \in \beta\} \forall \beta > 0$ ,  $C^n(\Omega_T)$  be the space of  $n$  times continuously differentiable functions on  $\Omega_T \forall n \in \mathbb{Z}_0^+$ ,  $L^p(\Omega_T)$  is the Banach space of measurable functions  $u$  defined on  $\Omega_T$  such that  $\|u\|_{L^p} = (\int_{\Omega} |u|^p)^{1/p} < \infty$ , and  $H^s(\Omega_T) = \{u \in L_{loc}(\Omega_T), D^\alpha u \in L^2(\Omega_T), |\alpha| \leq s\} \forall s \in \mathbb{Z}_0^+$  is the inner product space with the inner product  $(u, v)_s = \sum_{|\alpha| \leq s} \mathcal{I}_{\Omega_T}^{(x)}(D^\alpha u D^\alpha v)$ , where  $L_{loc}(\Omega_T)$  is the space of locally integrable functions on  $\Omega_T$  and  $D^\alpha u$  denotes any derivative of  $u$  with multi-index  $\alpha$ . Let also  $\mathcal{H}_T^s = \{u \in H^s(\Omega_T), u^{(s)} \in BV, u^{(0:s-1)}(0) = u^{(0:s-1)}(T)\}$ , where  $BV = \{u \in L^1(\Omega_T) : \|u\|_{BV} < \infty\}$  with the norm  $\|u\|_{BV} = \sup \{\mathcal{I}_T^{(x)}(u\phi'), \phi \in \mathcal{D}(\Omega_T), \|\phi\|_{L^\infty} \leq 1\}$  such that  $\mathcal{D}(\Omega_T) = \{u \in C^\infty(\Omega_T) : \text{supp}(u) \text{ is a compact subset of } \Omega_T\}$ . For convenience of writing, we shall denote  $\|\cdot\|_{L^2(\Omega_T)}$  and  $e^{i\omega_k x}$  by  $\|\cdot\|$  and  $\phi_k(x) \forall k$ , respectively.



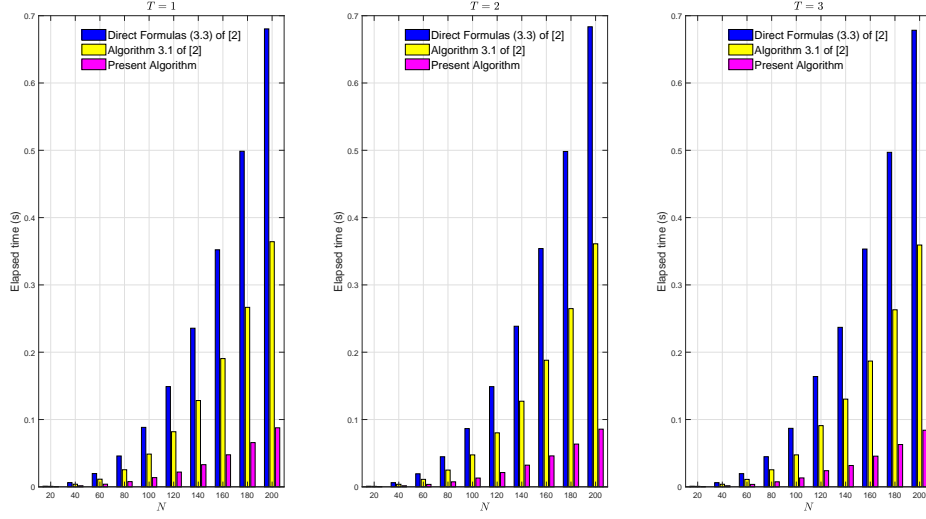


Figure 2: Three bar graphs illustrating the elapsed times of constructing  $\Theta$  using [28, Direct Formulas (3.3) and Algorithm 3.1] and the present algorithm, for  $T = 1 : 3$  and  $N = 20(20)200$ .

We shall first derive the decay rate of Fourier series coefficients for functions in  $\mathcal{H}_T^s \forall s \in \mathbb{Z}_0^+$ . Note that functions in this space are  $T$ -periodic and continuous (but nonsmooth) for  $s \geq 1$ . However, functions in  $\mathcal{H}_T^0$  may neither be  $T$ -periodic nor continuous.

**Theorem 4.1** (Decay of Fourier Series Coefficients for nonsmooth and generally  $T$ -periodic functions). *Suppose that  $f \in \mathcal{H}_T^s \forall s \in \mathbb{Z}_0^+$  is approximated by the  $N/2$ -degree,  $T$ -periodic truncated Fourier series*

$$\Pi_N f(x) = \sum_{|k| \leq N/2} \hat{f}_k \phi_k(x), \quad \forall s \in \mathbb{Z}_e^+, \quad (4.10)$$

where  $\hat{f}_{-N/2:N/2}$  is the Fourier series coefficients vector of  $f$ , then

$$|\hat{f}_k| = O(|k|^{-s-1}), \quad \text{as } |k| \rightarrow \infty. \quad (4.11)$$

*Proof.* Notice first that the set of complex exponentials  $\{\phi_{-N/2:N/2}\}$  is orthogonal on  $\Omega_T$  with respect to the weight function  $w(x) = 1 \forall x \in \Omega_T$  such that  $(\phi_n, \phi_m) = \mathcal{I}_T^{(x)}(\phi_n \phi_m^*) = T \delta_{n,m}$ , where  $\delta_{n,m}$  is the Kronecker delta function defined by

$$\delta_{n,m} = \begin{cases} 1, & n = m, \\ 0, & n \neq m. \end{cases}$$

Therefore,  $(\phi_n, \phi_n) = \mathcal{I}_T^{(x)}(\phi_n \phi_n^*) = \mathcal{I}_T^{(x)}(|\phi_n|^2) = \|\phi_n\|^2 = T$ . Fourier coefficients,  $\hat{f}_k$ , of  $f$  can thus be determined via the orthogonal projection  $(f, \phi_k)$ , which produces

$$\hat{f}_k = \frac{1}{T}(f, \phi_k) = \frac{1}{T} \mathcal{I}_T^{(x)}(f \phi_k) = \begin{cases} \frac{1}{T} \mathcal{I}_T^{(x)}(f \mathbb{1}_x - i\beta \mathbb{1}_{\phi_{-k}} \mathbb{1}_x - i\beta \mathbb{1}) \forall k \geq 0, \\ \frac{1}{T} \mathcal{I}_T^{(x)}(f \mathbb{1}_x + i\beta \mathbb{1}_{\phi_{-k}} \mathbb{1}_x + i\beta \mathbb{1}) \forall k < 0 \end{cases} = \begin{cases} \frac{e^{-\omega k \beta}}{T} \mathcal{I}_T^{(x)}(f \mathbb{1}_x - i\beta \mathbb{1}_{\phi_{-k}}) \forall k \geq 0, \\ \frac{e^{-\omega -k \beta}}{T} \mathcal{I}_T^{(x)}(f \mathbb{1}_x + i\beta \mathbb{1}_{\phi_{-k}}) \forall k < 0. \end{cases} \quad (4.12)$$

Through Eq. (4.12) and integration by parts, we have

$$\hat{f}_k = \frac{1}{T} \mathcal{I}_T^{(x)}(f \phi_{-k}) = \frac{1}{T(i\omega_k)^s} \mathcal{I}_T^{(x)}(f^{(s)} \phi_{-k}) = \frac{1}{T(i\omega_k)^{s+1}} \mathcal{I}_T^{(x)}(f^{(s)} \phi'_{-k}) \forall k \in \mathbb{K}_N \setminus \{0\} \Rightarrow |\hat{f}_k| \leq \frac{\|f^{(s)}\|_{BV}}{T \omega_{|k|}^{s+1}}, \quad \forall k \in \mathbb{K}_N \setminus \{0\}, \quad (4.13)$$

from which the Asymptotic Formula (4.11) immediately follows. Further,  $\hat{f}_0 = \frac{1}{T} \mathcal{I}_T^{(x)} f$ , i.e.,  $\hat{f}_0$  is the average value of

the function. □

We refer to the upper bound (4.13) by the “Fourier coefficients upper bounds for nonsmooth and  $T$ -periodic functions.”

**Theorem 4.2** (Fourier truncation error for nonsmooth and generally  $T$ -periodic functions). *Suppose that  $f \in \mathcal{H}_T^s \forall s \in \mathbb{Z}_0^+$  is approximated by the  $N/2$ -degree,  $T$ -periodic truncated Fourier series (4.10), then*

$$\|f - \Pi_N f\| = O(N^{-s-1/2}), \quad \text{as } N \rightarrow \infty.$$

*Proof.* Observe first that

$$\|f - \Pi_N f\|^2 = \mathcal{I}_T^{(x)} \left( \sum_{|k|>N/2} \hat{f}_k \phi_k \sum_{|l|>N/2} \hat{f}_l^* \phi_{-l} \right) = \sum_{|k|>N/2} \sum_{|l|>N/2} \hat{f}_k \hat{f}_l^* \mathcal{I}_T^{(x)} \phi_{k-l} = \sum_{|k|>N/2} \sum_{|l|>N/2} \hat{f}_k \hat{f}_l^* (\phi_k, \phi_l) = T \sum_{|k|>N/2} |\hat{f}_k|^2. \quad (4.14)$$

Through Eq. (4.13) and Ineq. (4.14), we have

$$\begin{aligned} \|f - \Pi_N f\|^2 &= T \sum_{|k|>N/2} |\hat{f}_k|^2 \leq \frac{1}{T} \|f^{(s)}\|_{BV}^2 \sum_{|k|>N/2} \omega_k^{-2s-2} \leq \frac{2}{T} \|f^{(s)}\|_{BV}^2 \mathcal{I}_{N/2, \infty}^{(x)} \omega_x^{-2s-2} = \frac{\|f^{(s)}\|_{BV}^2}{(2s+1)\pi\omega_{N/2}^{2s+1}} \quad \forall N \in \mathbb{Z}_e^+. \\ \Rightarrow \|f - \Pi_N f\| &\leq \frac{\|f^{(s)}\|_{BV}}{\sqrt{(2s+1)\pi\omega_{N/2}^{2s+1}}} \quad \forall N \in \mathbb{Z}_e^+. \end{aligned} \quad (4.15)$$

□

**Theorem 4.3** (Fourier aliasing error for nonsmooth and  $T$ -periodic functions). *Suppose that  $f \in \mathcal{H}_T^s \forall s \in \mathbb{Z}^+$  is approximated by the  $T$ -periodic Fourier interpolant  $I_N f \forall N \in \mathbb{Z}_e^+$ , then*

$$\|E_N f\| = O(N^{-s-1/2}), \quad \text{as } N \rightarrow \infty. \quad (4.16)$$

*Proof.* Replacing  $f$  in (4.3a) by its Fourier series yields

$$\tilde{f}_k = \frac{1}{N} \sum_{j=0}^{N-1} \left[ \sum_{l \in \mathbb{Z}} \hat{f}_l \phi_l(x_j) \right] \phi_{-k}(x_j) = \sum_{l \in \mathbb{Z}} \hat{f}_l \left[ \frac{1}{N} \sum_{j=0}^{N-1} \phi_{l-k}(x_j) \right] = \left[ \sum_{l \in \mathbb{Z}} \hat{f}_l \delta_{l-k, pN} \right]_{|p| \in \mathbb{Z}_0^+} = \hat{f}_k + \sum_{p \in \mathbb{Z}_\neq} \hat{f}_{k+pN}, \quad \forall k \in \mathbb{K}'_N. \quad (4.17)$$

Formula (4.17) and the Triangle Difference Ineq. imply that

$$\begin{aligned} \|\|E_N f\| - \|\hat{f}_{N/2} \phi_{N/2}\|\|^2 &\leq \|E_N f - \hat{f}_{N/2} \phi_{N/2}\|^2 = \mathcal{I}_T^{(x)} \left( \sum'_{|k| \leq N/2} \sum_{p \in \mathbb{Z}_\neq} \hat{f}_{k+pN} \phi_k \cdot \sum'_{|l| \leq N/2} \sum_{p \in \mathbb{Z}_\neq} \hat{f}_{l+pN}^* \phi_{-l} \right) \\ &= \sum'_{|k| \leq N/2} \sum'_{|l| \leq N/2} \sum_{p \in \mathbb{Z}_\neq} \hat{f}_{k+pN} \sum_{p \in \mathbb{Z}_\neq} \hat{f}_{l+pN}^* \mathcal{I}_T^{(x)} \phi_{k-l} = \sum'_{|k| \leq N/2} \left| \sum_{p \in \mathbb{Z}_\neq} \hat{f}_{k+pN} \right|^2 \|\phi_k\|^2 = T \sum'_{|k| \leq N/2} \left| \sum_{p \in \mathbb{Z}_\neq} \hat{f}_{k+pN} \right|^2 \\ &\leq T \sum'_{|k| \leq N/2} \sum_{p \in \mathbb{Z}_\neq} |\hat{f}_{k+pN}|^2. \end{aligned} \quad (4.18)$$

From Ineqs. (4.13) and (4.18), we find that

$$\begin{aligned}
\|E_N f\| - \|\hat{f}_{N/2} \phi_{N/2}\| &\leq T \sum'_{|k| \leq N/2} \sum_{p \in \mathbb{Z}_e^+} |\hat{f}_{k+pN}|^2 \leq \frac{\|f^{(s)}\|_{BV}^2}{T} \sum'_{|k| \leq N/2} \sum_{p \in \mathbb{Z}_e^+} \omega_{|k+pN|}^{-2s-2} \\
&= \frac{\|f^{(s)}\|_{BV}^2}{T} \left[ 2 \sum_{k=0}^{N/2} \sum_{p \in \mathbb{Z}_e^+} \omega_{|k+pN|}^{-2s-2} - \sum_{p \in \mathbb{Z}_e^+} (\omega_{|pN|}^{-2s-2} + \omega_{|N/2+pN|}^{-2s-2}) \right] \\
&\leq \frac{\|f^{(s)}\|_{BV}^2}{T} \left[ 2 \omega_1^{-2s-2} \sum_{k=0}^{N/2} \frac{1}{N^{2s+2}} \sum_{p \geq 1} \left( \frac{1}{(p-1/2)^{2s+2}} + \frac{1}{p^{2s+2}} \right) - \omega_N^{-2s-2} \left( \sum_{p \geq 1} \left( \frac{1}{(p-1/2)^{2s+2}} + \frac{2}{p^{2s+2}} + \frac{1}{(p+1/2)^{2s+2}} \right) \right) \right] \\
&= \frac{\|f^{(s)}\|_{BV}^2}{T} \left[ (N+2)\zeta(2s+2)\omega_{N/2}^{-2s-2} - (2\zeta(2s+2) - 1)\omega_{N/2}^{-2s-2} \right] = \frac{1}{\pi} \left( \zeta(2s+2) + \frac{1}{N} \right) \|f^{(s)}\|_{BV}^2 \omega_{N/2}^{-2s-1} \quad \forall N \in \mathbb{Z}_e^+,
\end{aligned}$$

where  $\zeta$  is the Riemann zeta function. Therefore,

$$\|E_N f\| - \|\hat{f}_{N/2} \phi_{N/2}\| \leq \sqrt{\frac{1}{\pi} \left( \zeta(2s+2) + \frac{1}{N} \right)} \|f^{(s)}\|_{BV} \omega_{N/2}^{-s-1/2} \quad \forall N \in \mathbb{Z}_e^+.$$

Since  $\|\hat{f}_{N/2} \phi_{N/2}\| = \sqrt{T} |\hat{f}_{N/2}| \leq \frac{\|f^{(s)}\|_{BV}}{\sqrt{T} \omega_{N/2}^{s+1}}$  by Ineq. (4.13), then

$$\|E_N f\| \leq \|\hat{f}_{N/2} \phi_{N/2}\| + \|E_N f - \hat{f}_{N/2} \phi_{N/2}\| \leq \frac{1}{\sqrt{\pi}} \left( \sqrt{\zeta(2s+2) + \frac{1}{N}} + \frac{1}{\sqrt{N}} \right) \|f^{(s)}\|_{BV} \omega_{N/2}^{-s-1/2}, \quad (4.19)$$

whence the Asymptotic Formula (4.16) is obtained.  $\square$

Since  $\zeta(s) < \frac{1}{1-2^{1-s}} \forall s > 2$ ; cf. [31], then the aliasing error is roughly bounded by

$$\|E_N f\| < \frac{1}{\sqrt{\pi}} \left( \sqrt{1 + \frac{1}{2^{2s+1}-1}} + \frac{1}{N} + \frac{1}{\sqrt{N}} \right) \|f^{(s)}\|_{BV} \omega_{N/2}^{-s-1/2} \sim \sqrt{\frac{2^{2s+1}}{\pi(2^{2s+1}-1)}} \|f^{(s)}\|_{BV} \omega_{N/2}^{-s-1/2}, \quad \text{as } N \rightarrow \infty.$$

Theorem 4.3 manifests that the aliasing error is comparable to Fourier series truncation error. The next corollary shows that Fourier interpolation error is also comparable to Fourier series truncation error.

**Corollary 4.1** (Fourier interpolation error for nonsmooth and  $T$ -periodic functions). *Suppose that  $f \in \mathcal{H}_T^s \forall s \in \mathbb{Z}^+$  is approximated by the  $T$ -periodic Fourier interpolant  $I_N f \forall N \in \mathbb{Z}_e^+$ , then*

$$\|f - I_N f\| = O(N^{-s-1/2}), \quad \text{as } N \rightarrow \infty.$$

*Proof.* Ineqs. (4.15) and (4.19) yield

$$\begin{aligned}
\|f - I_N f\|^2 &= \|f - \Pi_N f\|^2 + \|E_N f\|^2 \leq \frac{\|f^{(s)}\|_{BV}^2}{(2s+1)\pi \omega_{N/2}^{2s+1}} + \frac{1}{\pi} \left( \sqrt{\zeta(2s+2) + \frac{1}{N}} + \frac{1}{\sqrt{N}} \right)^2 \|f^{(s)}\|_{BV}^2 \omega_{N/2}^{-2s-1} \\
&\Rightarrow \|f - I_N f\| \leq v_{1,s,N} \|f^{(s)}\|_{BV} \omega_{N/2}^{-s-1/2} \\
&< v_{2,s,N} \|f^{(s)}\|_{BV} \omega_{N/2}^{-s-1/2} \sim v_{3,s} \|f^{(s)}\|_{BV} \omega_{N/2}^{-s-1/2}, \quad \text{as } N \rightarrow \infty,
\end{aligned} \quad (4.20)$$

where

$$\begin{aligned} \nu_{1,s,N} &= \sqrt{\frac{1}{\pi} \left[ \frac{1}{2s+1} + \left( \sqrt{\zeta(2s+2)} + \frac{1}{N} + \frac{1}{\sqrt{N}} \right)^2 \right]}, \\ \nu_{2,s,N} &= \sqrt{\frac{1}{\pi} \left[ \frac{1}{2s+1} + \left( \sqrt{1 + \frac{1}{2^{2s+1}-1}} + \frac{1}{N} + \frac{1}{\sqrt{N}} \right)^2 \right]}, \quad \text{and} \\ \nu_{3,s} &= \sqrt{\frac{1}{\pi} \left( 1 + \frac{1}{2s+1} + \frac{1}{2^{2s+1}-1} \right)}. \end{aligned}$$

□

**Corollary 4.2** (FPSQ error for nonsmooth and  $T$ -periodic functions). *Suppose that  $f \in \mathcal{H}_T^s \forall s \in \mathbb{Z}^+$  is approximated by the  $T$ -periodic Fourier interpolant  $I_N f \forall N \in \mathbb{Z}_e^+$ , then*

$$\left| \mathcal{I}_{x_N}^{(x)} f - \Theta f_{0:N-1} \right| = O\left(N^{-s-1/2} I_N\right), \quad \text{as } N \rightarrow \infty. \quad (4.21)$$

*Proof.* The Triangle Ineq. implies

$$\left| \mathcal{I}_{x_N}^{(x)} f - \Theta f_{0:N-1} \right| = \left| \mathcal{I}_{x_N}^{(x)} f - \mathcal{I}_{x_N}^{(x)}(I_N f) + \mathcal{I}_{x_N}^{(x)}(I_N f) - \Theta f_{0:N-1} \right| \leq \left| \mathcal{I}_{x_N}^{(x)} f - \mathcal{I}_{x_N}^{(x)}(I_N f) \right| + \left| \mathcal{I}_{x_N}^{(x)}(I_N f) - \Theta f_{0:N-1} \right|. \quad (4.22)$$

The proof is established through Ineqs. (4.20) and (4.22) together with Schwarz's Ineq. by realizing that

$$\begin{aligned} \left| \mathcal{I}_{x_N}^{(x)} f - \Theta f_{0:N-1} \right| &\leq \left| \mathcal{I}_{x_N}^{(x)} f - \mathcal{I}_{x_N}^{(x)}(I_N f) \right| + \left| \mathcal{I}_{x_N}^{(x)}(I_N f) - \Theta f_{0:N-1} \right| \leq \|f - I_N f\| \sqrt{\mathbf{x}_N} \\ &\leq \nu_{1,s,N} \|f^{(s)}\|_{BV} \omega_{N/2}^{-s-1/2} \sqrt{\mathbf{x}_N} < \nu_{2,s,N} \|f^{(s)}\|_{BV} \omega_{N/2}^{-s-1/2} \sqrt{\mathbf{x}_N} \sim \nu_{3,s} \|f^{(s)}\|_{BV} \omega_{N/2}^{-s-1/2} \sqrt{\mathbf{x}_N}, \quad \text{as } N \rightarrow \infty. \end{aligned}$$

□

Corollary 4.2 shows that

$$\left\| \mathcal{I}_{x_N}^{(x)} f - \Theta f_{0:N-1} \right\|_2 \leq \nu_{1,s,N} \|f^{(s)}\|_{BV} \omega_{N/2}^{-s-1/2} \left\| \sqrt{\mathbf{x}_N} \right\|_2 \quad (4.23a)$$

$$< \nu_{2,s,N} \|f^{(s)}\|_{BV} \omega_{N/2}^{-s-1/2} \left\| \sqrt{\mathbf{x}_N} \right\|_2 \quad (4.23b)$$

$$\sim \nu_{3,s} \|f^{(s)}\|_{BV} \omega_{N/2}^{-s-1/2} \left\| \sqrt{\mathbf{x}_N} \right\|_2, \quad \text{as } N \rightarrow \infty. \quad (4.23c)$$

We refer to the upper bounds (4.23a), (4.23b), and (4.23c) by the “FPSQ-NSTP error norm upper bound,” “relaxed FPSQ-NSTP error norm upper bound,” and “asymptotic FPSQ-NSTP error norm upper bound,” respectively, or collectively by the “FPSQ error norm upper bounds for nonsmooth and  $T$ -periodic functions.” Notice that each of the error factors  $\nu_{1,s,N}$ ,  $\nu_{2,s,N}$ , and  $\nu_{3,s}$  is a monotonically decreasing function for increasing values of  $s$ , indicating that the smoother the function, the faster the error convergence rate. All quadrature error upper bounds demonstrate that FPSQ approximation for nonsmooth and  $T$ -periodic functions has “a polynomial order accuracy.”

To sense how the smoothness of the function can influence the FPSQ error, consider the FPSQ approximations of the periodic extensions of the five polynomial functions  $f_s \in \mathcal{H}_1^s$ ,  $s = 1, 2, \dots, 5$ , defined by

$$\begin{aligned} f_1(x) &= x(1-x), \quad f_2(x) = \frac{1}{3}x^3 - \frac{1}{2}x^2 + \frac{1}{6}x + 1, \quad f_3(x) = x^4 - 2x^3 + x^2, \quad f_4(x) = -x^5 + \frac{15}{6}x^4 - \frac{5}{3}x^3 + \frac{1}{6}x + 2, \\ \text{and } f_5(x) &= -x^6 + 3x^5 - \frac{5}{2}x^4 + \frac{1}{2}x^2 - 1. \end{aligned}$$

The periodic extension of each function  $f_s$  has a jump discontinuity in the  $s$ th-derivative, for  $s = 1 : 5$ . Therefore, Corollary 4.2 anticipates the decay rate of FPSQ error of each function  $f_s$  to be of  $O(N^{-s-1/2})$ , as  $N \rightarrow \infty \forall s = 1 : 5$ .

Figure 3 shows the infinity- and Euclidean-error norms in log-lin scale of the FPSQ approximations of the five periodic functions. We can clearly see that the calculated FPSQ errors remain below the estimated upper bounds in all cases with faster decay rates for smoother functions, which is in whole consistent with Corollary 4.2. The figure also shows the fitted curves of the FPSQ Euclidean-error norms in the power function model form  $y = bx^m$ . Taking the natural logarithm of both sides of the equation gives the equivalent log-log regression model  $\ln y = m \ln x + \ln b$ , which has the form of the linear regression model  $Y = mX + B$  using the change of variables  $X = \ln x$  and  $Y = \ln y$  and the parameter

substitution  $B = \ln b$ . The parameters  $m$  and  $b$  of the latter model were obtained using MATLAB polynomial curve fitting function “polyfit” with the observed data  $\{(X_i, Y_i)\}_{i=1}^{10} = \left\{ \ln N_i, \ln \left\| \mathcal{I}_{x_{N_i}}^{(x)} f - \Theta_{f_{0:N_i-1}} \right\| \right\}_{i=0}^{10}$ , for  $N_i = 10(10 + i) \forall i$ . The estimated  $m$ -values were  $-1.5, -2.5, -3.5, -4.5$ , and  $-5.57$  in close agreement with Corollary 4.2.

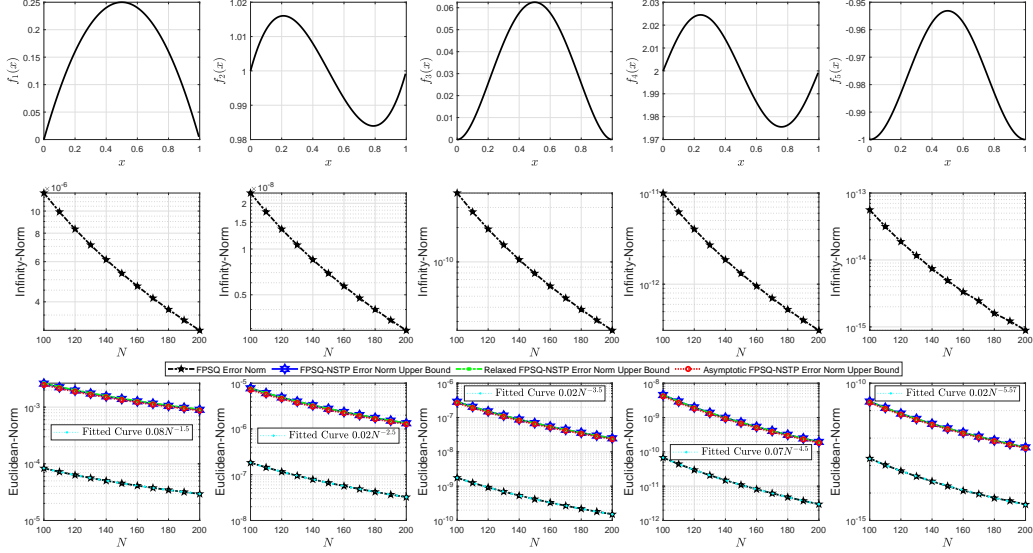


Figure 3: The first row of the figure shows the five polynomial functions  $f_1(x) = x(1-x)$ ,  $f_2(x) = \frac{1}{3}x^3 - \frac{1}{2}x^2 + \frac{1}{6}x + 1$ ,  $f_3(x) = x^4 - 2x^3 + x^2$ ,  $f_4(x) = -x^5 + \frac{15}{6}x^4 - \frac{5}{3}x^3 + \frac{1}{6}x + 2$ , and  $f_5(x) = -x^6 + 3x^5 - \frac{5}{2}x^4 + \frac{1}{2}x^2 - 1$  on the interval  $[0, 1]$ . The infinity- and Euclidean-error norms in log-lin scale of the FPSQ approximations of each function are shown in the second- and -third rows of the same column, respectively, against  $N = 100(10)200$ . All FPSQ error norm upper bounds are shown in the last row of plots as well as the fitted curve of the FPSQ Euclidean-error norms obtained using MATLAB.

To sense how the lack of continuity of the function can influence the FPSQ error, consider the FPSQ approximations of the square wave function  $f_6 \in \mathcal{H}_1^1$  defined in one period by

$$f_6(x) = \begin{cases} 1, & 0 \leq x < \frac{1}{2} \vee x = 1, \\ 0, & \frac{1}{2} \leq x < 1. \end{cases}$$

The function and its  $N/2$ -degree, 1-periodic Fourier interpolant, for  $N = 10, 20, 40$ , and  $80$  are depicted in Figure 4. We can see spurious oscillations throughout most of the interval with large peaks near the jump discontinuities giving rise to the well known Gibbs phenomenon, which often occurs in Fourier series expansions and interpolations of discontinuous data. Adding more terms to the Fourier interpolant slowly decreases the error away from the discontinuities, but the over- and undershoots will remain visible to the naked eye and ultimately compress into a single vertical line at the points of discontinuity as  $N \rightarrow \infty$ . The largest amount of over- or undershoot in the Fourier interpolant  $I_N(x)$ , for  $N = 10(10)80$ , when evaluated at  $10,000$  equally-spaced nodes between  $0$  and  $1$  are about  $12.3\%$ ,  $14.3\%$ ,  $13.9\%$ ,  $14.2\%$ ,  $14.0\%$ ,  $14.1\%$ ,  $14.1\%$ , and  $14.1\%$  of the jump size, respectively. These over- and undershoot factors are slightly larger than the classical asymptotic overshoot factor arising in Fourier expansion series, which approaches  $8.95\%$  of the jump size. The contrast between the over- and undershoot factors associated with Fourier interpolation and that of classical Gibbs phenomenon is no surprise as Fourier interpolation computations in finite-precision arithmetic are subject to aliasing and round-off errors. In fact, it was discovered more than a quarter century ago that the behavior of the Fourier interpolant near an isolated jump discontinuity point  $\xi$  of a function depends on the position of  $\xi$  with respect to the interpolation nodes considered; cf. [32]. Besides this point, Figure 4 also shows the magnitude of the symmetric discrete Fourier interpolation coefficients against their indices, where the

coefficients with even indices vanish. The fitted curves of the discrete data  $\left\{ \left( 1 : 2 : \frac{N}{2} - 1, \left| \tilde{f}_{1:2:\frac{N}{2}-1} \right| \right) \right\}$  using the power function model  $y = bx^m$  manifest that the coefficients decay like  $O(k^{-1})$  as indicated by Theorem 4.1. The FPSQ error Euclidean-norm decays like  $O(N^{-1/2})$  as revealed by another curve fit obtained through MATLAB. This result is in agreement with the Asymptotic Formula (4.21) although the theoretical proof of Corollary 4.2 does not apply to this case.

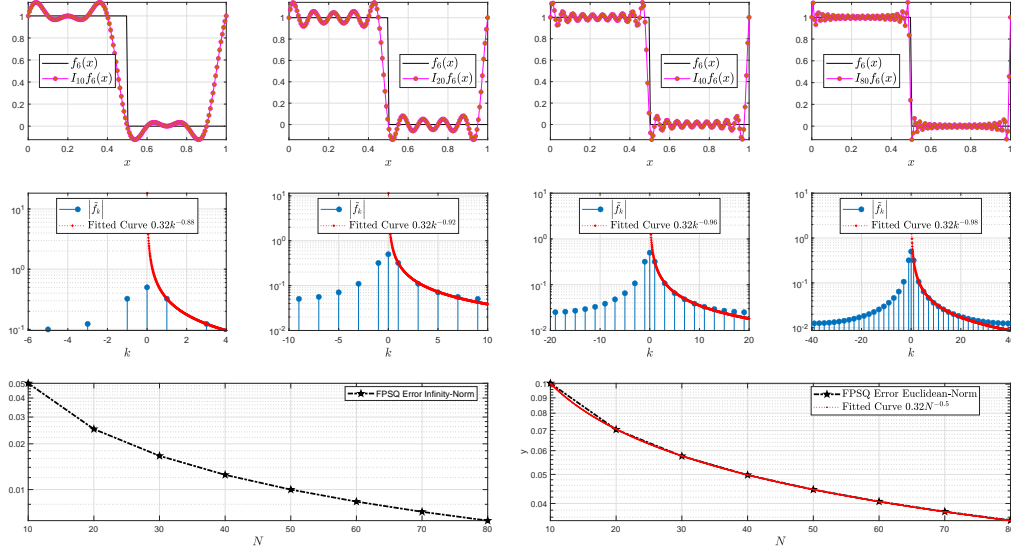


Figure 4: The figure shows the square wave function  $f_6$  and its  $N/2$ -degree,  $T$ -periodic Fourier interpolant  $I_N(x)$ , for  $N = 10, 20, 40$ , and  $80$ . The plots of  $I_N(x)$  were produced using 150 linearly spaced nodes between 0 and 1. The second row shows stem plots of the Fourier interpolation coefficients magnitudes against their indices in log-lin scale together with the fitted curves of the odd-indexed right half discrete data obtained through MATLAB. The last row displays the FPSQ error infinity- and -Euclidean norms in log-lin scale in addition to the fitted curve obtained from the latter experimental error data.

## 5. Behavior of Fourier Interpolants at Jump Discontinuities

The variance between the asymptotic overshoot factors of Fourier interpolants and that of Fourier expansion series is not the only distinctive difference in their behaviors; in fact, there is another remarkable difference that seemingly did not attract much attention in the literature: their behavior at a jump discontinuity! While it is well known that the classical Fourier expansion series converges to the average value of the left- and right-hand limits of the function at a jump discontinuity point  $\xi$ , to the best of our knowledge, the behavior of Fourier interpolant at  $\xi$  was not investigated clearly in the literature. We shall confine our study on  $T$ -periodic piecewise constant functions with two jump discontinuity points in  $\Omega_T$  and study the behavior of Fourier interpolants of their periodic extensions on  $\mathbb{R}_0^+$  at the jump discontinuities. The motivation for this study is the fact that the optimal control of Problem  $\mathcal{P}$  is a bang-bang controller that switches abruptly between two states at two switching times; cf. [15]. We refer to the jump discontinuity points in  $(0, T)$  and at the boundary point  $x = T$  by the interior- and boundary-jump discontinuity points, respectively. Now, consider the 1-periodic, piecewise constant functions  $f_j \in \mathcal{H}_1^0$ , for  $j = 6 : 12$ , where  $f_7, \dots, f_{12}$  are given by

$$f_7(x) = \begin{cases} 1, & 0 \leq x < \frac{1}{3}, \\ 0, & \frac{1}{3} \leq x < 1, \end{cases} \quad f_8(x) = \begin{cases} 4, & 0 \leq x < \frac{2}{3}, \\ 0, & \frac{2}{3} \leq x < 1, \end{cases} \quad f_9(x) = \begin{cases} -5, & 0 \leq x < 0.8183, \\ 0, & 0.8183 \leq x < 1, \end{cases}$$

$$f_{10}(x) = \begin{cases} 2, & 0 \leq x < \frac{\pi}{5}, \\ 1, & \frac{\pi}{5} \leq x < \frac{\pi}{4}, \\ 2, & \frac{\pi}{4} \leq x < 1, \end{cases} \quad f_{11}(x) = \begin{cases} 10, & 0 \leq x < \frac{\epsilon}{5}, \\ -2, & \frac{\epsilon}{5} \leq x < \frac{\epsilon}{3}, \\ 10, & \frac{\epsilon}{3} \leq x < 1. \end{cases} \quad \text{and } f_{12}(x) = \begin{cases} -3, & 0 \leq x < \ln 1.5, \\ 2, & \ln 1.5 \leq x < \ln 2, \\ -3, & \ln 2 \leq x < 1. \end{cases}$$



The set of functions  $\{f_{7,9}\}$  is created by various translations of the interior jump discontinuity point or different scalings of the square wave function  $f_6$ , so each function has exactly one interior jump discontinuity point and one boundary jump discontinuity point in  $\Omega_1$ . The rest of the functions have both jump discontinuity points of interior type. Table 1 shows the observed Fourier interpolant approximations at the interior jump discontinuity points of each function, for several increasing values of  $N$ . For  $f_6$ , the interpolant converges to zero at  $\xi = 1/2 \forall N$ , since  $\xi$  always belong to the set of interpolation nodes. On the other hand, each of the interpolants values of  $f_7$  and  $f_8$  appear to swing back and forth among three different limiting values, including the zero value when  $\xi$  conforms with one of the interpolation nodes. Interestingly enough, the sum of each three interpolant values at the jump discontinuity point corresponding to any three consecutive  $N$ -values having a fixed step-size of power of 10 (nearly) equals the jump size at  $\xi \forall \xi$  function! For the rest of the functions, the interpolants do not show any signs of convergence to a single or even to a finite set of multiple values! In all cases where the jump discontinuity point  $\xi$  does not coincide with any interpolation node, the value of Fourier interpolant falls within the open interval  $(f(\xi^-), f(\xi^+))$ , where  $\xi^-$  and  $\xi^+$  are points infinitesimally to the left and right of  $\xi$ , respectively. These results manifest that Fourier interpolant diverges at  $\xi$ , except when the jump discontinuity point  $\xi$  coincides with an interpolation node, where Fourier interpolant matches the value of the discontinuous function by the interpolation condition.

Table 1: Observed Fourier interpolant values at a discontinuity point rounded to 4 decimal digits.

$N$	$I_N f_6(1/2)$	$I_N f_7(1/3)$	$I_N f_8(2/3)$	$I_N f_9(0.8183)$	$I_N f_{10}(\pi/5)$	$I_N f_{10}(\pi/4)$	$I_N f_{11}(e/5)$	$I_N f_{11}(e/3)$	$I_N f_{12}(\ln 1.5)$	$I_N f_{12}(\ln 2)$
100	0	0.6887	1.2253	-0.7210	1.1430	1.5554	5.8852	5.5461	-0.2099	0.5742
200	0	0.3101	2.7694	-1.5989	1.3162	1.0614	0.8580	0.2428	-2.6403	-1.2379
300	0	0.0000	0.0000	-2.5714	1.5021	1.6352	9.1071	8.3030	0.2979	-2.7950
400	0	0.6905	1.2332	-3.5372	1.6956	1.1289	4.5168	3.1217	-2.2202	0.8602
500	0	0.3094	2.7663	-4.3962	1.8709	1.7281	-0.2953	-1.5870	0.8087	-0.9315
600	0	0.0000	0.0000	-0.0705	1.0062	1.2070	8.0419	6.1515	-1.7527	-2.5647
700	0	0.6907	1.2343	-0.7931	1.1475	1.8107	3.1736	0.8337	1.2771	1.1385
800	0	0.3092	2.7656	-1.6890	1.3231	1.2936	-1.3221	8.8158	-1.2407	-0.6059
900	0	0.0000	0.0000	-2.6705	1.5145	1.8857	6.8532	3.7869	1.6919	-2.3100
1000	0	0.6908	1.2347	-3.6347	1.7066	1.3811	1.8420	-1.1351	-0.7053	1.4047
1100	0	0.3092	2.7652	-4.4817	1.8786	1.9541	9.8124	6.7762	-2.9592	-0.2798
1200	0	0.0000	0.0000	-0.1455	1.0125	1.4733	5.5581	1.4333	-0.1601	-2.0377
1300	0	0.6909	1.2349	-0.8961	1.1549	1.0124	0.5913	9.2934	-2.5944	1.6498
1400	0	0.3091	2.7650	-1.8090	1.3326	1.5675	8.8764	4.4389	0.3703	0.0462
1500	0	0.0000	0.0000	-2.7937	1.5265	1.0751	4.2180	-0.6410	-2.1657	-1.7483
2000	0	0.3090	2.7648	-1.9186	1.3424	1.8277	6.5636	-0.1144	1.7384	0.6675
3000	0	0.0000	0.0000	-0.3859	1.0324	1.1638	-1.7335	1.0356	-1.1057	-0.1592
4000	0	0.6910	1.2354	-4.1556	1.7555	1.6077	2.2617	2.2785	1.4404	-1.0144
5000	0	0.3090	2.7645	-2.5008	1.3923	1.9936	6.9655	3.5769	-1.4988	-1.8295
10000	0	0.6911	1.2356	0.0000	1.8453	1.9870	3.1116	9.4607	0.3689	-0.3355

## 6. Detecting the Jump Discontinuities and Reconstructing the Discontinuous Function

Detecting the jump discontinuity points in the optimal control of Problem  $\mathcal{P}$  is a crucial step and an essential prerequisite to obtain accurate approximations to the solutions of the problem. In fact, the discontinuity points of the controller are not known a priori; therefore, we need to estimate their locations from the Fourier interpolant approximation. To this end, we present a novel accurate and efficient edge detection method that can estimate the locations of the desired discontinuities for piecewise constant functions with two jump discontinuities in  $\Omega_T$ . The proposed method is inspired by the fact that the horizontal extension of the Gibbs phenomenon is reduced as the number of spectral terms grows, but the ultimate graph of Fourier interpolant in the close vicinity of a jump discontinuity point  $\xi$  turns into a jagged line on both sides of  $\xi$  and passes in almost a vertical direction through a point whose abscissa is  $\xi$  and ordinate falls within the open interval  $(f(\xi^-), f(\xi^+))$ , except when  $\xi$  exist at an interpolation point where Fourier interpolant matches the function value at  $\xi$ . Therefore, the location of  $\xi$  is gradually squeezed between the locations of the sharp spikes and eventually falls (almost) at the midpoint between the two abscissas whose ordinates are the peak and the bottom out of the two jagged lines enclosing  $\xi$ , as  $N \rightarrow \infty$ . Hence, the peculiar manner in which Fourier interpolant behaves near a jump discontinuity point provides an excellent means of detecting one. We present a brief description of this method in what follows.

### 6.1. Implementation of the Edge Detection Strategy

Given a piecewise constant function  $f \in \mathcal{H}_T^0 : f(0) = f(T)$  with two jump discontinuity points in  $\Omega_T$ , start by constructing its Fourier interpolant  $I_N f$  and determine its extreme values on  $\Omega_T$ . To this end, we evaluate  $I_N f$  at a set of equally-spaced nodes  $\mathbb{S}_M = \{y_{M,0:M-1}\} \forall_s$  relatively large  $M \in \mathbb{Z}^+$ . Next, we find  $d_{\max} := \text{indmax } I_N f(y_M)$

and  $d_{\min} := \text{indmin } I_N f(y_M)$ . To refine the obtained approximations to the extreme values, we extremize  $I_N f$  on the relatively small uncertainty intervals  $[y_{M,d_{\max}-1}, y_{M,d_{\max}+1}]$  and  $[y_{M,d_{\min}-1}, y_{M,d_{\min}+1}]$ , respectively. For this task, we prefer to apply the recent fast line search method known by the Chebyshev PS line search method (CPSLSM); cf. [33]. Let  $I_N^{\max} f$  and  $I_N^{\min} f$  be the maximum and minimum values of  $I_N f$  obtained by the CPSLSM, respectively. The next step is to set up the straight line  $y = I_N^{\text{ave}} f = \frac{1}{2} (I_N^{\max} f + I_N^{\min} f)$  whose ordinate is the average value of the calculated extreme values; we call this line the “*separation line*,” as we shall use it later to separate the Fourier interpolant values into two groups of discrete data. For now, we choose a user-defined tolerance  $\epsilon$ , and form the “*user-defined discontinuity feasible zone*”—basically a narrow strip centered about the separation line with radius  $\epsilon$ , where any Fourier interpolant value within an  $\epsilon$ -distance from the separation line is recognized as a possible Fourier interpolant value paired with an estimated discontinuity point  $\tilde{\xi}$  that is sufficiently close to a true discontinuity point  $\xi$ . Our rationale here is simple: “*while the Fourier interpolant at a discontinuity point  $\xi$  is not necessarily equal to the average of the left and right limits at  $\xi$ , as verified by Table 1, it is less likely that the Fourier interpolant at a continuity point to be exactly equal to the average of the left and right limits at  $\xi$ .*” We expect to have at most a single approximate discontinuity point near each discontinuity point, since the graph of Fourier interpolant moves in virtually a vertical direction through each point whose abscissa is a discontinuity point, so that the Fourier interpolant values at the interpolation points that are not sufficiently close to a discontinuity point are expected to live outside the user-defined discontinuity feasible zone, for relatively small  $\epsilon$ . For a certain tolerance  $\epsilon$ , we refer to this zone by “*the  $\epsilon$ -discontinuity feasible zone*,” and denote it by  $Z_\epsilon^{\text{disc}}$ . We prefer to set the  $\epsilon$ -value to within a relatively small length of “*the local extremeshoot height*<sup>5</sup>” such that  $\epsilon = \tilde{\epsilon} (I_N^{\max} f - I_N^{\min} f) \forall \tilde{\epsilon} \in (0, 0.01]$ . Now, let  $\Xi = \{\tilde{\xi}_{1:L}\}$  be the set of approximate discontinuity points collected at this step  $\forall_s L \in \{1, 2\}$ . If  $L = 2$ , i.e., the method determines two approximate discontinuity points, then we consider the method successful and terminate the procedure at this step. Otherwise, we create the “*discontinuity auxiliary function  $I_N^{\text{aux}} f$* ,” which is a two-state, piecewise constant function whose two states are the obtained extreme values of  $I_N f$  such that

$$I_N^{\text{aux}} f(y_{M,l}) = \begin{cases} I_N^{\min} f, & I_N f(y_{M,l}) < I_N^{\text{ave}} f, \\ I_N^{\max} f, & I_N f(y_{M,l}) > I_N^{\text{ave}} f, \end{cases} \quad \forall l \in \mathbb{J}_M^+. \quad (6.1)$$

Since the function  $f$  switches its state abruptly at a discontinuity point  $\xi$ , we expect  $\xi$  to occur sufficiently close to the two consecutive interpolation points whose ordinates lie closely above and below the separation line. To find these points, we find the two-elements index vector  $J_{1:2} : I_N^{\text{aux}} f(y_{M,J_1}) - I_N^{\text{aux}} f(y_{M,J_1+1}) \neq 0 \forall l = 1, 2$ . Now, the desired discontinuity points  $\xi_1$  and  $\xi_2$  either exist in the closed intervals  $[y_{M,J_1}, y_{M,J_1+1}]$  and  $[y_{M,J_2}, y_{M,J_2+1}]$  or occur in close proximity of their boundaries. To account for both scenarios, denote the boundary points  $y_{M,J_1}, y_{M,J_1+1}, y_{M,J_2}$ , and  $y_{M,J_2+1}$  by  $b_j \forall j = 1 : 4$ , respectively. If the set  $\Xi$  is empty, we estimate  $\xi_1$  and  $\xi_2$  by the midpoints of the two intervals such that  $\tilde{\xi}_l = \frac{1}{2}(b_{2l} - b_{2l-1}) \forall l = 1, 2$ . On the other hand, if the set  $\Xi$  contains already one of the two discontinuity points, say  $\xi_1$ , then we drop the interval which either includes  $\xi_1$  or whose boundaries are closely adjacent to  $\xi_1$ . We can then estimate  $\xi_2$  by bisecting the remaining interval. That is, we can calculate  $\tilde{\xi}_2$  by the formula

$$\tilde{\xi}_2 = \begin{cases} \frac{1}{2}(b_2 - b_1), & \text{if } b_1 - \tilde{\xi}_1 > \varepsilon \vee \tilde{\xi}_1 - b_2 > \varepsilon, \\ \frac{1}{2}(b_4 - b_3), & \text{otherwise,} \end{cases}$$

$\forall_s$  relatively small positive number  $\varepsilon < T/M$ . As a further correction step in practice, an estimated discontinuity point is assigned the value  $T$  if its location is within a sufficiently small distance from  $x = T$ . For a relatively large value of  $M$ , we may reasonably set the estimated discontinuity point equal to  $T$  when  $J_2 = M - 1$ . A graphical illustration of the method is depicted in Figure 5, for  $M = 200$ ,  $\epsilon = 0.5\% (I_N^{\max} f - I_N^{\min} f)$ , and  $\varepsilon = T/(2M)$ . Table 2 shows the observed relative errors in the estimated jump discontinuity points of the functions  $f_6, \dots, f_{12}$  using  $M \in \{100, 400\}$  and the same  $\epsilon$ - and  $\varepsilon$ -values. We notice from the table that, for a certain  $N$ -value, the relative errors often drop-off when  $M$  increases; roughly speaking, the estimated interior discontinuity points approximate the true ones to two-three and three-five significant digits for  $M = 100$  and 400, respectively. On the other hand, for a certain  $M$ -value, the relative errors may slightly decrease at the beginning for increasing  $N$ -values, but (almost) cease to fall beyond a certain level as  $N$  grows larger, in general, except for  $\xi_1 = 0.5$  of  $f_6$ , where the error drops to zero abruptly at  $(N, M) = (200, 100)$  and  $(500, 400)$  and sustains at this level for growing values of  $N$ . In all cases, the method locates the exact boundary jump discontinuity point perfectly whenever exists.

Now that we know how to detect the discontinuity points with plausible accuracy, it remains one final question before we end this section: how can we quickly reconstruct the discontinuous function from the PS data? A possible answer to this question turns out to be quite simple and does not really require much effort after recovering the discontinuity points within satisfactory precision. In fact, the key to the answer lies again in the separation line

<sup>5</sup>The extremeshoot height refers to the vertical distance between the maximum overshoot and the minimum undershoot of the signal near a discontinuity.

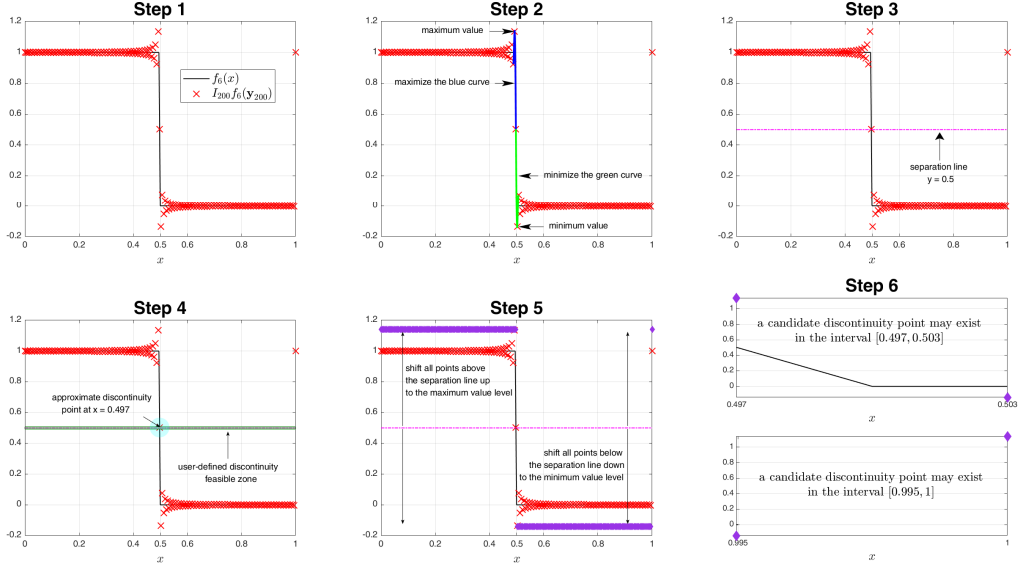


Figure 5: The necessary steps to locate the discontinuity points of the wave function  $f_6$  through the proposed edge detection method. In the first step the method calculates the Fourier interpolant  $I_{200}f_6$  at the equally-spaced nodes  $y_{200} = x_{200}$  and sets  $y_{200,200} = y_{200,0}$ . In Step 2, the indices of the extreme values of  $I_{200}f_6(y_{200})$  are determined (99 and 101 in this case); these extreme values specify the parts of the graph of  $I_{200}f_6$  to be extremized using the CPSLSM (the blue and green curves in the plot whose domains are the narrow intervals  $[0.487, 0.497]$  and  $[0.497, 0.508]$ , respectively). In Step 3, the separation line  $y = I_N^{\text{ave}} f_6 = 0.5$  is installed by averaging the determined extreme values from the previous step (the extreme values were found to be 1.14116 and  $-0.14116$ ). Interpolation points are deemed approximate discontinuity points in Step 4 if their ordinates fall within the boundaries of roughly  $\mathcal{Z}_{0.0064}^{\text{disc}}$ ; the method stops at this step if two estimates are found (only one estimate  $\xi_1 \approx 0.497$  was recorded here with ordinate 0.503). Otherwise, the discontinuity auxiliary function  $I_N^{\text{aux}} f_6$  is derived in Step 5 by shifting all points above and below the separation line to the extreme values levels  $y = 1.14116$  and  $y = -0.14116$ . The range analysis of  $I_N^{\text{aux}} f_6$  gives birth to the two intervals  $[0.497, 0.503]$  and  $[0.995, 1]$  in step 6, which may contain the discontinuity points or their boundaries are sufficiently close to them. The midpoints of these two intervals are considered estimates to the the discontinuity points, except when  $J_2 = M - 1$ , or when an approximate discontinuity point that was discovered in Step 4 either exist in one interval, or occurs in the vicinity of one of its boundaries. In this example, the midpoints of both intervals are abandoned, since  $\xi_1 = 0.497 \in [0.497, 0.503]$  and  $J_2 = 199$ , so we set  $\xi_2 = 1$ .

$y = I_N^{\text{ave}} f$ . In particular, the Fourier interpolant values are divided into two groups of discrete data by this line: one group containing all Fourier interpolant values above the separation line and occur almost entirely close to the upper state level of the discontinuous function, say  $\mathbb{F}\mathbb{I}^{\text{u}}$ , and another group containing all Fourier interpolant values below the separation line and mainly appear close to the lower state level of the discontinuous function, say  $\mathbb{F}\mathbb{I}^{\text{d}}$ , except near the discontinuity points  $\xi_1$  and  $\xi_2$ , where the Fourier interpolant values in each group are vastly larger or smaller than the other values in the same set. This motivates us to measure the central tendency of each data group using the median, which is less liable to be distorted by outliers than the mean. To this end, let  $\check{f}_{N,M}^{\text{max}}$  and  $\check{f}_{N,M}^{\text{min}}$  be the medians of the two sets of Fourier interpolant values,  $\mathbb{F}\mathbb{I}^{\text{u}}$  and  $\mathbb{F}\mathbb{I}^{\text{d}}$ , and define the approximate discontinuous function  $\check{f}_{N,M}$  by

$$\check{f}_{N,M}(t) = \begin{cases} \check{f}_{N,M}^{\text{max}}, & 0 \leq t < \check{\xi}_1 \vee \check{\xi}_2 \leq t \leq T, \\ \check{f}_{N,M}^{\text{min}}, & \check{\xi}_1 \leq t < \check{\xi}_2, \end{cases}$$

if  $I_N f(0) \in \mathbb{F}\mathbb{I}^{\text{u}}$ , or by

$$\check{f}_{N,M}(t) = \begin{cases} \check{f}_{N,M}^{\text{min}}, & 0 \leq t < \check{\xi}_1 \vee \check{\xi}_2 \leq t \leq T, \\ \check{f}_{N,M}^{\text{max}}, & \check{\xi}_1 \leq t < \check{\xi}_2, \end{cases}$$

otherwise. A pseudocode for the construction of  $\check{f}_{N,M}$  from the PS data is presented in Algorithm A.2. Table 3 shows the small absolute errors in the estimated extreme values of the discontinuous functions  $f_6, \dots, f_{12}$  using  $M \in \{100, 400\}$ , for increasing values of  $N$ . Figures 6-12 also show snapshots of the approximate discontinuous functions  $\check{f}_{6,N,M}, \dots, \check{f}_{12,N,M}$  over one period using  $M = 400$ , for increasing values of  $N$ , where  $\check{f}_{j,N,M}$  denotes the approximate discontinuous function  $(\check{f}_j)_{N,M} \forall j$ .

Table 2: Observed relative errors in the estimated discontinuity points using  $M = 100$  and  $M = 400$ . All approximations are rounded to six significant digits.

$N$	$f_6$		$f_7$		$f_8$		$f_9$		$f_{10}$		$f_{11}$		$f_{12}$		
	$ \xi_1 - \hat{\xi}_1 _r$	$ \xi_2 - \hat{\xi}_2 _r$	$ \xi_1 - \hat{\xi}_1 _r$	$ \xi_2 - \hat{\xi}_2 _r$	$ \xi_1 - \hat{\xi}_1 _r$	$ \xi_2 - \hat{\xi}_2 _r$	$ \xi_1 - \hat{\xi}_1 _r$	$ \xi_2 - \hat{\xi}_2 _r$	$ \xi_1 - \hat{\xi}_1 _r$	$ \xi_2 - \hat{\xi}_2 _r$	$ \xi_1 - \hat{\xi}_1 _r$	$ \xi_2 - \hat{\xi}_2 _r$	$ \xi_1 - \hat{\xi}_1 _r$	$ \xi_2 - \hat{\xi}_2 _r$	
$M = 100$	100	1.01010E-02	0	1.51515E-02	0	7.57576E-03	0	6.31637E-03	0	1.13102E-02	3.27207E-03	5.98232E-03	2.26636E-03	8.94233E-03	1.77161E-03
	200	0	0	1.51515E-02	0	7.57576E-03	0	6.31637E-03	0	4.76605E-03	3.27207E-03	5.98232E-03	2.26636E-03	8.94233E-03	1.77161E-03
	300	0	0	1.51515E-02	0	7.57576E-03	0	6.02752E-03	0	4.76605E-03	3.27207E-03	5.98232E-03	2.26636E-03	8.94233E-03	1.77161E-03
	400	0	0	1.51515E-02	0	7.57576E-03	0	6.02752E-03	0	4.76605E-03	3.27207E-03	5.98232E-03	2.26636E-03	8.94233E-03	1.77161E-03
	500	0	0	1.51515E-02	0	7.57576E-03	0	6.02752E-03	0	4.76605E-03	3.27207E-03	5.98232E-03	2.26636E-03	8.94233E-03	1.77161E-03
	600	0	0	1.51515E-02	0	7.57576E-03	0	6.31637E-03	0	4.76605E-03	3.27207E-03	5.98232E-03	2.26636E-03	8.94233E-03	1.77161E-03
	700	0	0	1.51515E-02	0	7.57576E-03	0	6.31637E-03	0	4.76605E-03	3.27207E-03	5.98232E-03	2.26636E-03	8.94233E-03	1.77161E-03
	800	0	0	1.51515E-02	0	7.57576E-03	0	6.31637E-03	0	4.76605E-03	3.27207E-03	5.98232E-03	2.26636E-03	8.94233E-03	1.77161E-03
	900	0	0	1.51515E-02	0	7.57576E-03	0	6.02752E-03	0	4.76605E-03	3.27207E-03	5.98232E-03	2.26636E-03	8.94233E-03	1.77161E-03
	1000	0	0	1.51515E-02	0	7.57576E-03	0	6.02752E-03	0	4.76605E-03	3.27207E-03	5.98232E-03	2.26636E-03	8.94233E-03	1.77161E-03
	1100	0	0	1.51515E-02	0	7.57576E-03	0	6.02752E-03	0	4.76605E-03	3.27207E-03	5.98232E-03	2.26636E-03	8.94233E-03	1.77161E-03
	1200	0	0	1.51515E-02	0	7.57576E-03	0	6.31637E-03	0	4.76605E-03	3.27207E-03	5.98232E-03	2.26636E-03	8.94233E-03	1.77161E-03
	1300	0	0	1.51515E-02	0	7.57576E-03	0	6.31637E-03	0	4.76605E-03	3.27207E-03	5.98232E-03	2.26636E-03	8.94233E-03	1.77161E-03
	1400	0	0	1.51515E-02	0	7.57576E-03	0	6.02752E-03	0	4.76605E-03	3.27207E-03	5.98232E-03	2.26636E-03	8.94233E-03	1.77161E-03
	1500	0	0	1.51515E-02	0	7.57576E-03	0	6.02752E-03	0	4.76605E-03	3.27207E-03	5.98232E-03	2.26636E-03	8.94233E-03	1.77161E-03
$M = 400$	100	1.00251E-02	0	3.75940E-03	0	1.87970E-03	0	3.06798E-03	0	4.78300E-03	4.02499E-04	2.67893E-03	8.70828E-05	1.73431E-03	3.37813E-03
	200	5.01253E-03	0	3.75940E-03	0	1.87970E-03	0	5.20671E-06	0	7.94154E-04	3.59358E-03	1.93109E-03	2.67893E-03	4.44690E-03	2.37647E-04
	300	5.01253E-03	0	3.75940E-03	0	1.87970E-03	0	5.20671E-06	0	7.94154E-04	4.02499E-04	2.67893E-03	8.70828E-05	1.73431E-03	3.85342E-03
	400	2.50627E-03	0	3.75940E-03	0	1.87970E-03	0	5.20671E-06	0	7.94154E-04	4.02499E-04	1.93109E-03	8.70828E-05	4.44690E-03	2.37647E-04
	500	0	0	3.75940E-03	0	1.87970E-03	0	5.20671E-06	0	7.94154E-04	4.02499E-04	1.93109E-03	8.70828E-05	1.73431E-03	2.37647E-04
	600	0	0	3.75940E-03	0	1.87970E-03	0	5.20671E-06	0	7.94154E-04	4.02499E-04	2.67893E-03	8.70828E-05	1.73431E-03	2.37647E-04
	700	0	0	3.75940E-03	0	1.87970E-03	0	5.20671E-06	0	7.94154E-04	4.02499E-04	1.93109E-03	8.70828E-05	1.73431E-03	2.37647E-04
	800	0	0	3.75940E-03	0	1.87970E-03	0	5.20671E-06	0	7.94154E-04	4.02499E-04	1.93109E-03	8.70828E-05	1.73431E-03	2.37647E-04
	900	0	0	3.75940E-03	0	1.87970E-03	0	5.20671E-06	0	7.94154E-04	4.02499E-04	2.67893E-03	8.70828E-05	1.73431E-03	2.37647E-04
	1000	0	0	3.75940E-03	0	1.87970E-03	0	5.20671E-06	0	7.94154E-04	4.02499E-04	1.93109E-03	8.70828E-05	1.73431E-03	2.37647E-04
	1100	0	0	3.75940E-03	0	1.87970E-03	0	5.20671E-06	0	7.94154E-04	4.02499E-04	2.67893E-03	8.70828E-05	1.73431E-03	2.37647E-04
	1200	0	0	3.75940E-03	0	1.87970E-03	0	5.20671E-06	0	7.94154E-04	4.02499E-04	1.93109E-03	8.70828E-05	1.73431E-03	2.37647E-04
	1300	0	0	3.75940E-03	0	1.87970E-03	0	5.20671E-06	0	7.94154E-04	4.02499E-04	1.93109E-03	8.70828E-05	1.73431E-03	2.37647E-04
	1400	0	0	3.75940E-03	0	1.87970E-03	0	5.20671E-06	0	7.94154E-04	4.02499E-04	2.67893E-03	8.70828E-05	1.73431E-03	2.37647E-04
	1500	0	0	3.75940E-03	0	1.87970E-03	0	5.20671E-06	0	7.94154E-04	4.02499E-04	1.93109E-03	8.70828E-05	1.73431E-03	2.37647E-04

\*  $|\cdot|_r$  gives the relative error, and the letter E stands for power of 10.

## 7. Accurate Computation of Definite Integrals of Reconstructed Discontinuous Functions from the FPS Data

A practical difficulty with the Fourier collocation of Problem  $\mathcal{IP}$  at the mesh point set  $\mathbb{S}_N$  is the well recovery of the  $N$  definite integrals of the nonlinear state derivative variable  $\psi$  over the intervals  $\Omega_{x_n} \forall n \in \mathbb{J}_N$ . A similar goal is sought whilst the evaluation of the definite integral of the approximate substrate concentration  $\bar{s}$  over  $\Omega_T$ . Notice that  $\psi$  is a  $T$ -periodic function, since it is a composition of the  $T$ -periodic functions  $s$  and  $u$ ; thus, it is possible to estimate the required integrals using FPSQs. However,  $\psi$  is generally a piecewise discontinuous function due to the presence of the bang–bang controller  $u$ , so the FPSQ error Euclidean-norm of  $\psi$  decays like  $O(N^{-1/2})$  as discussed in Section 4.2, assuming that both  $u$  and  $s$  are computed using exact arithmetic. Table 4 asserts this finding as it shows that the calculated absolute errors in the definite integrals of  $f_6, \dots, f_{12}$  decay, at best, like  $O(N^{-1/2})$ , when they are approximated by FPSQs using the reconstructed  $\check{f}_{6,N,M}, \dots, \check{f}_{12,N,M}$  obtained by Algorithm A.2 with  $M = 100$  and  $M = 400$ . In practice, the expected poor convergence rate of FPSQ in computing the required integrals of  $\psi$ , after its successful application to recover the approximate discontinuous controller  $\check{u}_{N,M}$  through Algorithm A.2, motivates us to seek an alternative strategy to evaluate the sought integrals efficiently and with higher accuracy.

To refine the required integral approximations and improve the convergence rate, an alternative approach in lieu of using FPSQs, after utilizing them to determine  $\check{u}_{N,M}$ , is to numerically piecewise integrate  $\psi$  using quadratures of Gauss-type. In particular, since the optimal controller switches between two predefined states at two unspecified time instances in  $\Omega_T$ , the idea is to estimate these two time instances and then partition the time interval  $\Omega_T$  into generally three subintervals determined by the estimated time instances over which the restricted  $\psi$  on each subinterval is smooth. The application of Gauss quadrature over each subinterval is optimal in this case in the sense that it requires the smallest number of points to calculate the exact integration of the highest possible order polynomial. In fact, an  $n$ -point Gaussian quadrature rule is exact for polynomials of degree at most  $2n - 1$ .

Suppose now that we collocated Problem  $\mathcal{IP}$  using Fourier collocation, constructed the Fourier interpolant  $I_N u$  through either (4.2) or (4.4), estimated the jump discontinuity points  $\xi_1$  and  $\xi_2$  of the optimal control  $u$  by  $\tilde{\xi}_1$  and  $\tilde{\xi}_2$  through Algorithm A.2, and finally established the piecewise function  $\check{u}_{N,M}$  whose pieces are defined over the three subintervals  $\Omega_{\tilde{\xi}_1}, [\tilde{\xi}_1, \tilde{\xi}_2]$ , and  $[\tilde{\xi}_2, T]$ . Motivated by the need to successively integrate the composite function  $\psi$ , we

Table 3: Observed absolute errors in the estimated extreme values using  $M = 100$  and  $M = 400$ . All approximations are rounded to 5 significant digits.

$N$	$ f_6^{\max} - \hat{f}_{k,N,M}^{\max} $	$ f_6^{\min} - \hat{f}_{k,N,M}^{\min} $	$ f_7^{\max} - \hat{f}_{7,N,M}^{\max} $	$ f_7^{\min} - \hat{f}_{7,N,M}^{\min} $	$ f_8^{\max} - \hat{f}_{8,N,M}^{\max} $	$ f_8^{\min} - \hat{f}_{8,N,M}^{\min} $	$ f_9^{\max} - \hat{f}_{9,N,M}^{\max} $	$ f_9^{\min} - \hat{f}_{9,N,M}^{\min} $	$ f_{10}^{\max} - \hat{f}_{10,N,M}^{\max} $	$ f_{10}^{\min} - \hat{f}_{10,N,M}^{\min} $	$ f_{11}^{\max} - \hat{f}_{11,N,M}^{\max} $	$ f_{11}^{\min} - \hat{f}_{11,N,M}^{\min} $	$ f_{12}^{\max} - \hat{f}_{12,N,M}^{\max} $	$ f_{12}^{\min} - \hat{f}_{12,N,M}^{\min} $
$M = 100$														
100	0	5.46088E-03	0	4.49677E-03	0	4.50457E-04	2.49110E-05	0	0	3.35184E-05	0	9.11425E-05	4.12214E-03	0
200	4.99626E-03	4.99873E-03	0	2.51316E-03	9.32089E-03	3.03750E-02	4.89755E-02	3.53520E-03	4.95266E-04	2.28608E-02	7.44350E-03	1.73682E-03	1.45449E-02	1.81804E-02
300	0	0	0	0	0	0	3.02093E-02	0	0	0	0	0	3.25348E-03	3.96128E-03
400	0	7.93199E-05	3.28370E-03	1.05061E-03	1.43522E-03	7.84150E-03	3.91300E-02	1.86406E-03	7.36512E-05	2.06300E-03	8.31750E-03	3.33354E-02	1.22597E-02	1.66248E-03
500	0	6.65826E-05	1.49456E-05	1.68377E-05	9.26264E-05	1.13569E-03	2.86345E-02	0	0	7.84322E-03	0	1.80370E-03	1.90864E-03	2.03980E-04
600	1.39572E-03	1.60546E-03	0	0	0	0	5.36424E-03	0	0	8.76537E-05	1.73440E-03	0	6.07519E-03	6.45157E-03
700	0	5.86112E-05	0	5.43198E-05	0	6.00823E-05	3.87591E-04	0	0	3.66535E-04	1.92613E-04	4.75528E-03	1.73308E-03	0
800	0	5.54328E-05	2.61831E-04	1.14336E-04	5.59091E-04	5.05955E-03	1.03214E-02	2.92815E-04	1.01803E-04	4.36209E-03	1.77192E-03	9.55560E-03	3.90087E-03	3.24764E-04
900	0	0	0	0	0	0	2.41966E-05	0	0	0	0	0	0	0
1000	3.82151E-04	5.23656E-04	6.24540E-04	1.30314E-04	1.57500E-04	1.16577E-04	1.00520E-02	0	6.35917E-06	2.48792E-03	8.63638E-04	1.46659E-04	8.34752E-03	7.09763E-04
1100	0	0	0	0	0	0	0	0	0	0	0	0	0	0
1200	0	0	0	0	0	0	4.11854E-03	0	0	1.76179E-05	0	9.28325E-05	1.26346E-04	0
1300	0	3.65047E-05	0	7.18113E-05	0	5.71562E-05	8.10304E-05	0	0	7.69238E-05	0	2.75065E-04	6.27262E-04	0
1400	1.42066E-04	2.31099E-04	0	3.46255E-05	1.88635E-04	1.18611E-03	6.31568E-03	1.56579E-04	0	3.65358E-04	1.22283E-04	1.18564E-03	1.61653E-05	1.02878E-04
1500	0	8.64334E-05	0	0	0	0	1.35611E-03	0	0	5.89476E-04	0	7.21775E-04	5.77529E-05	0
2000	0	5.10837E-05	1.52090E-05	1.07136E-05	8.96558E-05	3.63116E-04	6.37900E-05	0	0	3.81931E-04	0	1.51160E-04	2.17857E-06	0
3000	0	3.18855E-05	0	0	0	0	5.74120E-04	0	0	3.16420E-04	1.52756E-04	2.07019E-03	2.15656E-05	0
4000	5.33208E-05	5.53811E-05	8.26423E-05	3.18614E-05	3.46062E-05	3.65272E-05	1.47634E-03	3.49097E-05	4.88532E-06	3.00460E-04	3.29526E-04	1.46024E-03	5.94479E-05	5.52881E-05
5000	0	5.06295E-05	0	2.09657E-06	0	4.73278E-06	3.15796E-04	0	0	2.55724E-06	0	4.07073E-06	2.82026E-06	0
10000	0	5.02725E-05	0	4.33234E-05	0	1.24372E-05	5.07503E-08	0	0	3.13849E-04	0	1.01557E-06	4.19042E-05	0
$M = 400$														
100	0	7.45429E-07	0	1.08003E-07	8.80460E-05	6.31829E-04	8.33915E-03	0	0	2.13359E-05	0	1.37385E-05	1.46014E-03	3.08440E-05
200	0	1.01475E-07	0	8.87797E-06	0	5.73833E-03	7.74449E-03	0	0	6.42337E-06	2.61235E-05	6.21617E-04	3.73607E-04	4.76268E-07
300	0	4.37162E-05	0	0	0	5.36993E-05	0	0	0	0	0	8.08618E-04	9.86152E-04	0
400	0	1.29624E-03	0	1.09308E-03	0	2.66733E-05	4.08258E-06	0	0	7.64073E-05	0	1.70227E-04	2.55136E-04	4.76633E-07
500	0	5.13750E-05	0	4.34465E-06	0	2.77615E-04	3.59999E-05	0	0	2.27026E-03	0	3.65232E-04	3.83288E-04	0
600	0	4.61691E-05	0	0	0	0	3.20427E-04	0	0	0	0	5.51513E-05	1.58906E-03	0
700	0	8.19535E-05	0	0	0	0	8.12122E-04	0	0	3.29693E-04	0	0	0	0
800	1.24994E-03	1.24998E-03	0	6.30566E-04	2.45823E-03	7.52286E-03	3.30175E-05	4.49499E-03	1.28307E-04	6.18159E-03	7.77397E-03	2.64532E-02	3.89492E-03	8.93570E-04
900	4.17024E-05	7.19074E-05	0	0	0	1.31607E-04	0	1.65860E-06	1.64881E-06	0	8.01157E-04	1.56246E-04	0	0
1000	0	1.34536E-05	0	4.84323E-06	0	1.15471E-05	7.87413E-05	5.36932E-07	2.14505E-07	8.21346E-06	0	1.27814E-04	9.26297E-05	0
1100	2.59035E-05	2.79315E-05	7.65316E-07	7.69717E-06	1.00792E-05	1.63958E-04	4.62507E-05	1.80063E-05	0	1.59331E-04	1.41455E-04	7.03096E-04	1.37554E-04	0
1200	0	0	0	0	0	0	2.19871E-06	0	0	0	0	0	0	0
1300	0	1.29724E-05	0	1.13542E-05	0	3.09164E-05	1.56925E-04	0	1.82411E-06	2.20495E-05	0	9.22740E-05	3.79064E-04	0
1400	0	0	0	0	0	1.38501E-04	5.58243E-04	0	0	1.56315E-04	0	3.51820E-06	0	0
1500	0	2.09907E-05	0	0	0	7.19364E-04	1.19776E-05	0	1.35936E-04	1.22263E-04	5.90207E-04	2.09164E-05	0	0
2000	0	4.13727E-06	8.73579E-07	9.97008E-07	5.81071E-06	7.10885E-05	1.22050E-04	2.72419E-07	0	1.94218E-03	0	4.49886E-05	9.27621E-05	0
3000	0	0	0	0	0	5.24378E-05	0	0	0	3.56397E-05	0	0	0	0
4000	1.20035E-04	1.21493E-04	1.88141E-04	3.12670E-05	5.17704E-05	6.94291E-06	1.12754E-03	1.36414E-05	1.76000E-06	2.09533E-04	2.74553E-04	1.11656E-03	3.63409E-05	0
5000	0	3.26496E-06	0	1.90552E-07	0	3.26261E-06	5.22698E-05	0	2.52510E-07	1.04305E-05	2.56480E-05	1.27053E-04	1.27472E-04	3.86535E-06
10000	0	3.16213E-06	0	2.80268E-06	0	9.98510E-07	4.02506E-06	3.06259E-07	0	2.24589E-05	0	9.06546E-05	2.70250E-06	0

shall use the barycentric SG-Gauss (SGG) quadratures prompted by the barycentric Gegenbauer-Gauss (GG) quadratures, which were derived by Elgindy [29]. These numerical operators are constructed using the stable barycentric representation of Lagrange interpolating polynomials and the explicit barycentric weights for the GG points, and they are well-known for their stability and superior accuracy. The error and the convergence analysis of GG quadratures for sufficiently smooth functions on the interval  $[-1, 1]$  are outlined by [29, Theorems 3.1 & 3.2]. The error of the SGG quadrature for sufficiently smooth functions on the interval  $\Omega_T$  is expounded in [34, Theorem 4.1]. To derive the SG quadratures in barycentric form suited to carry out integrals over any partition of  $\Omega_T$  and study their errors, we closely follow the notations and derivations presented in [27] in the following section.

### 7.1. Barycentric SG Quadratures

Let  $\mathfrak{K}_K = \{1, \dots, K\}$  and consider the partitioning of the time interval  $\Omega_T$  into  $K$  mesh intervals  $\Gamma_{1:K}$  using  $K + 1$  mesh points  $\tau_{0:K}$  distributed along the interval  $\Omega_T$  such that  $\Omega_T = \bigcup_{k=1}^K \Gamma_k$ ,  $\Gamma_k = [\tau_{k-1}, \tau_k]$ ,  $0 = \tau_0 < \tau_1 < \dots < \tau_K = T$ . Let  $\tau_k^+ = (\tau_k + \tau_{k-1})/2$  and  $\tau_k^- = |\Gamma_k|/2$  in respective order, and denote the restricted variable  $t$  whose values are confined to  $\Gamma_k$  by  $t^{(k)}$  such that  $t^{(k)} = t : \tau_{k-1} \leq t \leq \tau_k$ . Define  $\hat{G}_{k,j}^{(\alpha)}(t^{(k)}) = G_j^{(\alpha)}((t^{(k)} - \tau_k^+)/\tau_k^-)$  to be the  $j$ th-degree SG polynomial defined on the partition  $\Gamma_k \forall j \in \mathbb{Z}_0^+, k \in \mathfrak{K}_K$ —henceforth referred to by the  $j$ th-degree,  $k$ th element SG polynomial (or simply the  $(j, k)$ -SG polynomial), where  $G_j^{(\alpha)}(t)$  is the classical  $j$ th-degree Gegenbauer polynomial associated with the real parameter  $\alpha > -1/2$  and standardized by Doha [35]; cf. also Elgindy and Smith-Miles [36, Formula (A.1)]. The  $k$ th element SG polynomials  $\hat{G}_{k,0:N_k}^{(\alpha)}(t^{(k)})$  form a complete  $L_{w_k^{(\alpha)}}^2(\Gamma_k)$ -orthogonal system with respect to the weight function  $w_k^{(\alpha)}(t^{(k)}) = (\tau_k - t^{(k)})^{\alpha-1/2} (t^{(k)} - \tau_{k-1})^{\alpha-1/2} \forall \alpha \in \mathbb{Z}_0^+$ . An important and convenient property of these polynomials is that they are orthogonal with respect to the weighted inner product

$$\left( \hat{G}_{k,m}^{(\alpha)}, \hat{G}_{k,n}^{(\alpha)} \right)_{w_k^{(\alpha)}} = \int_{\tau_{k-1}, \tau_k}^{\tau_k} \hat{G}_{k,m}^{(\alpha)} \hat{G}_{k,n}^{(\alpha)} w_k^{(\alpha)} = \left\| \hat{G}_{k,n}^{(\alpha)} \right\|_{w_k^{(\alpha)}}^2 \delta_{m,n} = \lambda_{k,n}^{(\alpha)} \delta_{m,n}, \quad \forall m, n \in \mathbb{Z}_0^+,$$

where  $\delta_{m,n}$  is the Kronecker delta function,  $\lambda_{k,n}^{(\alpha)} = (\tau_k^-)^{2\alpha} \lambda_n^{(\alpha)}$  is the normalization factor, and  $\lambda_n^{(\alpha)}$  is as defined by [34, Eq. (2.6)]; cf. also [27]. Now,  $\forall k \in \mathfrak{K}_K$ , let  $\mathbb{G}_{N_k}^{(\alpha),k} = \{t_{N_k,l}^{(k),\alpha} \forall l \in \mathbb{J}_{N_k}^+\}$  be the set of the zeroes of the  $(N_k + 1, k)$ -SG



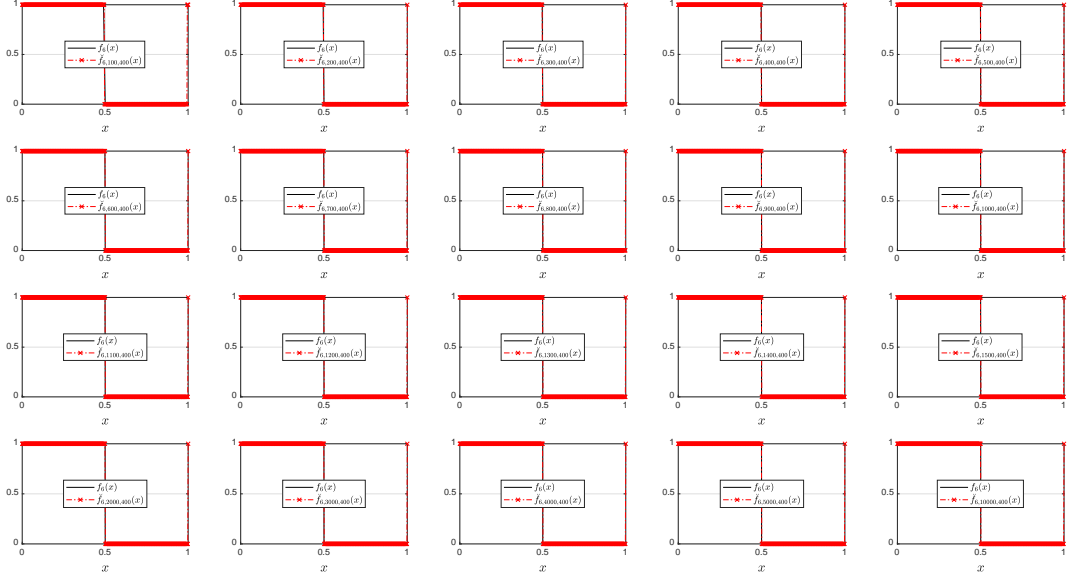


Figure 6: Snapshots of the approximate discontinuous function  $\hat{f}_6$  over one period using  $M = 400$ , for increasing values of  $N$ .

polynomial,  $\hat{G}_{k,N_k+1}^{(\alpha)}(t^{(k)}) \forall_s N_k \in \mathbb{Z}_0^+$ . If we denote by  $\mathbb{P}_n$ , the space of all polynomials of degree at most  $n \in \mathbb{Z}^+$ , then

$$\mathcal{I}_{\tau_k^-, \tau_k^+}^{(t^{(k)})} \phi w_k^{(\alpha)} = (\tau_k^-)^{2\alpha} \mathcal{I}_{-1,1}^{(t)} \phi \{ \tau_k^- t + \tau_k^+ \} w^{(\alpha)} = (\tau_k^-)^{2\alpha} \sum_{j=0}^{N_k} \omega_j^{(\alpha)} \phi(\tau_k^- t_{N_k,j}^{(\alpha)} + \tau_k^+) = \sum_{j=0}^{N_k} \omega_{k,j}^{(\alpha)} \phi(\hat{t}_{N_k,j}^{(k),\alpha}), \quad \forall \phi \in \mathbb{P}_{2N_k+1}, \quad (7.1)$$

using the standard GG quadrature, where  $t_{N_k,0:N_k}^{(\alpha)}$  are the zeroes of the classical  $(N_k + 1)$ th-degree Gegenbauer polynomial  $G_{N_k+1}^{(\alpha)}(t)$ ,  $\omega_{0:n_k}^{(\alpha)}$  are the corresponding Christoffel numbers as given by [37, Eq. (2.6)], and  $\omega_{k,0:N_k}^{(\alpha)}$  are the Christoffel numbers corresponding to the SGG set  $\mathbb{G}_{N_k}^{(\alpha),k}$  and defined by

$$\omega_{k,l}^{(\alpha)} = (\tau_k^-)^{2\alpha} \omega_l^{(\alpha)} = \frac{1}{\sum_{j=0}^{N_k} (\lambda_{k,l}^{(\alpha)})^{-1} (\hat{G}_{k,j}^{(\alpha)}(\hat{t}_{N_k,l}^{(k),\alpha}))^2}, \quad \forall l \in \mathbb{J}_{N_k}^+.$$

The SG Quadrature Rule (7.1) allows us to define the discrete inner product  $(\cdot, \cdot)_{k,N_k}$  associated with the SGG interpolation points as follows:

$$(u, v)_{k,N_k} = \sum_{j=0}^{N_k} \omega_{k,j}^{(\alpha)} u(\hat{t}_{N_k,j}^{(k),\alpha}) v(\hat{t}_{N_k,j}^{(k),\alpha}), \quad \forall u, v \in \text{Def}(\mathbf{\Gamma}_k).$$

With this mathematical setting, we can write the SGG interpolant of a restricted, real function  $f$  on  $\mathbf{\Gamma}_k$  obtained through interpolation at the set  $\mathbb{G}_{N_k}^{(\alpha),k}$  as

$$P_{N_k} f(t^{(k)}) = \sum_{j=0}^{N_k} a_j^{(k)} \hat{G}_{k,j}^{(\alpha)}(t^{(k)}), \quad (7.2)$$



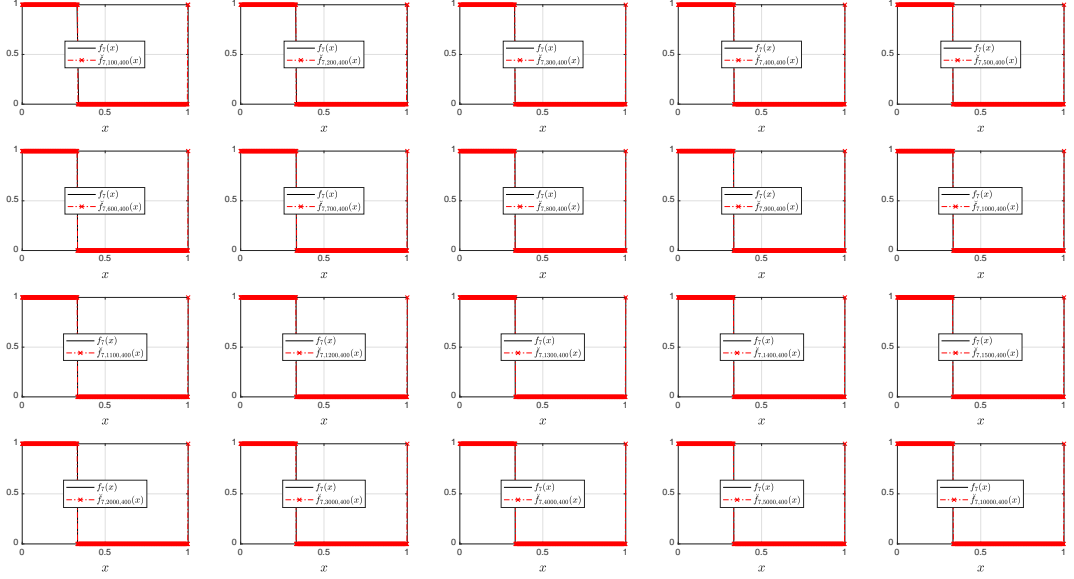


Figure 7: Snapshots of the approximate discontinuous function  $\check{f}_j$  over one period using  $M = 400$ , for increasing values of  $N$ .

where  $a_{0:N_k}^{(k)}$  are the associated discrete interpolation coefficients,  $\forall k \in \mathfrak{K}$ , defined by

$$a_j^{(k)} = \frac{(P_{N_k} f, \hat{G}_{k,j}^{(\alpha)})_{k,N_k}}{\|\hat{G}_{k,j}^{(\alpha)}\|_{W_k^{(\alpha)}}^2} = \frac{(f, \hat{G}_{k,j}^{(\alpha)})_{k,N_k}}{\|\hat{G}_{k,j}^{(\alpha)}\|_{W_k^{(\alpha)}}^2} = \frac{1}{\lambda_{k,j}^{(\alpha)}} \sum_{l=0}^{N_k} \varpi_{k,l}^{(\alpha)} f(\hat{t}_{N_k,l}^{(k),\alpha}) \hat{G}_{k,j}^{(\alpha)}(\hat{t}_{N_k,l}^{(k),\alpha}), \quad \forall j \in \mathbb{J}_{N_k}^+. \quad (7.3)$$

Equation (7.3) gives the discrete SG transform on  $\Gamma_k$ . Substituting Eq. (7.3) into Eq. (7.2) yields the SGG interpolant of  $f$  in the following Lagrange form

$$P_{N_k} f(t^{(k)}) = \sum_{l=0}^{N_k} f(\hat{t}_{N_k,l}^{(k),\alpha}) \mathcal{L}_{k,l}^{(\alpha)}(t^{(k)}), \quad (7.4)$$

where  $\mathcal{L}_{k,0:N_k}^{(\alpha)}(t^{(k)})$  are the shifted Lagrange interpolating polynomials in basis-form defined on  $\Gamma_k$  by

$$\mathcal{L}_{k,l}^{(\alpha)}(t^{(k)}) = \varpi_{k,l}^{(\alpha)} \sum_{j=0}^{n} (\lambda_{k,j}^{(\alpha)})^{-1} \hat{G}_{k,j}^{(\alpha)}(\hat{t}_{N_k,l}^{(k),\alpha}) \hat{G}_{k,j}^{(\alpha)}(t^{(k)}), \quad \forall l \in \mathbb{J}_{N_k}^+.$$

A faster and more numerically stable way to evaluate  $P_{N_k} f(t^{(k)})$  can be achieved by calculating Lagrange polynomials through the “true” barycentric formula

$$\mathcal{L}_{k,l}^{(\alpha)}(t^{(k)}) = \frac{\xi_{k,l}^{(\alpha)}}{t^{(k)} - \hat{t}_{N_k,l}^{(k),\alpha}} / \sum_{j=0}^{N_k} \frac{\xi_{k,j}^{(\alpha)}}{t^{(k)} - \hat{t}_{N_k,j}^{(k),\alpha}}, \quad \forall l \in \mathbb{J}_{N_k}^+, \quad (7.5)$$

which brings into play the barycentric weights  $\xi_{k,0:N_k}^{(\alpha)}$  that depend on the interpolation points. An interpolation in Lagrange form with Lagrange polynomials defined by Formula (7.5) is often referred to by “a barycentric rational interpolation.” The barycentric weights associated with the SGG points in  $\Gamma_1$  can be expressed explicitly in terms of

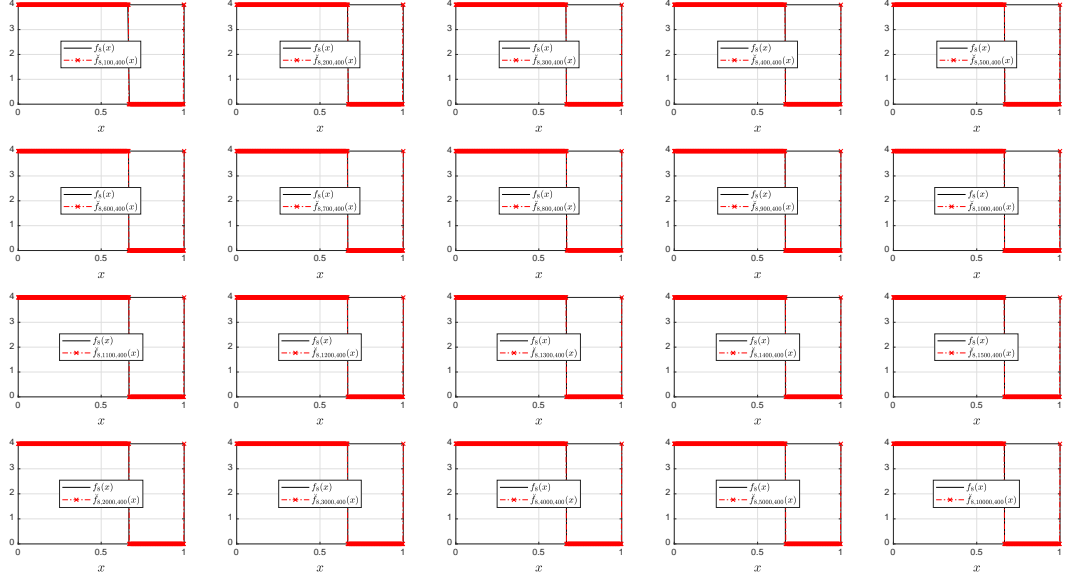


Figure 8: Snapshots of the approximate discontinuous function  $\check{f}_8$  over one period using  $M = 400$ , for increasing values of  $N$ .

the corresponding Christoffel numbers in algebraic form by

$$\xi_{1,l}^{(\alpha)} = \left(\frac{2}{\tau_1}\right)^{\alpha+1} (-1)^l \sqrt{(\tau_1 - \hat{t}_{N_1,l}^{(1),\alpha}) \hat{t}_{N_1,l}^{(1),\alpha} \varpi_{1,l}^{(\alpha)}}, \quad \forall l \in \mathbb{J}_{N_1}^+,$$

or in trigonometric form through

$$\xi_{1,l}^{(\alpha)} = \left(\frac{2}{\tau_1}\right)^{\alpha} (-1)^l \sin\left(\cos^{-1}\left(\frac{2\hat{t}_{N_1,l}^{(1),\alpha}}{\tau_1} - 1\right)\right) \sqrt{\varpi_{1,l}^{(\alpha)}}, \quad \forall l \in \mathbb{J}_{N_1}^+,$$

cf. [38, Eqs. (21) and (22)]. Through the change of variables  $x = (t^{(k)} - \tau_k^+)/\tau_k^-$  it is easy to show that the barycentric weights associated with the SSG in any partition  $\Gamma_k$  can be defined in algebraic form by

$$\xi_{k,l}^{(\alpha)} = (\tau_k^-)^{-(\alpha+1)} (-1)^l \sqrt{(\tau_k - \hat{t}_{N_k,l}^{(k),\alpha}) (\hat{t}_{N_k,l}^{(k),\alpha} - \tau_{k-1}) \varpi_{k,l}^{(\alpha)}}, \quad \forall l \in \mathbb{J}_{N_k}^+, \quad (7.6)$$

or in trigonometric form through

$$\xi_{k,l}^{(\alpha)} = (\tau_k^-)^{-\alpha} (-1)^l \sin\left(\cos^{-1}\left(\frac{\hat{t}_{N_k,l}^{(k),\alpha} - \tau_k^+}{\tau_k^-}\right)\right) \sqrt{\varpi_{k,l}^{(\alpha)}}, \quad \forall l \in \mathbb{J}_{N_k}^+. \quad (7.7)$$

Formula (7.7) avoids the cancellation error in calculating Formula (7.6) using floating point arithmetic due to the clustering of the SGG points near the endpoints of each partition as the mesh size increase. The successive integrations of the SGG interpolant (7.4) on the intervals  $[\tau_{k-1}, \hat{t}_{N_k,i}^{(k),\alpha}] \forall i \in \mathbb{J}_{N_k}^+$ , give rise to the first-order,  $k$ th element, square SG integration matrix (SGIM) in barycentric form,  ${}_k\mathbf{P} = ({}_kP_{i,j})_{0 \leq i,j \leq N_k}$ , whose elements are defined by

$${}_kP_{i,j} = \varpi_{k,j}^{(\alpha)} \sum_{l=0}^n (\lambda_{k,l}^{(\alpha)})^{-1} \hat{G}_{k,l}^{(\alpha)}(\hat{t}_{N_k,j}^{(k),\alpha}) \mathcal{I}_{\tau_{k-1}, \hat{t}_{N_k,i}^{(k),\alpha}}^{(t^{(k)})} \hat{G}_{k,l}^{(\alpha)}, \quad i, j \in \mathbb{J}_{N_k}^+, \quad k \in \mathfrak{R}_K, \quad (7.8)$$

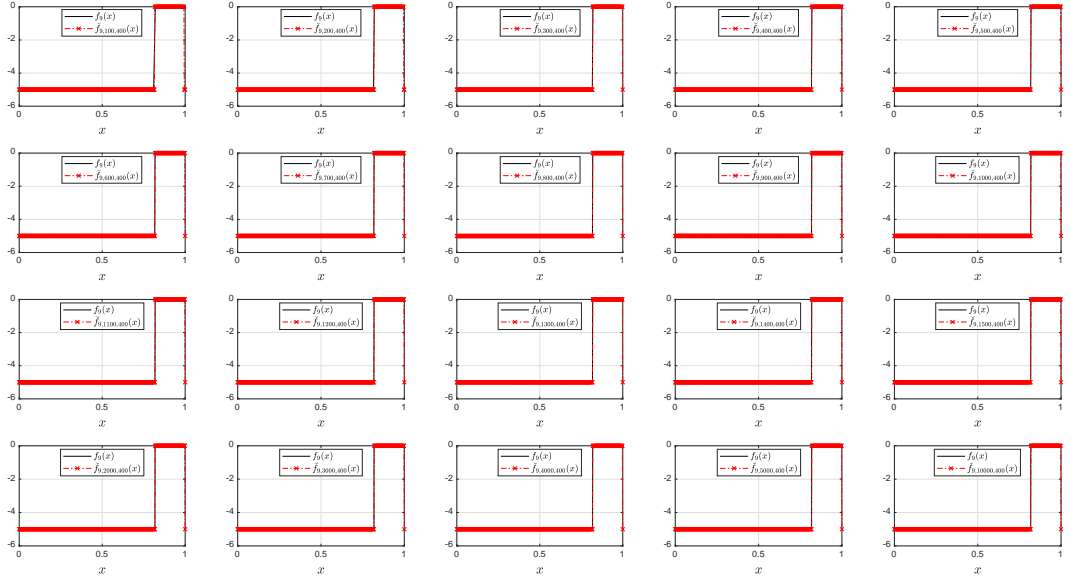


Figure 9: Snapshots of the approximate discontinuous function  $\check{f}_0$  over one period using  $M = 400$ , for increasing values of  $N$ .

in basis-form, or

$${}_k P_{i,j} = \mathcal{I}_{\tau_{k-1}, \hat{t}_{N_k, j}^{(k), \alpha}}^{(f^{(k)})} \mathcal{L}_{k,j}^{(\alpha)}, \quad i, j \in \mathbb{J}_{N_k}^+, \quad k \in \mathfrak{R}_K, \quad (7.9)$$

in rational-form, where  $\mathcal{L}_{k,j}^{(\alpha)}$  is as defined by Eq. (7.5). When the computations of  $\mathcal{I}_{y_{M_k, i}}^{(f^{(k)})} (P_{N_k} f)$  are needed,  $\forall_s M_k$ -random set of points  $\{y_{M_k, 0:M_k}\} \subset (\tau_{k-1}, \tau_k] : y_{M_k, i} \notin \mathbb{G}_{N_k}^{(\alpha), k} \forall M_k \in \mathbb{Z}^+, i \in \mathbb{J}_{M_k}^+$ , one can derive the elements formulas of the associated rectangular SGIM,  ${}_k \hat{P}_{i,j} = ({}_k \hat{P}_{i,j})$ ,  $i \in \mathbb{J}_{M_k}^+, j \in \mathbb{J}_{N_k}^+$ , by performing the replacement  $\hat{t}_{N_k, i}^{(k), \alpha} \leftarrow y_{M_k, i}$  in Formulas (7.8) and (7.9). If an element  $y_{M_k, i} = \tau_k \forall_a k \in \mathfrak{R}_K$ , we shall conveniently denote it by  $\hat{t}_{N_k, N_k+1}^{(k), \alpha}$ , and replace its associated matrix elements  ${}_k \hat{P}_{i,j}$  by  ${}_k P_{N_k+1, j}$  in this particular case such that  ${}_k P_{N_k+1} = {}_k P_{N_k+1, 0:N_k}$ . For a comprehensive review on Gegenbauer polynomials and quadratures and their relevant theory, the reader may consult Refs. [29, 34, 35, 37, 39, 40], and the Refs. therein. For additional resources on why we prefer to use Gegenbauer polynomials and their shifted variants in numerical discretizations, the reader may consult [24, 41] and the Refs. therein.

### 7.1.1. Error and Convergence Analyses of Barycentric SG Quadratures

Let  $\|g\|_{\infty, \Gamma_k} = \|g\|_{\infty} = \sup |g(t^{(k)})| \forall_a g \in \mathfrak{F} \cap \text{Def}(\Gamma_k), k \in \mathfrak{R}_K$ . The following two theorems underline the SG quadrature truncation error and its bounds on any partition  $\Gamma_k$ . Their proofs can be immediately derived from [27, Proofs of Theorems 4.1 and 4.2] by replacing the notations  $m_k, \alpha_i^{(k),*}, \hat{z}_{m_k, i, j}^{(k), \alpha}$  with  $N_k, \alpha, \hat{t}_{N_k, j}^{(k), \alpha}$ , respectively.

**Theorem 7.1.** *Let  $N_k, M_k \in \mathbb{Z}_0^+$ , and consider any arbitrary integration nodes set  $\{y_{M_k, 0:M_k}\} \subset \Gamma_k \forall k \in \mathfrak{R}_K$ . Suppose also that  ${}_k g \in C^{N_k+1}(\Gamma_k)$  is approximated by Formula (7.2) with the associated discrete interpolation coefficients given by Formula (7.3),  $\forall_s g \in \mathfrak{F}$ . Then  $\exists \{\zeta_{M_k, 0:M_k}\} \subset \text{int}(\Gamma_k)$  such that*

$$\mathcal{I}_{\tau_{k-1}, y_{M_k, i}}^{(f^{(k)})} g = {}_k \mathbf{P}_i g_{0:N_k} + E_{N_k}^{(\alpha)}(y_{M_k, i}, \zeta_{M_k, i}),$$

where  $g_{0:N_k}^t = g(\hat{t}_{N_k, 0:N_k}^{(k), \alpha})$ ,

$$E_{N_k}^{(\alpha)}(y_{M_k, i}, \zeta_{M_k, i}) = \frac{g^{(N_k+1)}(\zeta_{M_k, i})}{(N_k+1)! K_{k, N_k+1}^{(\alpha)}} \mathcal{I}_{\tau_{k-1}, y_{M_k, i}}^{(f^{(k)})} \hat{G}_{k, N_k+1}^{(\alpha)},$$

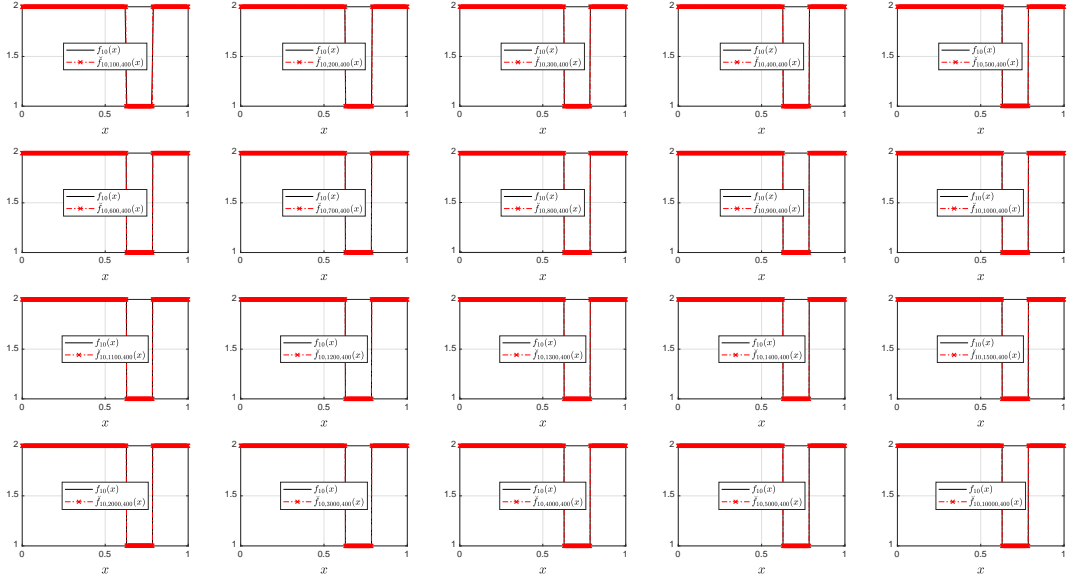


Figure 10: Snapshots of the approximate discontinuous function  $\check{f}_{10}$  over one period using  $M = 400$ , for increasing values of  $N$ .

is the truncation error of the SG quadrature  $\forall_e i, k$ ,

$$K_{k,j}^{(\alpha)} = \frac{2^{2j-1} \Gamma(2\alpha + 1) \Gamma(j + \alpha)}{|\Gamma_k|^j \Gamma(\alpha + 1) \Gamma(j + 2\alpha)} \quad \forall j \in \mathbb{Z}_0^+,$$

is the leading coefficient of the  $(j, k)$ -SG polynomial, and  $\Gamma$  is the usual Gamma function.

**Theorem 7.2.** Let  $\|k\mathcal{G}^{(N_k+1)}\|_\infty = A_k \in \mathbb{R}_0^+ \forall k \in \mathfrak{R}_K$ , where the constant  $A_k$  depends on  $k$  but is independent of  $N_k$ . Suppose also that the assumptions of Theorem 7.1 hold true. Then there exist some constants  $D^{(\alpha)} > 0$ ,  $B_{1,k}^{(\alpha)} = A_k D^{(\alpha)}$ , and  $B_2^{(\alpha)} > 1$ , which depend on  $\alpha$  but are independent of  $N_k$ , such that the SG quadrature truncation error,  $E_{N_k}^{(\alpha)}(y_{M_k,i}, \zeta_{M_k,i})$ , is bounded by

$$\left\| E_{N_k}^{(\alpha)}(y_{M_k,i}, \zeta_{M_k,i}) \right\|_{\infty, \Gamma_k} = B_{1,k}^{(\alpha)} 2^{-2N_k-1} e^{N_k} N_k^{\alpha-N_k-\frac{3}{2}} (y_{M_k,i} - \tau_{k-1}) |\Gamma_k|^{N_k+1} \times \left( \begin{array}{l} 1, \quad N_k \geq 0 \wedge \alpha \geq 0, \\ \frac{\Gamma(\frac{N_k}{2} + 1) \Gamma(\alpha + \frac{1}{2})}{\sqrt{\pi} \Gamma(\frac{N_k}{2} + \alpha + 1)}, \quad N_k \in \mathbb{Z}_0^+ \wedge -\frac{1}{2} < \alpha < 0, \\ \frac{2\Gamma(\frac{N_k+3}{2}) \Gamma(\alpha + \frac{1}{2})}{\sqrt{\pi} \sqrt{(N_k+1)(N_k+2\alpha+1)} \Gamma(\frac{N_k+1}{2} + \alpha)}, \quad N_k \in \mathbb{Z}_{0,e}^+ \wedge -\frac{1}{2} < \alpha < 0, \\ B_2^{(\alpha)} (N_k+1)^{-\alpha}, \quad N_k \rightarrow \infty \wedge -\frac{1}{2} < \alpha < 0 \end{array} \right), \quad \forall i \in \mathbb{J}_{M_k}^+, k \in \mathfrak{R}_K.$$

Theorem 7.2 shows that the SG quadrature formula converges exponentially fast for piecewise-smooth functions whose pieces are defined on  $\Gamma_{1:K}$ . Since  $\psi$  is a piecewise-smooth function on  $\Omega_T$ , the truncation errors in approximating its definite integrals over the intervals  $\Omega_{x_{N,0}:x_{N-1}}$  using SG quadratures decay with exponential convergence rate and the total quadrature error is dominated by the errors committed in constructing  $\check{u}_{N,M}$  and  $\check{s} \forall_e N \in \mathbb{J}_N$ . On the other hand, regardless of how well the estimates of  $\check{u}_{N,M}$  and  $\check{s}$ , the FPSQ error in approximating  $\mathcal{I}_{x_{N,0}}^{(i)} \psi \forall_e n \in \mathbb{J}_N$ , in the best scenario, is of  $O(N^{-1/2})$ , as  $N \rightarrow \infty$ , not to mention the size gap between the SGIM employed in the construction of the SG quadrature and the FIM required to achieve the same degree of accuracy—clearly, the SGIM wins this race

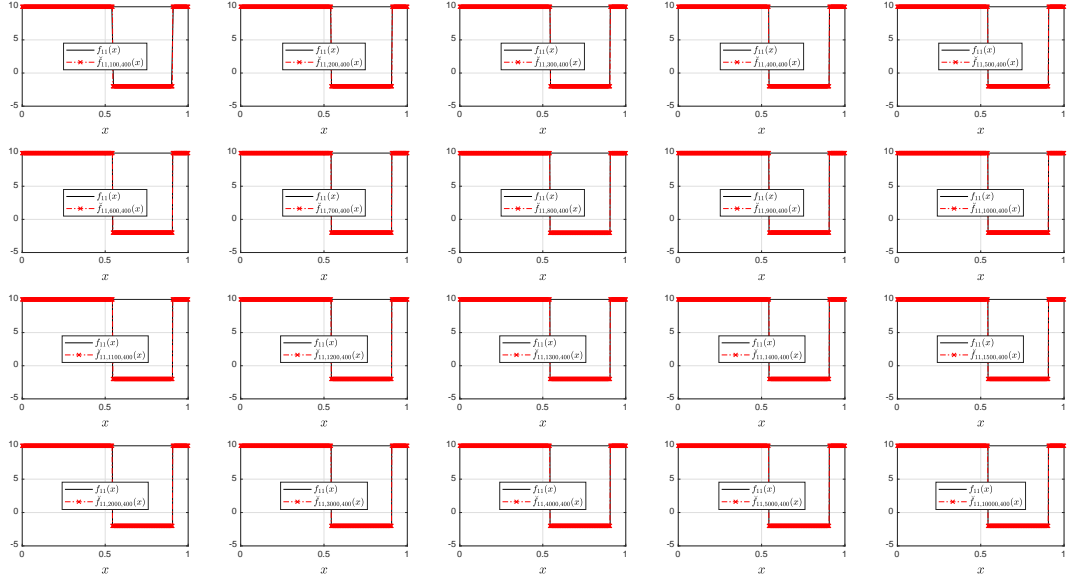


Figure 11: Snapshots of the approximate discontinuous function  $\check{f}_{11}$  over one period using  $M = 400$ , for increasing values of  $N$ .

hands down.

### 7.1.2. Efficient and Stable Computation of SG Matrices

It is noteworthy to mention that  ${}_k\mathbf{P}$  and  ${}_k\hat{\mathbf{P}}$  are directly related to the usual first-order Gegenbauer integration matrices (GIMs) in barycentric form  $\mathbf{P}$  and  $\hat{\mathbf{P}}$  derived by Elgindy [29] by the useful identity

$$[{}_k\mathbf{P}, {}_k\hat{\mathbf{P}}] = (\tau_k^-) [\mathbf{P}, \hat{\mathbf{P}}], \quad \forall k, \quad (7.10)$$

cf. Elgindy [29, Algorithms 1 and 8] for how to efficiently construct the pair of matrices  $\mathbf{P}$  and  $\hat{\mathbf{P}}$ . Formula (7.10) allows us to calculate definite integrals over any partition  $\Gamma_k$  in the physical space by premultiplying either  $\mathbf{P}$  or  $\hat{\mathbf{P}}$  by the constant factor  $\tau_k^-$ ; thus, reducing the overall amount of computations required significantly.

To evaluate the necessary definite integrals of  $\psi$  over the intervals  $\Omega_{x_N,0;N-1}$ , one still needs to evaluate  $\mathcal{I}_{\tau_{k-1},\tau_k}^{(k)} \psi \forall_e k \in \mathfrak{R}_K \setminus \{K\}$ , assuming that  $x_{N,N-1} \in \Gamma_k$ . For instance, to piecewise integrate  $\psi$  on the intervals  $\Omega_{x_N,p;n} \forall_s p, n \in \mathbb{J}_N : \{x_{N,p;n}\} \subset \Gamma_2$ , one needs first to calculate  $\mathcal{I}_{\Gamma_1}^{(k)} \psi$  using the row vector  ${}_1\mathbf{P}_{N_k+1}$  before using  ${}_2\mathbf{P}$  to estimate the required integrals on  $[\tau_1, x_{N,i}]_{i=p;n}$ . One can similarly calculate  ${}_k\mathbf{P}_{N_k+1} \forall k \in \mathfrak{R}_K$  using the useful formula

$${}_k\mathbf{P}_{N_k+1} = (\tau_k^-) \mathbf{P}_{N_k+1},$$

where  $\mathbf{P}_{N_k+1}$  is a row vector whose elements form the  $(N_k+1)$ st-row of the barycentric GIM constructed using Elgindy [29, Algorithm 6 or 7].

Figure 16 shows the SG quadrature error infinity- and -Euclidean norms in log-lin scale of the definite integrals of the square wave function  $f_6$  when successively integrated over the intervals  $\Omega_{x_N,0;N-1}$ , using merely two GG points and the Gegenbauer parameter (index) value  $\alpha = -0.1$ . Notice here that the obtained integral approximations are accurate to almost full precision in double-precision floating-point arithmetic, since  $f_6$  is a linear piecewise function and the 2-point SG quadrature is exact for polynomials of degree at most three. For piecewise-constant functions, the SG quadrature truncation error collapses for  $N_k \geq 0$ , as indicated by Theorem 7.1, and the computational error is dominated by the maximum error in the approximate jump discontinuity points and the extreme values of the discontinuous function. This outcome is consistent with Figure 17, which shows the plots of the 2-point SG quadrature error infinity- and -Euclidean norms in log-lin scale of the reconstructed square wave function  $\check{f}_{6,N,400}$  when successively integrated over the intervals  $\Omega_{x_N,0;N-1}$ , for  $\alpha = -0.1$  and several increasing values of  $N$ . Clearly, the quadrature error

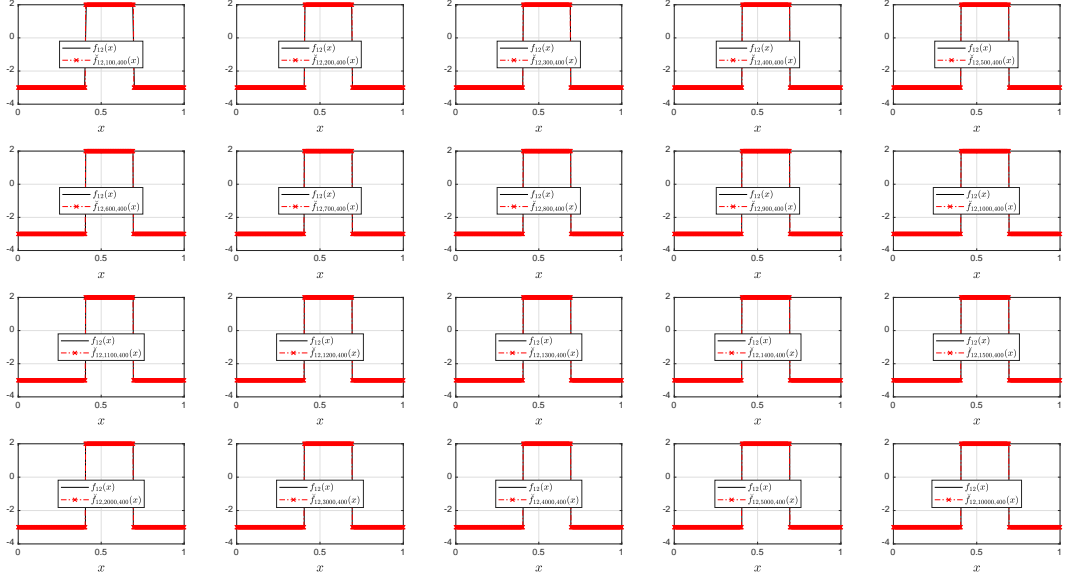


Figure 12: Snapshots of the approximate discontinuous function  $\check{f}_{12}$  over one period using  $M = 400$ , for increasing values of  $N$ .

infinity-norm is of the same maximum error order of the approximate jump discontinuity points and extreme values recorded in Tables 2 and 3, whenever an approximation error exists. In the absence of any approximation errors, the quadrature error infinity-norm approaches the machine epsilon. The figure also shows the corresponding FPSQ error infinity-norms using FPSI matrices of the same size of the mesh grid, as recorded in Table 4, where we observe the slow decay of the errors as the mesh grid size grows larger, no matter how well the reconstructed square wave function was set up.

To support our analysis further, consider the problem of evaluating  $\mathcal{I}_{\Omega_{N,0;N-1}}^{(t)} \psi$  when

$$s(t) = \begin{cases} \frac{2}{3}(t+1), & 0 \leq t < \xi_1, \\ -\frac{1}{10}(t-\xi_1)^2 + \frac{2}{3}(\xi_1+1), & \xi_1 \leq t < \xi_2, \\ \sin\left(\frac{1}{4}(t-\xi_2)\right) - \frac{1}{10}(\xi_2-\xi_1)^2 + \frac{2}{3}(\xi_1+1), & \xi_2 \leq t < T, \end{cases} \quad \text{and} \quad u(t) = \begin{cases} 0, & 0 \leq t < \xi_1, \\ 2, & \xi_1 \leq t < \xi_2, \\ 0, & \xi_2 \leq t < T. \end{cases}$$

Here we can calculate the exact required integrals of  $\psi$ , since both  $s$  and  $u$  are available in closed form and their antiderivatives can be written in terms of elementary functions. The plots of  $s, u, \psi$  and the errors plot of approximating the required integrals using the SG quadratures are shown in Figure 13 for some parameter values. The maximum absolute error recorded was about  $2.66\text{E-}15$ , which demonstrates the high accuracy of the SG quadratures for exact input data and their exponential convergence using relatively small number of quadrature nodes. To test the stability of SG quadratures, let us perturb the jump discontinuity points such that  $\xi_{1:2} = \check{\xi}_{1:2} + \delta_{1:2} \forall_s \delta_{1:2} \in \mathbb{R}_{\neq 0}^2$ , and denote the perturbed state- control, and state derivative-variables by  $\check{s}, \check{u}$ , and  $\check{\psi}$ , respectively. Figure 14 shows the exact and perturbed functions for  $\delta_{1:2} = [-1\text{E-}5, 1\text{E-}6]$  in addition to the errors plot generated using the same parameter values. The maximum absolute error recorded was about  $1.08\text{E-}05$ , which verifies the numerical stability of the numerical scheme as the quadrature errors are nearly equal to the maximum perturbations incorporated in the mathematical model. It is interesting to mention here that better estimates were obtained when we evaluated the definite integrals of  $\psi$  over partitions determined by the SGG points instead of the equispaced nodes. In particular, the maximum absolute error in evaluating  $\mathcal{I}_{\Omega_{N_k,0;N_k}}^{(t)} \psi \forall k \in \mathfrak{R}_3$  using the SG quadratures and the same parameter values was about  $2.22\text{E-}15$  assuming that  $\tau_1 = \xi_1, \tau_2 = \xi_2$ , and  $K = 3$ ; cf. Figure 15.



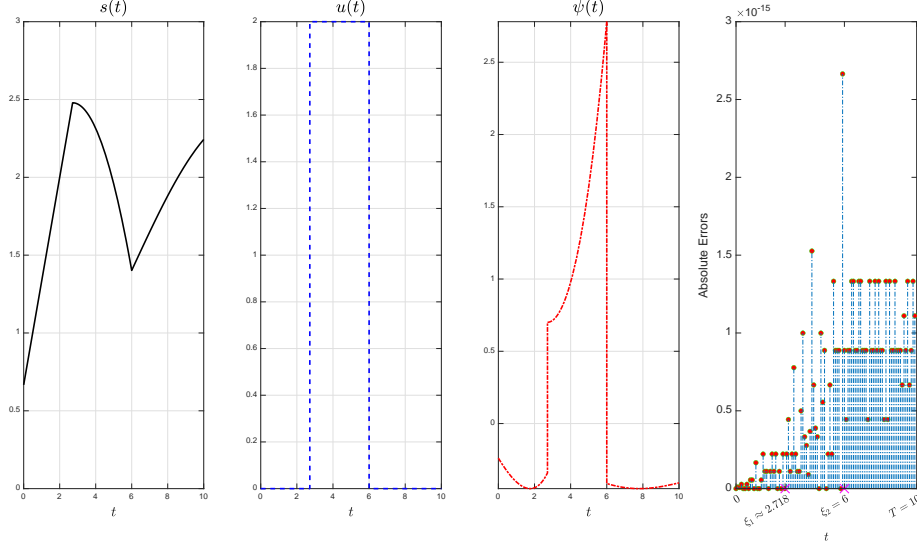


Figure 13: The plots of  $s, u, \psi$  and the errors plot of approximating  $\mathcal{I}_{\Omega_{\xi_{1,2}, 0.99}}^{(t)} \psi$  using the SG quadratures for the parameter values  $T = 10, s_{\text{in}} = 3, \mu_{\text{max}} = 1, k_s = 2.5, \alpha = 1/2, \xi_{1,2} = [e, 6]$ , and  $N_{1,3} = [18]_3$ .

## 8. The FG-PC Method

We initiate our proposed method of solution by collocating Problem  $\mathcal{IP}$  in the Fourier physical space at the set of mesh points  $\mathbb{S}_N$  with the aid of Formulas (4.8a) and (4.9) to obtain the discrete optimal control problem

$$\begin{aligned} \min \quad & J_N = \frac{1}{N} \left( \mathbf{I}_N^t [\bar{s}; s_{1:N-1}] \right) \\ \text{s.t.} \quad & s_{1:N-1} = \bar{s} \mathbf{I}_{N-1} + \Theta_{\Phi} \psi_{0:N-1}, \\ & \mathbf{I}_N^t u_{0:N-1} = N \bar{u}, \\ & \mathbf{0}_{N-1} \leq s_{1:N-1} \leq s_{\text{in}} \mathbf{I}_{N-1}, \\ & u_{\min} \mathbf{I}_N \leq u_{0:N-1} \leq u_{\max} \mathbf{I}_N. \end{aligned}$$

Let  $\mathbf{X} = [s_{1:N-1}; u_{0:N-1}]$ ,  $\bar{\mathbf{X}} = [\bar{s}; \mathbf{X}_{1:N-1}]$ ,  $\mathbf{A} = [\mathbf{0}_{N-1}^t; \mathbf{I}_N^t]$ ,  $\mathbf{X}_{lb} = [\mathbf{0}_{N-1}; u_{\min} \mathbf{I}_N]$ ,  $\mathbf{X}_{ub} = [s_{\text{in}} \mathbf{I}_{N-1}; u_{\max} \mathbf{I}_N]$ , and  $\hat{\mathbf{X}} = s_{\text{in}} \mathbf{I}_N - \bar{\mathbf{X}}$ . Then

$$\psi_{0:N-1} = \left[ \mathbf{X}_{N:2N-1} - \mu_{\max} \bar{\mathbf{X}} \odot (k_s \hat{\mathbf{X}} + \bar{\mathbf{X}}) \right] \odot \hat{\mathbf{X}},$$

and the following scaled optimization problem

$$\begin{aligned} \min \quad & \bar{J}_N = \mathbf{I}_N^t \bar{\mathbf{X}} \\ \text{s.t.} \quad & \mathbf{X}_{1:N-1} = \bar{s} \mathbf{I}_{N-1} + \Theta_{\Phi} \psi_{0:N-1}, \\ & \mathbf{A} \mathbf{X} = N \bar{u}, \\ & \mathbf{X}_{lb} \leq \mathbf{X} \leq \mathbf{X}_{ub}. \end{aligned} \tag{8.1}$$

is equivalent to the foregoing constrained nonlinear programming problem in the sense that an optimal solution  $\mathbf{X}^* = [s_{1:N-1}^*; u_{0:N-1}^*]$  to the latter problem is also an optimal solution to the former problem; moreover, the optimal objective function value  $J_N^* = \bar{J}_N^*/N$ . We denote the predicted optimal state- and control-variables obtained at this stage by  $s^p(t)$  and  $u^p(t)$ , respectively; their associated predicted optimal objective function value is denoted by  $J_N^p$ . Moreover, we denote  $s_{1:N-1}^p$  and  $u_{0:N-1}^p$  by  $s_N^p$  and  $u_N^p$ , and refer to them together with  $\mathbf{X}^p = [s_N^p; u_N^p]$  by the predicted state- control, and solution-vectors, in respective order.

To improve the obtained approximations we construct the  $T$ -periodic Fourier interpolants  $I_N s^p$  and  $I_N u^p$  from  $s_N^p$

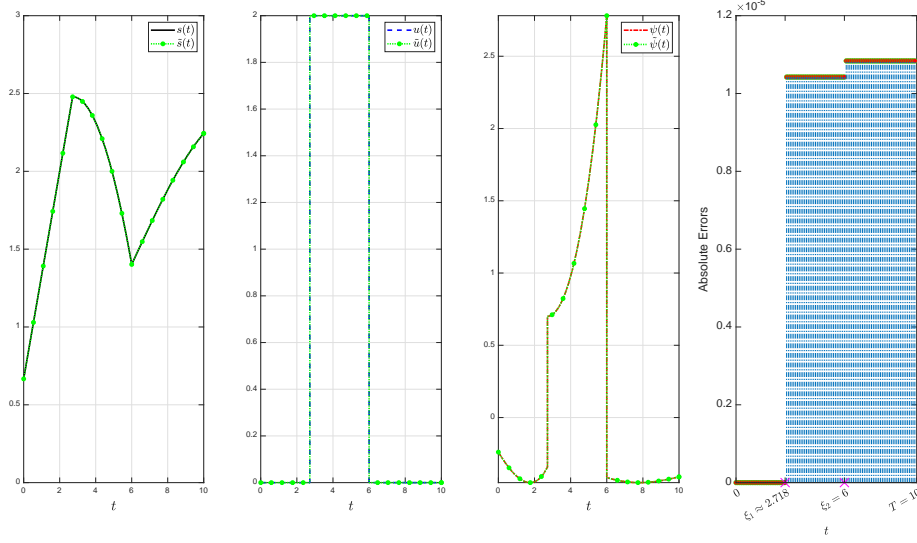


Figure 14: The plots of  $s, u, \psi$  and their perturbations (in green color) in addition to the errors plot of approximating  $\mathcal{I}_{\Omega_{100,0.99}}^{(t)} \tilde{\psi}$  using the SG quadratures for the parameter values  $T = 10, s_{\text{in}} = 3, \mu_{\text{max}} = 1, k_s = 2.5, \alpha = 1/2, \xi_{1:2} = [e, 6], \delta_{1:2} = [-1\text{E-}5, 1\text{E-}6],$  and  $N_{1:3} = [18]_3$ .

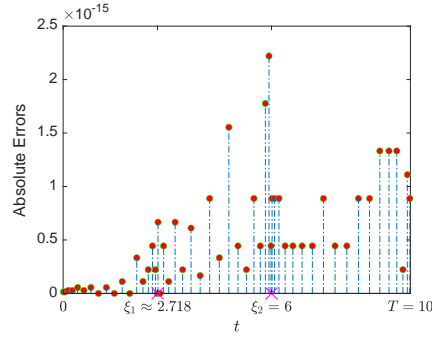


Figure 15: The error plot of approximating  $\mathcal{I}_{\Omega_{N_k, 0.99}^{(k), \alpha}}^{(t)} \psi$  using the SG quadratures for the parameter values  $T = 10, s_{\text{in}} = 3, \mu_{\text{max}} = 1, k_s = 2.5, \alpha = 1/2, \xi_{1:2} = [e, 6],$  and  $N_{1:3} = [18]_3$ .

and  $\mathbf{u}_N^p$  through Formula (4.4) as follows:

$$\begin{aligned} I_N s^p(t) &= \mathcal{F}(t) \bar{s}_N^p, \\ I_N u^p(t) &= \mathcal{F}(t) \mathbf{u}_N^p, \end{aligned} \quad (8.2a)$$

where  $\bar{s}_N^p = [\bar{s}; s_N^p]$  and  $\mathcal{F} = [\mathcal{F}_0, \dots, \mathcal{F}_{N-1}]$ . We then estimate the jump discontinuity points  $\tilde{\xi}_{1:2}$  of the predicted controller and reconstruct the approximate discontinuous controller  $\check{u}_{N,M}$  from the PS data using Algorithm A.2. Since the controller is a bang–bang controller, then  $u \in \{u_{\text{min}}, u_{\text{max}}\}$ , and the approximation  $\check{u}_{N,M}$  can be further corrected by the following formula:

$$u_{N,M}^c(t) = \begin{cases} u_{\text{max}}, & 0 \leq t < \tilde{\xi}_1 \vee \tilde{\xi}_2 \leq t \leq T, \\ u_{\text{min}}, & \tilde{\xi}_1 \leq t < \tilde{\xi}_2, \end{cases} \quad (8.3a)$$

if  $|\check{u}_{N,M}(\tilde{\xi}_1) - u_{\text{min}}| < |u_{\text{max}} - \check{u}_{N,M}(\tilde{\xi}_1)|$ , or by

$$u_{N,M}^c(t) = \begin{cases} u_{\text{min}}, & 0 \leq t < \tilde{\xi}_1 \vee \tilde{\xi}_2 \leq t \leq T, \\ u_{\text{max}}, & \tilde{\xi}_1 \leq t < \tilde{\xi}_2, \end{cases} \quad (8.3b)$$

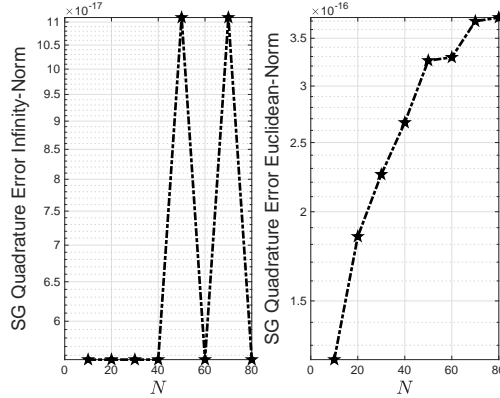


Figure 16: The figure shows the error infinity- and -Euclidean norms of the 2-point SG quadrature with  $\alpha = -0.1$  in log-lin scale of the square wave function  $f_6$  when successively integrated over the intervals  $\Omega_{x_{N,0:N-1}}$ , for  $N = 10, 20, 40,$  and  $80$ .

otherwise. Formulas (8.3a) and (8.3b) provide accurate approximations to the exact controller for relatively large values of  $N$  and  $M$  due to the close proximity of  $\tilde{\xi}_{1:2}$  from the true jump discontinuity points  $\xi_{1:2}$  as demonstrated earlier in Section 6. Now, let  $\tau_1 = \tilde{\xi}_1$ ,  $\tau_2 = \tilde{\xi}_2$ , and  $K = 3$ . To obtain the corresponding corrected values of the state variable we can solve the nonlinear equality constraints

$$s_{1:N-1} = \bar{s} \mathbf{I}_{N-1} + \mathcal{I}_{\Omega_{x_{N,1:N-1}}}^{(t)} \psi, \quad (8.4)$$

for  $s_{1:N-1}$  starting from some initial approximations. However, to approximate  $\mathcal{I}_{\Omega_{x_{N,1:N-1}}}^{(t)} \psi$  using the highly accurate SG quadratures, the grid point values of  $\psi$  at the SGG points in each partition  $\Gamma_k$  are required  $\forall k \in \mathfrak{R}_3$  as illustrated earlier in Section 7.1. While the corrected control values at the SGG points in each partition,  $u_{N_k}^c = u_{0:N_k}^{c,k} := u_{N,M}^c \left( \hat{t}_{N_k,0:N_k}^{(k),\alpha} \right)$ , can be easily calculated through Formulas (8.3a) or (8.3b), a difficulty arises in accurately computing the corresponding corrected state values at the SGG points,  $s_{N_k}^c = s_{0:N_k}^{c,k} := s^{c,k} \left( \hat{t}_{N_k,0:N_k}^{(k),\alpha} \right) \forall k \in \mathfrak{R}_3$ , where  $s^{c,k}$  is the corrected state function on  $\Gamma_k \forall k \in \mathfrak{R}_3$ . In particular, attempting to calculate the interpolated, predicted state values at the SGG points,  $s_k^p = s_{0:N_k}^{p,k} := I_N s^p \left( \hat{t}_{N_k,0:N_k}^{(k),\alpha} \right) \forall k \in \mathfrak{R}_3$ , through Eq. (8.2a) to recover the necessary values of  $\psi$  at the SGG points would drive the iterative method employed to solve the nonlinear system (8.4) to generate a sequence of spurious approximations to the state values at the equispaced nodes,  $s_{1:N-1}$ , using crude input data induced by poor approximations to the state derivative values at the SGG points,  $\psi_{0:N_k}^G := \psi \left( \hat{t}_{N_k,0:N_k}^{(k),\alpha} \right) \forall k \in \mathfrak{R}_3$ , which are inherited from the noisy data  $\bar{s}_N^p$ . A viable alternative to overcome this problem is to resample the collocation points set and carry out the collocation of Eq. (3.5) at the SGG points  $\hat{t}_{N_k,0:N_k}^{(k),\alpha} \forall k \in \mathfrak{R}_3$  in lieu of the equispaced nodes  $x_{N,1:N-1}$  to obtain the following nonlinear systems of equations:

$$s_{N_k}^c = \bar{s} \mathbf{I}_{N_k+1} + \mathcal{I}_{\Omega_{\hat{t}_{N_k,0:N_k}^{(k),\alpha}}}^{(t)} \psi, \quad \forall k \in \mathfrak{R}. \quad (8.5)$$

To put it another way, the initial “prediction” phase of our proposed method predicts the optimal state- and control-values through collocation of Problem  $\mathcal{IP}$  in the Fourier physical space at the set of mesh points  $\mathbb{S}_N$ . The next “correction” phase refines the predicted values of the solutions through three steps: (i)  $\tilde{\xi}_{1:2}$  of the predicted controller are estimated and  $\tilde{u}_{N,M}$  is reconstructed from the FPS data using Algorithm A.2, (ii)  $\tilde{u}_{N,M}$  is corrected through Formula (8.3a) or (8.3b) to obtain the corrected optimal control  $u_{N,M}^c$ , and (iii) the predicted optimal state values  $s_N^p$  at the equispaced nodes are corrected through collocation of Eq. (3.5) at the SGG points to obtain the corrected optimal state values  $s_{N_k}^c$ . The profile of the corrected optimal state variable  $s^{c,k}$  on  $\Omega_T$  can be generated via a piecewise combination of the SG interpolants defined by Eqs. (7.4), (7.5), and (7.7). We denote the corrected optimal objective function value associated with  $s^{c,k}$  and  $u_{N,M}^c$  by  $J_{N_k}^c$ .

**Remark 8.1.** We prefer to solve the nonlinear system (8.5) using MATLAB fsolve solver carried out using the efficient Trust-Region-Dogleg Algorithm, which is specially designed to solve nonlinear equations. To initiate the iterative

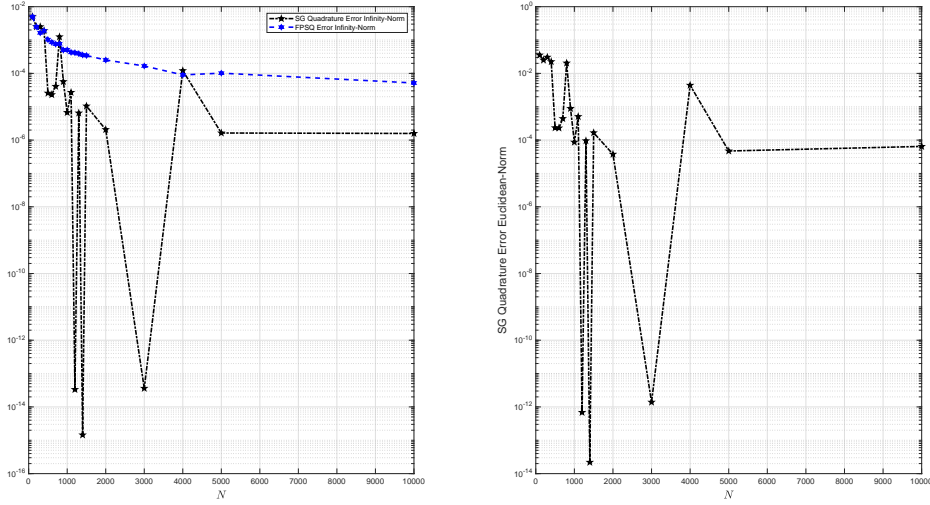


Figure 17: The figure shows the error infinity- and -Euclidean norms of the 2-point SG quadrature with  $\alpha = -0.1$  in log-lin scale of the reconstructed square wave function  $\check{f}_{6,N,400}$  when successively integrated over the intervals  $\Omega_{x_{N,0};x_{N-1}}$ , for several increasing values of  $N$ . The left plot also shows the corresponding FPSQ error infinity-norms using FPSI matrices of size  $N$ .

method, we can evaluate  $s_k^p$  through Eq. (8.2a) and use it as an initial guess for the corrected state vector together with  $\mathbf{u}_{N_k}^c$  to set up the initial guesses for  $\psi_{0:N_k}^G \forall k \in \mathfrak{R}$ . Therefore, as the Trust-Region-Dogleg Algorithm progresses through iterations, both approximations to the state and its derivative get improved and ultimately the sequence of solution approximations converge rapidly to  $s_{N_k}^c$ .

## 9. Simulation Results

This section shows the approximate optimal solutions and objective function values obtained through the proposed method using the parameters values  $s_{\text{in}} = 3$ ,  $\bar{s} = 2.9$ ,  $u_{\text{min}} = 0$ ,  $u_{\text{max}} = 2$ ,  $\mu_{\text{max}} = 1$ , and  $k_s = 2.5$ . The numerical experiments were carried out using MATLAB R2022a software installed on a personal laptop equipped with a 2.9 GHz AMD Ryzen 7 4800H CPU and 16 GB memory running on a 64-bit Windows 11 operating system. The constrained optimization problem (8.1) was solved using MATLAB fmincon solver with the interior-point algorithm. The fmincon solver was carried out using the stopping criteria TolFun = TolX = 1E-14 and the initial guesses  $s(t) = \bar{s}$  and  $u(t) = \bar{u} = 58/63 \approx 0.92063492063492063 \forall t \in \Omega_T$ , which can be calculated through Eq. (3.4). The nonlinear system (8.5) was solved using MATLAB fsolve solver carried out using the Trust-Region-Dogleg Algorithm with the stopping criteria StepTolerance = TolFun = 1E-15.

Figure 18 shows the approximate optimal solutions plots obtained at various stages on  $\Omega_{10}$  for the parameter values  $N = 100$ ,  $M = 100$ ,  $N_{1:3} = [16]_3$ , and  $\alpha = -0.1$ . Both fmincon and fsolve solvers were terminated successfully in 63- and 3-iterations, respectively. The corresponding median of the measured wall-clock time for running the FG-PC method was about 1.19 s. Notice here how the noisy data obtained in the prediction phase due to Gibbs effect has been successfully smoothed out in the correction phase. Notice also the distinctive feature in the profile of the corrected optimal state variable arising in the formation of an interior layer followed by a boundary layer at which a steep fall in the substrate concentration was noted near the end of the time period. In particular,  $s^{c,k}$  exhibits two thin transition layers where it varies rapidly, but varies regularly and slowly in the remaining part of the domain. The corresponding corrected optimal controller is a bang-bang controller that contains only two switches with the second switch being in close proximity to  $t = T$ . Figure 19 shows the plots of both  $J_N^p$  and  $J_N^c$  for increasing  $N$ -values, where  $J_N^c$  converges to 2.407 rounded to three decimal digits. The approximate time switches values  $\check{\xi}_i, i = 1, 2$  obtained by the current method were about 5.39 and 9.95 s, respectively. Figure 20 shows further the plots of the corrected optimal performance index value  $J_N^c$  against the cycling time  $T$ , for  $T = 0 : 40$ ,  $N = 100$ ,  $M = 1000$ ,  $N_{1:3} = [20]_3$ , and  $\alpha = 1/2$ , in which we observe the monotonic decline of the  $J_N^c$ -curve as the cycling time  $T$  increases before it nearly flattens as  $T$  grows large.

Table 4: Observed absolute errors in the definite integrals of functions  $f_6, \dots, f_{12}$  when they are approximated by FPSQs using the reconstructed  $\check{f}_{6,N,M}, \dots, \check{f}_{12,N,M}$  obtained by Algorithm A.2 with  $M = 100$  and  $M = 400$ . All approximations are rounded to 5 significant digits.

	$N$	$\ I_{x_N} f_6 - I_{x_N} \check{f}_{6,N,M}\ _\infty$	$\ I_{x_N} f_7 - I_{x_N} \check{f}_{7,N,M}\ _\infty$	$\ I_{x_N} f_8 - I_{x_N} \check{f}_{8,N,M}\ _\infty$	$\ I_{x_N} f_9 - I_{x_N} \check{f}_{9,N,M}\ _\infty$	$\ I_{x_N} f_{10} - I_{x_N} \check{f}_{10,N,M}\ _\infty$	$\ I_{x_N} f_{11} - I_{x_N} \check{f}_{11,N,M}\ _\infty$	$\ I_{x_N} f_{12} - I_{x_N} \check{f}_{12,N,M}\ _\infty$
$M = 100$	100	7.7031E-03	2.8499E-03	6.4450E-03	1.6746E-02	3.9564E-03	3.2151E-02	1.5815E-02
	200	3.0731E-03	5.6578E-03	4.1025E-02	2.4944E-02	1.0960E-02	2.6135E-02	2.2157E-02
	300	1.6667E-03	5.0021E-03	1.9992E-02	1.8794E-02	7.1784E-03	2.5017E-02	2.1124E-02
	400	1.2896E-03	7.4427E-03	2.0185E-02	3.6597E-02	4.2957E-03	4.7179E-02	2.2133E-02
	500	1.0332E-03	4.3404E-03	1.8230E-02	2.4678E-02	6.3296E-03	3.2689E-02	2.8087E-02
	600	8.9546E-04	5.8339E-03	2.3331E-02	2.8593E-02	5.2307E-03	3.7298E-02	2.4069E-02
	700	6.8502E-04	4.6952E-03	1.8076E-02	2.3719E-02	5.6152E-03	3.8174E-02	2.3842E-02
	800	5.9732E-04	5.0583E-03	2.3303E-02	2.5245E-02	5.1227E-03	3.5575E-02	2.4860E-02
	900	5.5556E-04	4.9998E-03	2.0001E-02	2.3055E-02	5.9836E-03	3.8001E-02	2.7461E-02
	1000	3.1066E-04	5.5535E-03	2.0603E-02	2.8201E-02	6.4653E-03	3.8083E-02	2.5833E-02
	1100	4.5455E-04	4.6968E-03	1.9224E-02	2.4954E-02	5.2746E-03	3.9082E-02	2.0363E-02
	1200	4.1667E-04	5.4165E-03	2.1667E-02	2.6671E-02	5.4272E-03	3.9515E-02	2.1901E-02
	1300	3.6638E-04	4.8359E-03	1.8955E-02	2.4179E-02	5.5601E-03	3.9710E-02	2.2902E-02
	1400	2.6414E-04	5.0957E-03	2.1246E-02	2.6127E-02	5.6021E-03	3.9737E-02	2.4127E-02
	1500	3.1292E-04	5.0001E-03	2.0000E-02	2.4036E-02	5.1751E-03	4.0622E-02	2.5140E-02
2000	2.7553E-04	5.0712E-03	2.0691E-02	2.5050E-02	5.5265E-03	4.1313E-02	2.5945E-02	
3000	1.5649E-04	5.1667E-03	2.0667E-02	2.5569E-02	5.3667E-03	3.7809E-02	2.5086E-02	
4000	9.0703E-05	5.1131E-03	2.0131E-02	2.4526E-02	5.6293E-03	4.0266E-02	2.4683E-02	
5000	9.3887E-05	5.0319E-03	2.0229E-02	2.5145E-02	5.4800E-03	3.8022E-02	2.4418E-02	
10000	7.5134E-05	5.0287E-03	2.0062E-02	2.4810E-02	5.6274E-03	3.8548E-02	2.3900E-02	
$M = 400$	100	4.9996E-03	2.8670E-03	6.3275E-03	1.8210E-02	3.9583E-03	3.2113E-02	1.4180E-02
	200	2.5001E-03	8.3199E-04	5.7223E-03	5.4374E-03	3.2109E-03	3.3962E-02	1.4262E-02
	300	1.6449E-03	1.6646E-03	6.6748E-03	2.1666E-03	5.1743E-04	3.0778E-02	5.2880E-03
	400	1.8965E-03	7.1559E-04	1.6532E-03	3.7499E-03	5.8589E-04	2.8770E-03	4.6719E-03
	500	1.0256E-03	3.3118E-04	2.2930E-03	4.6999E-03	1.3704E-03	2.0028E-02	8.2111E-03
	600	8.5638E-04	8.3282E-04	3.3354E-03	4.0511E-03	1.3538E-03	2.9835E-02	6.7314E-03
	700	7.5520E-04	1.8381E-03	6.6682E-03	2.3560E-03	5.0315E-04	2.3221E-02	4.8724E-03
	800	7.7339E-04	1.4188E-03	1.0400E-02	4.4291E-03	1.5498E-03	2.1083E-02	7.3088E-03
	900	5.0073E-04	1.6669E-03	6.6658E-03	8.3327E-04	7.6506E-04	1.6931E-02	2.7026E-03
	1000	5.0672E-04	1.2866E-03	4.6635E-03	1.5994E-03	9.7877E-04	1.9428E-02	5.1536E-03
	1100	4.2765E-04	1.0556E-03	4.6855E-03	2.2419E-03	1.1314E-03	1.8328E-02	2.7325E-03
	1200	4.1667E-04	1.2501E-03	4.9995E-03	1.9188E-03	4.7075E-04	1.1344E-02	4.6587E-03
	1300	3.9110E-04	9.8973E-04	3.6005E-03	1.0884E-03	6.6346E-04	1.2153E-02	2.4482E-03
	1400	3.5714E-04	1.5477E-03	6.5332E-03	5.3092E-04	8.8572E-04	2.0928E-02	4.6611E-03
	1500	3.4382E-04	1.0001E-03	3.9997E-03	5.5662E-04	9.9820E-04	1.8945E-02	2.5315E-03
2000	2.5207E-04	1.0838E-03	4.5694E-03	3.0036E-04	6.4333E-04	1.3095E-02	3.7522E-03	
3000	1.6667E-04	1.1667E-03	4.6666E-03	6.7591E-04	4.9595E-04	1.4990E-02	3.2590E-03	
4000	8.9983E-05	1.3978E-03	5.1346E-03	7.0223E-04	6.5124E-04	1.2374E-02	3.0360E-03	
5000	1.0163E-04	1.2332E-03	5.0293E-03	1.1999E-04	7.3058E-04	1.1753E-02	3.9238E-03	
10000	5.1581E-05	1.2287E-03	4.8663E-03	2.5096E-04	8.2991E-04	1.2116E-02	3.6048E-03	

## 10. Conclusion and Further Remarks

It is demonstrated via numerical simulations that the performance of the chemostat can be upgraded with minimal costs in terms of the time-averaged substrate concentration by adopting the optimal control strategy obtained through the proposed FG-PC method. The numerical simulations manifest also the decay of  $J_N^c$  with a slower rate as  $T$  increases before it converges asymptotically to a certain limit for a large cyclic time  $T$ ; therefore, the performance of the chemical reactor can be increased significantly as  $T$  increases up to a certain  $T$ -limit. Part of the success of the FG-PC method is due to the accurate and efficient construction of the newly developed FPSI matrices in reduced form through Algorithm A.1, which can quickly generate the needed FPS data in the prediction phase. Another indispensable feature of the proposed method lies in its ability to determine sufficiently close estimates to the jump discontinuities of the bang-bang controller and reconstructing an accurate control model through the novel Algorithm A.2. The derived barycentric SG quadratures proved to be highly accurate and feasible in the correction phase of the FG-PC method and the numerical simulations demonstrate their excellent capacity together with the Trust-Region-Dogleg Algorithm in computing the necessary definite integrals of the reconstructed state derivative discontinuous function from the FPS data. The current paper asserts that the optimal substrate concentration corresponding to the optimal dilution rate of the experimental data exhibits two thin transition layers— one interior layer and one boundary layer near the end of the time period— where it varies rapidly, but varies regularly and slowly in the remaining part of the domain. The current paper asserts also that the associated optimal periodic control has exactly two switching times and the optimal controller should be defined by Formula (8.3b) such that the optimal dilution rate should remain zero for about half the time period until the occurrence of the first switching time. Assuming that the time period is measured in hours (h), this policy of the FG-PC method recommends that the chemostat should initially pass through a starvation phase in which no nutrient flow to the chemostat culture is allowed for about 5.39 h. Since  $\mu_{\max} > \bar{u}$ , the utilization of substrate exceeds the initial supply of substrate in the absence of washout<sup>6</sup>, causing the micro-organisms population to monotonically increase at a rapid pace, while the substrate concentration is consumed until it nearly runs

<sup>6</sup>The washout term means the mass flow rate of cells that leave with the outgoing stream.

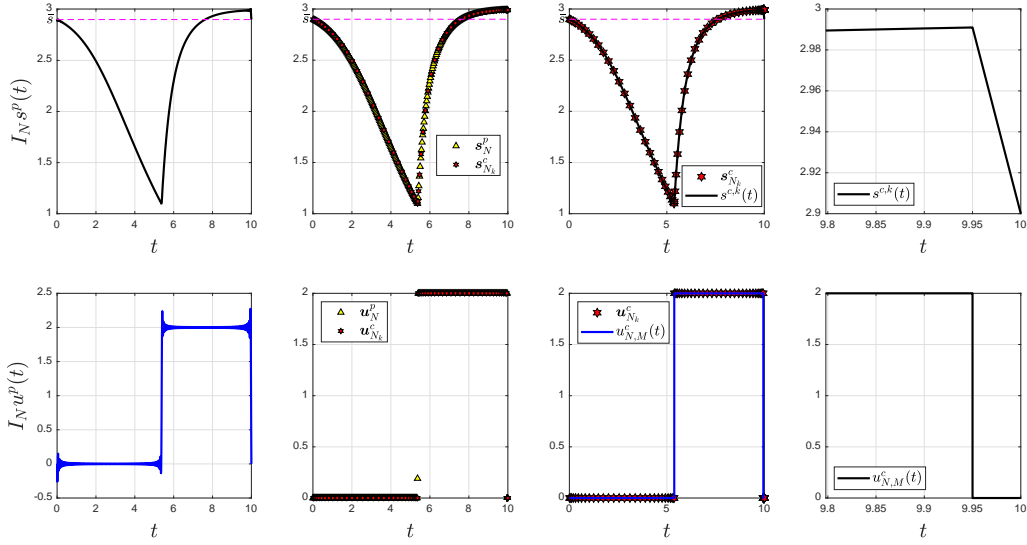


Figure 18: The approximate solutions obtained by the FG-PC method using the parameter values  $N = 100$ ,  $M = 100$ ,  $N_{1:3} = [16]_3$ , and  $\alpha = -0.1$ . The first column shows the plots of the predicted optimal state- and control-variables on  $\Omega_{10}$  using  $M + 1$  equispaced points from 0 to 10 connected by line segments. The second column shows the predicted state- and control-variables at the equispaced collocation points set  $\mathbb{S}_N$  together with their corresponding corrected values at the SGG points sets  $\mathbb{G}_{N_{1:3}}^{(\alpha)}$ . Column 3 shows the corrected data at the collection of SGG points sets  $\mathbb{G}_{N_{1:3}}^{(\alpha)}$  and the estimated discontinuity points  $\tilde{\xi}_i$ ,  $i = 1, 2$  sorted in ascending order in addition to the interpolated, corrected optimal state- and control-variables,  $s^{c,k}$  and  $u_{N,M}^c$ , respectively. Column 4 shows a zoom in of the corrected optimal state- and control-variables near  $t = T$ . The level of the substrate concentration  $\bar{s}$  is shown in horizontal dashed line.

out by the end of the same period. The current optimal control policy shows later that the dilution rate should shift abruptly into  $2 \text{ h}^{-1}$  and remain constant at this level for about 4.56 h; the supply of substrate added with the inflowing fresh medium during this phase exceeds the demand of substrate in the presence of increasing washout rate, causing the substrate concentration to increase rapidly, while the microbes can no longer reproduce fast enough to maintain a population as they are continuously being washed out of the vessel until their population reaches nearly an extinction level at the end of this period. For the next 3 minutes, the optimal dilution rate shifts back to zero and the media feed stops. During this last phase, the substrate concentration is initially at its peak while the number of cells is at its minimum, so the substrate depletion is substantial, lowering the concentration of the limiting substrate rapidly while the cells' population grows swiftly until they both return to their initial states by the end of the time period. Although this optimal control policy can overall maximize the chemostat performance, caution must be exercised when applying this strategy, since any slight changes in the process path may risk severe process instabilities. For example, a shift to slightly higher dilution rate in the second phase may lead to a complete washout of the cells. Perhaps another important result from a numerical viewpoint that could be added to the above list is the fact that the numerical results derived in [15] were obtained using a local optimization solver with random initial guesses, while the current FG-PC method employs automatically-calculated and sufficiently close initial guesses at the outset of the correction phase, which adds more support and credibility to the new study results presented in the paper.

## 11. Future Work

One potential direction is to investigate the possibility of adding the time period  $T$  as another optimization variable and then probe how that would affect the proposed algorithm.

## Competing Interests

The author declares there is no conflict of interests.

## Availability of Supporting Data

The author declares that the data supporting the findings of this study are available within the article.



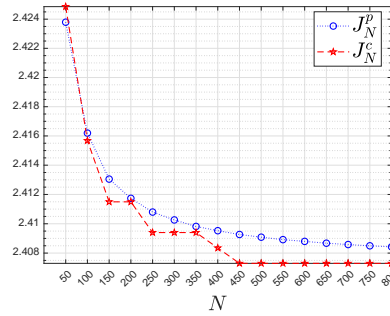


Figure 19: Plots of  $J_N^p$  and  $J_N^c$  against  $N = 50 : 50 : 800$  using the FG-PC method with  $M = 1000$ ,  $N_{1:3} = [30]_3$ , and  $\alpha = 1/2$ .

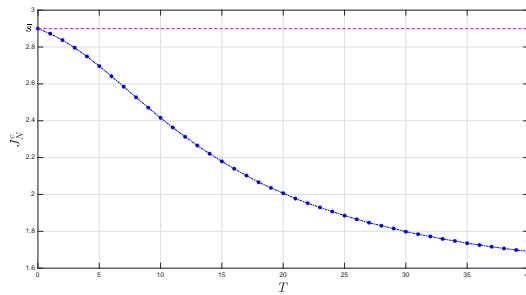


Figure 20: Plots of the corrected optimal performance index  $J_N^c$  against the cycling time  $T$ , for  $T = 0 : 40$ ,  $N = 100$ ,  $M = 1000$ ,  $N_{1:3} = [20]_3$ , and  $\alpha = 1/2$ .

### Ethical Approval and Consent to Participate

Not Applicable.

### Human and Animal Ethics

Not Applicable.

### Consent for Publication

Not Applicable.

### Funding

The author received no financial support for the research, authorship, and/or publication of this article.

### Authors' Contributions

The author confirms sole responsibility for the following: study conception and design, data collection, analysis and interpretation of results, and manuscript preparation.

### Acknowledgments

Not applicable.

---

**Algorithm A.1** Faster, More Accurate, and More Economic Construction of  $\Theta$ 


---

**Input:** A positive real number  $T$ ; a column vector  $\mathbf{x}$  of even  $N$ -equally-spaced points.

**Output:** The elements  $\theta_{l,j}$ ,  $1 \leq l, j \leq N$ , of  $\Theta$ .

```

Set  $N_x \leftarrow N$ ;  $N-1 \leftarrow N_{-1}$ ;  $N+2 \leftarrow N_{+2}$ ;  $N+3 \leftarrow N_{+3}$ ;  $N/2 \leftarrow N_{\div 2}$ ;            $\triangleright N_x$  is the number of elements of  $\mathbf{x}$ .
 $\mathbf{O}_N \leftarrow \mathbf{O}$ ;  $2\pi/T \leftarrow c_1$ ;                                            $\triangleright \mathbf{O}_N$  is the zeros matrix of size  $N$ .
 $[-N_{\div 2} : N_{\div 2} - 1]_{\neq 0} \leftarrow \mathbf{K}$ ;  $i/c_1 \leftarrow c_2$ ;                        $\triangleright$  The notation  $[\cdot]_{\neq 0}$  means excluding 0.
 $\exp((c_1 i \mathbf{K}) \otimes \mathbf{x}) \leftarrow \mathbf{A}$ ;  $1 - \mathbf{A}_{2:N,:} \leftarrow \mathbf{B}$ ;                    $\triangleright \mathbf{Z}_{n,:}$  is a row vector whose elements form the  $n$ th row of a matrix  $\mathbf{Z}$ .
for  $l = 2 : N$  do
  Set  $l-1 \leftarrow L_{-1}$ ;  $1 : \lfloor (l+3)/2 \rfloor \leftarrow \mathbf{C}$ ;  $2 : \lfloor (N_{+3} - l)/2 \rfloor \leftarrow \mathbf{D}$ ;            $\triangleright \lfloor \cdot \rfloor$  is the floor function.
  for  $j = \mathbf{C}$  do
     $\sum [\mathbf{B}_{L_{-1},:} \otimes (\mathbf{K} \circ \mathbf{A}_{j,:})] \leftarrow \theta_{l,j}$ ;                                $\triangleright \sum$  is the sum of array elements.
  end for
  Set  $\theta_{l,C} \leftarrow \theta_{l,l+1-C}$ ;
  if  $l \leq N_{-1}$  then
    for  $j = \mathbf{D}$  do
       $L_{-1} + j \leftarrow k$ ;  $\sum [\mathbf{B}_{L_{-1},:} \otimes (\mathbf{K} \circ \mathbf{A}_{k,:})] \leftarrow \theta_{l,k}$ ;
    end for
     $\theta_{l,L_{-1}+D} \leftarrow \theta_{l,N_{+2}-D}$ ;
  end if
   $x_l + \text{Re}(c_2 \theta_{l,:}) \leftarrow \theta_{l,:}$ ;                                            $\triangleright \text{Re}$  is the real part of a complex number.
end for
 $\Theta/N \leftarrow \Theta$ ;

```

---

## A. Computational Algorithms

### References

- [1] N. Ziv, N. J. Brandt, D. Gresham, The use of chemostats in microbial systems biology, *JoVE (Journal of Visualized Experiments)* (2013) e50168.
- [2] R. M. Maier, I. L. Pepper, Chapter 3 - bacterial growth, in: I. L. Pepper, C. P. Gerba, T. J. Gentry (Eds.), *Environmental Microbiology* (Third Edition), Academic Press, San Diego, third edition edition, 2015, pp. 37–56.
- [3] X. Xu, Y. Qiu, X. Chen, H. Zhang, Z. Liang, B. Tian, Bifurcation analysis of a food chain chemostat model with Michaelis-Menten functional response and double delays, *AIMS Mathematics* 7 (2022) 12154–12176.
- [4] A. Eliasson, C. Christensson, C. F. Wahlbom, B. Hahn-Hägerdal, Anaerobic xylose fermentation by recombinant *Saccharomyces cerevisiae* carrying XYL1, XYL2, and XKS1 in mineral medium chemostat cultures, *Applied and environmental microbiology* 66 (2000) 3381–3386.
- [5] P. Gray, S. Bhuwapathanapun, Production of the macrolide antibiotic tylosin in batch and chemostat cultures, *Biotechnology and Bioengineering* 22 (1980) 1785–1804.
- [6] M. Raatz, S. Schaelicke, M. Sieber, A. Wacker, U. Gaedke, One man’s trash is another man’s treasure—the effect of bacteria on phytoplankton–zooplankton interactions in chemostat systems, *Limnology and Oceanography: Methods* 16 (2018) 629–639.
- [7] J. Douglas, D. Rippin, Unsteady state process operation, *Chemical Engineering Science* 21 (1966) 305–315.
- [8] G. Butler, S.-B. Hsu, P. Waltman, A mathematical model of the chemostat with periodic washout rate, *SIAM Journal on Applied Mathematics* 45 (1985) 435–449.
- [9] E.-M. Abulesz, G. Lyberatos, Periodic optimization of continuous microbial growth processes, *Biotechnology and bioengineering* 29 (1987) 1059–1065.
- [10] G. P. Kumar, I. S. Sastry, M. Chidambaram, Periodic operation of a bioreactor with input multiplicities, *The Canadian Journal of Chemical Engineering* 71 (1993) 766–770.
- [11] M. Petkovska, D. Nikolić, A. Marković, A. Seidel-Morgenstern, Fast evaluation of periodic operation of a heterogeneous reactor based on nonlinear frequency response analysis, *Chemical engineering science* 65 (2010) 3632–3637.
- [12] G. S. Wolkowicz, X.-Q. Zhao,  $n$ -species competition in a periodic chemostat, *Differential and Integral Equations* 11 (1998) 465–491.
- [13] Q.-L. Peng, H. Freedman, Global attractivity in a periodic chemostat with general uptake functions, *Journal of mathematical analysis and applications* 249 (2000) 300–323.
- [14] L. Wang, D. Jiang, D. O’Regan, The periodic solutions of a stochastic chemostat model with periodic washout rate, *Communications in Nonlinear Science and Numerical Simulation* 37 (2016) 1–13.
- [15] T. Bayen, A. Rapaport, F.-Z. Tani, Optimal periodic control of the chemostat with Contois growth function, *IFAC-PapersOnLine* 51 (2018) 730–734.
- [16] T. Bayen, A. Rapaport, F. Z. Tani, Improvement of performances of the chemostat used for continuous biological water treatment with periodic controls, *Automatica* 121 (2020) 109199.
- [17] J. Bailey, Periodic operation of chemical reactors: A review, *Chemical Engineering Communications* 1 (1974) 111–124.
- [18] A. Renken, Unsteady-state operation of continuous reactors, *International Chemical Engineering* 24 (1984) 202–213.
- [19] T. Caraballo, X. Han, P. E. Kloeden, A. Rapaport, Dynamics of nonautonomous chemostat models, in: *Continuous and Distributed Systems II*, Springer, 2015, pp. 103–120.
- [20] N. Cogan, Optimal control methods for controlling bacterial populations with persister dynamics, in: *AIP Conference Proceedings*, volume 1738, AIP Publishing LLC, p. 320004.
- [21] D. Contois, Kinetics of bacterial growth: Relationship between population density and specific growth rate of continuous cultures, *Microbiology* 21 (1959) 40–50.
- [22] R. T. Alqahtani, M. I. Nelson, A. L. Worthy, Analysis of a chemostat model with variable yield coefficient: Contois kinetics, *ANZIAM Journal* 53 (2011) C155–C171.
- [23] A. Moser, *Bioprocess technology: Kinetics and reactors*, Springer Science & Business Media, 2012.
- [24] K. T. Elgindy, H. M. Refat, A direct integral pseudospectral method for solving a class of infinite-horizon optimal control problems using Gegenbauer polynomials and certain parametric maps, 2022. Manuscript submitted for publication.
- [25] K. T. Elgindy, H. M. Refat, High-order Gegenbauer integral spectral element method integrated with an adaptive Chebyshev optimization strategy for solving linear singularly perturbed differential equations, *Journal of Computational and Applied Mathematics* 372 (2020) 112722.

---

**Algorithm A.2** Reconstruction of the Approximate Discontinuous Function  $\check{f}_{N,M}$  from the FPS Data
 

---

**Input:** Numbers  $T \in \mathbb{R}^+$ ,  $M \in \mathbb{Z}^+$ ; equally-spaced column vector  $\mathbf{y}_M^+$ ; Fourier interpolant values column vector  $\mathbf{Inf} = I_N f(\mathbf{y}_M^+)$ ; user-defined tolerances  $\tilde{\epsilon}, \epsilon$ .

**Output:** The approximate discontinuous function  $\check{f}$ .

```

1: Set  $\emptyset \leftarrow \Xi$ ;  $M^- \leftarrow M - 1$ ;  $\emptyset \leftarrow \Lambda$ ;  $\emptyset \leftarrow \rho_1$ ;  $\mathbf{0} \leftarrow [\rho_2; \rho_3]$ ; ▷  $\emptyset$  denotes the empty vector.
2:  $\text{indmin } \mathbf{Inf} \leftarrow v_1$ ;  $\text{indmax } \mathbf{Inf} \leftarrow v_2$ ;
3: Calculate  $I_N^{\text{min}} f$  and  $I_N^{\text{max}} f$  using the CPSLSM; ▷ See Section 6.1.
4:  $\frac{1}{2} (I_N^{\text{max}} f + I_N^{\text{min}} f) \leftarrow \mu$ ;  $|\mathbf{Inf} - \mu \mathbf{I}_{M+1}| \leftarrow d_1$ ;  $\min d_1 \leftarrow d_2$ ;  $\epsilon = \tilde{\epsilon} (I_N^{\text{max}} f - I_N^{\text{min}} f)$ ;
5: if  $d_2 \leq \epsilon$  then
6:    $\text{ind}(d_1 \leq \epsilon) \leftarrow \Lambda$ ;  $\rho_2 = (\Lambda == M^-)$ ;  $\Lambda(\rho_2) = M$ ;  $\mathbf{y}_{M,\Lambda} \leftarrow \Xi$ ;  $\rho_1 = \Lambda$ ;
7: end if
8: if  $|\Lambda| < 2$  then ▷  $|\Lambda|$  is the length of  $\Lambda$ .
9:   Calculate  $I_N^{\text{aux}} f(\mathbf{y}_M^+)$  using Eq. (6.1);
10:  Find  $J_{1,2} : I_N^{\text{aux}} f(\mathbf{y}_{M,J_1}) - I_N^{\text{aux}} f(\mathbf{y}_{M,J_1+1}) \neq 0$ ,  $l = 1, 2$ ;
11:  if  $J_2 = M^-$  and  $\text{any}(\rho_2) = 0$  then ▷  $\text{any}(\mathbf{A})$  returns 1 if any of the elements of  $\mathbf{A}$  is a nonzero number, and returns 0 otherwise.
12:     $\Xi = [\Xi, T]$ ;  $\rho_3 = 1$ ;
13:  end if
14:  if  $|\Xi| < 2$  then
15:    if  $\rho_1 = \emptyset$  and  $\rho_3 = 0$  then
16:       $\frac{1}{2} (\mathbf{y}_{M,J_{1,2}} + \mathbf{y}_{M,J_{1,2}+1}) \leftarrow \Xi$ ;
17:    else
18:      for  $l = 1 : 2$  do
19:        if  $\mathbf{y}_{M,J_l} - \Xi > \epsilon$  or  $\Xi - \mathbf{y}_{M,J_l+1} > \epsilon$  then
20:           $\text{sort}([\Xi; \frac{1}{2} (\mathbf{y}_{M,J_l} + \mathbf{y}_{M,J_l+1})]) \leftarrow \Xi$ ; ▷  $\text{sort}(\mathbf{A})$  sorts the elements of  $\mathbf{A}$  in ascending order.
21:        end if
22:      end for
23:    end if
24:  end if
25: end if
26:  $\text{ind}(\mathbf{Inf} > \mu) \leftarrow \bar{J}_1$ ;  $\text{ind}(\mathbf{Inf} < \mu) \leftarrow \bar{J}_2$ ;
27:  $\text{median}(\mathbf{Inf}_{\bar{J}_1}) \leftarrow \check{f}^{\text{max}}$ ;  $\text{median}(\mathbf{Inf}_{\bar{J}_2}) \leftarrow \check{f}^{\text{min}}$ ; ▷ median gives the median value of an array.
28: if  $\mathbf{Inf}_0 > \mu$  then
29:    $\begin{cases} \check{f}^{\text{max}}, & 0 \leq t < \Xi_1 \vee \Xi_2 \leq t \leq T, \\ \check{f}^{\text{min}}, & \Xi_1 \leq t < \Xi_2 \end{cases} \leftarrow \check{f}$ ;
30: else
31:    $\begin{cases} \check{f}^{\text{min}}, & 0 \leq t < \Xi_1 \vee \Xi_2 \leq t \leq T, \\ \check{f}^{\text{max}}, & \Xi_1 \leq t < \Xi_2 \end{cases} \leftarrow \check{f}$ ;
32: end if

```

---

- [26] S. A. Dahy, K. T. Elgindy, High-order numerical solution of viscous Burgers' equation using an extended Cole–Hopf barycentric Gegenbauer integral pseudospectral method, *International Journal of Computer Mathematics* (2021) 1–19.
- [27] K. T. Elgindy, High-order adaptive Gegenbauer integral spectral element method for solving non-linear optimal control problems, *Optimization* 66 (2017) 811–836.
- [28] K. T. Elgindy, A high-order embedded domain method combining a Predictor–Corrector–Fourier–Continuation–Gram method with an integral Fourier pseudospectral collocation method for solving linear partial differential equations in complex domains, *Journal of Computational and Applied Mathematics* 361 (2019) 372–395.
- [29] K. T. Elgindy, High-order, stable, and efficient pseudospectral method using barycentric Gegenbauer quadratures, *Applied Numerical Mathematics* 113 (2017) 1–25.
- [30] K. T. Elgindy, B. Karasözen, Distributed optimal control of viscous Burgers' equation via a high-order, linearization, integral, nodal discontinuous Gegenbauer-Galerkin method, *Optimal Control Applications and Methods* 41 (2020) 253–277.
- [31] N. Batir, New inequalities for the Hurwitz zeta function, *Proceedings Mathematical Sciences* 118 (2008) 495–503.
- [32] G. Helmborg, The Gibbs phenomenon for Fourier interpolation, *Journal of Approximation Theory* 78 (1994) 41–63.
- [33] K. T. Elgindy, Optimization via Chebyshev polynomials, *Journal of Applied Mathematics and Computing* 56 (2018) 317–349.
- [34] K. T. Elgindy, High-order numerical solution of second-order one-dimensional hyperbolic telegraph equation using a shifted Gegenbauer pseudospectral method, *Numerical Methods for Partial Differential Equations* 32 (2016) 307–349.
- [35] E. Doha, An accurate solution of parabolic equations by expansion in ultraspherical polynomials, *Computers & Mathematics with Applications* 19 (1990) 75–88.
- [36] K. T. Elgindy, K. A. Smith-Miles, Fast, accurate, and small-scale direct trajectory optimization using a Gegenbauer transcription method, *Journal of Computational and Applied Mathematics* 251 (2013) 93–116.
- [37] K. T. Elgindy, K. A. Smith-Miles, Optimal Gegenbauer quadrature over arbitrary integration nodes, *Journal of Computational and Applied Mathematics* 242 (2013) 82–106.
- [38] K. T. Elgindy, Optimal control of a parabolic distributed parameter system using a fully exponentially convergent barycentric shifted Gegenbauer integral pseudospectral method, *Journal of Industrial & Management Optimization* 14 (2018) 473.
- [39] M. Abramowitz, I. A. Stegun, *Handbook of mathematical functions with formulas, graphs, and mathematical tables*, volume 55, US Government printing office, 1964.
- [40] S. El-Gendi, Chebyshev solution of differential, integral and integro-differential equations, *The Computer Journal* 12 (1969) 282–287.
- [41] K. T. Elgindy, H. M. Refat, High-order shifted Gegenbauer integral pseudo-spectral method for solving differential equations of Lane–Emden type, *Applied Numerical Mathematics* 128 (2018) 98–124.